eman ta zabal zazu

Universidad del País Vasco

Euskal Herriko Unibertsitatea

The Role of the Brain Extracellular Space in Diffusion and Cell Signalling

Doctoral thesis opting to the PhD degree, presented by

Paula Giménez Mínguez

2023

Supervisor:

Dr. Jan Tønnesen

This doctoral thesis has been performed thanks to the usage of a UPV/EHU fellowship for the hiring of predoctoral researchers during 2018-2023.

The experimental work has been financed by the following organizations:

- University of the Basque Country UPV/EHU (GIU21/048)
- Spanish Ministry of Science and Innovation (PID2020-113894RB-I00, PCI2022-135040-2)
- Aligning Science Across Parkinson's (ASAP), ASAP-020505
- Sigma XI grant in aid of research
- National Institute of Health

AGRADECIMIENTOS

Que no hay excusa alguna para no servir a los demás
Siempre sonriente sin dejar a la queja entrar
Que un ángel nos ha enseñado cómo se debe volar
Que si llevas la cruz a cuestas no se tiene por qué notar
Que si esta no es nuestra liga, entonces ¿a qué te quieres aferrar?

Simplemente
Baila y déjate de historias
Aunque no tengas el control
Cualquiera que sea la canción
Déjate llevar en el salón
Déjate hacer, que trace tu camino
Él también quiere bailar contigo

Que si el sufrimiento es por amor
el dolor es diferente
Entrégate hasta el extremo,
empápate de esta fuente.
Inagotable, infinita,
de la que siempre se sacan fuerzas
Es Dios Padre quien te grita
que te acompaña en lo que elijas

Baila – HAKUNA

Si hay alguien a quien tengo que dar gracias en primer lugar, ese eres tú.

Gon, gracias por tu entrega a nuestra familia, por todos los sacrificios que has hecho, por todos los esfuerzos del día a día, por todo tu apoyo para que yo pueda trabajar en lo que me gusta y para que pueda terminar esta tesis doctoral. Perdón por todas las veces que me he llevado el cansancio, la frustración y el desánimo a casa. Gracias por ser luz en mi vida, y afrontar las dificultades que nos vamos encontrando en el camino siempre con alegría, sin queja alguna, con confianza, transformándolas en una aventura más. Gracias por recordarme que no caminamos solos.

"La vocación al matrimonio es una llamada a conducir un barco incierto —pero seguro por la realidad del sacramento— en un mar a veces agitado. Cuántas veces, como los apóstoles, sienten ganas de decir o, mejor dicho, de gritar: «¡Maestro! ¿No te importa que perezcamos?» (Mc 4,38). No olvidemos que a través del sacramento del matrimonio Jesús está presente en esa barca. Él se preocupa por ustedes, permanece con ustedes en todo momento en el vaivén de la barca agitada por el mar."

Carta del Papa Francisco a las familias. Año de la Familia (2021).

A mis padres, cuanto tengo por agradeceros. Sin duda hay tantas cosas por las que daros las gracias. Pero si tengo que elegir una, me quedo con el ejemplo de familia que me habéis regalado. Me habéis

enseñado que la vida da muchas vueltas y puede ir por muchos caminos pero que la familia siempre es lo primero, familia solo hay una y hay que cuidarla. En vosotros he visto una entrega total a vuestra familia, cada uno con un papel, cada uno de una manera, pero siempre remando en la misma dirección y con el mismo compromiso. El valor de la familia y la importancia del matrimonio que he aprendido de vosotros me ha ayudado muchísimo en estos años a saber discernir que es lo que de verdad importa en cada momento. Con el tiempo uno se da cuenta de que no existen los padres perfectos, que son humanos con sus virtudes y defectos y eso es lo más bonito de la familia. Que en ella aprendemos a querer a cada uno en sus virtudes y defectos. Papá, mamá, gracias por todo lo que me habéis enseñado, me llevo una mochila llena de cosas que espero poder inculcar a mis hijos. **A mi hermana**, eres un ejemplo de esfuerzo y superación, de no tirar la toalla cuando todos te dicen que no puedes. Pero sobre todo quiero darte gracias por el cariño con el que me tratas, los detalles que siempre tienes conmigo, recordándome que es muchísimo más importante ser agradable con los demás que ser el mejor en todo.

Y ahora, si la familia es un regalo, menudo regalo tener dos. Gracias **familia Pérez de Villegas Molina.** Llegar a una nueva familia me parece algo tan enriquecedor. De primeras te descuadra, te choca, rompe un poco tu forma de hacer las cosas hasta ahora, pero he aprendido muchísimo de vosotros. Admiro vuestra generosidad, vuestra entrega a las personas que os rodean, siempre con las puertas de casa de par en par dispuestos a acoger a todo el mundo. Gracias por vuestros consejos y vuestra preocupación por nosotros, aunque no siempre hagamos caso, siempre los tenemos en cuenta.

A todos, deciros que si la conciliación familiar es posible es gracias a la familia extensa: abuelos y tíos. Así que sabed que a esta tesis habéis contribuido todos. Llevando a los niños al circo, a patinar, al zoo. Las semanas de vacaciones que os habéis quedado con los nietos para que trabajemos o para que recuperásemos un poco de sueño y salud mental. Siempre dispuestos a echar una mano en lo que haga falta. Una y mil veces gracias.

Now, I would like to thank **Dr. Jan Tønnesen**, my supervisor. Jan, I have to say that I have really enjoyed working with you all these years. A PhD thesis is such a long way and can have long periods of frustrating work. Still you have manged to make this trip enjoyable and peaceful. I have learned a lot with you, and I am really grateful for having you as supervisor. Thank you so much for your patience and your serenity, I have always felt that it was easy to approach you, and ask you anything or give an opinion. But above all, I want to thank you for being so respectful with our personal lives, may be is something that should be given for granted but sadly I think is not that common. Thanks for always being genuinely happy for each of my pregnancies, for encouraging the lab and Achucarro to plan non-work-related activities, for always asking first about the family and the weekend and then about work. Thanks.

Thank you to all my lab colleagues. To the new ones, **Jonny, Dann y Virginia** for the contributions each of you have make to this work. Specially, thank you **Ane** and **Rizky**. It has been many years together already, with many people passing by but always the three of us. It has been great to work with you. Rizky, you are so kind with everyone around, you always have time for others. Always willing to help even when nobody notices it. Also, thank you for all the help with the experiments. Ane, mi compañera de laboratorio, no sabes la paz mental que me has dado todos estos años. Gracias por todos los favores,

por siempre poner facilidades para todo, por ser tan abierta y alegre, por siempre tener algo de lo que charlar. Haces que llegar a la ofi siempre sea agradable. Da gusto trabajar con gente así.

Gracias a los compañeros de ofi que por mucho tiempo han sido para mí mis compañeros de laboratorio. **Eneritz**, amiga, tú has sido LA COMPAÑERA en este camino. Has estado ahí todos los días, en los cafés largos y en los cafés exprés, siempre facilitando a los demás, adaptándote a todo el mundo, ayudando a todo el mundo. Admiro tu entrega en todo, en el trabajo, a los amigos, a la familia. Si alguien te pide ayuda tardas dos minutos en coger una brocha y ponerte a pintar armarios. Es un gusto tenerte como compi de trabajo, pero un regalo tenerte como amiga. Gracias por todos estos años siempre al lado, siempre disponible para charlar y escuchar, animándose a todos los planes, ya sea un cumpleaños un bautizo o una mudanza, que todo te parece fenomenal. Gracias por tu amistad. Gracias a todos los veteranos que ya no estáis. A **Irene**, la alegría en persona, con la que siempre ha sido un gusto compartir alegrías porque te emocionas un montón. Me encanta tu forma de ser, tan sencilla y tan entusiasta. Eres de esas personas que hace que la gente se sienta a gusto a tu alrededor. A **Vir**, por tu forma de escuchar y estar atenta a los demás, de recibir a todo el mundo sin prejuicios. A **Rober**, por todos esos cafés tirados en el suelo. Por ser tan majo, por apuntarte también a cualquier plan. Y a tanta gente más con la que he coincidido en este camino. Habéis hecho que llegar a un sitio nuevo sea fácil y que me lleve tan buenos recuerdos de esos primeros años en Achucarro. A todos los que siguen, y las nuevas incorporaciones que siempre animan y dan vidilla a la oficina.

A todo el personal de Achucarro, que se esfuerza por crear un buen ambiente y por hacer más fácil el trabajo a los demás. Gracias a todos, especialmente a **Alejandro Carretero, y Laura Escobar**. Aunque no he tenido que trabajar codo con codo con vosotros, sois personas que generáis muy buen clima a vuestro alrededor. Siempre con una sonrisa, siempre mostrando interés por los demás, dispuestos a ayudar en lo que haga falta. Gracias por la humanidad que transmitís en el mundo laboral, en el que a veces vamos todos a la carrera solo preocupados por nuestros resultados.

Also, I want to thank **Lauritzen Lab** in Copenhagen for hosting me during my PhD stay. I have learnt a lot from this experience. Specially, I would like to thank Krzysztof and Micael for having the patience of showing me all the work you do and taking the time to teach me all the procedures to do *in-vivo* two-photon imaging. I have learnt a lot from you and I have really enjoyed all the work I did there.

A los muchos amigos que siempre acompañáis con vuestro interés y vuestra oración.

Table of Contents

LIST OF ABREVIATIONS

2D	Two-dimensions
2P-microscopy	Two-photon microscopy
2PSI	Two-photon shadow imaging
3D	Three-dimensions
ACSF	Artificial cerebro-spinal fluid
AF	Alexa Fluor
APD	Avalanche photodiode detector
BBB	Brain-blood-barrier
BGT	Betaine-GABA transporter
BSA	Bovine serum albumin
CA1	First region of the hippocampal circuit
CA3	Region of the hippocampus that receives input from the dentate gyrus
$CaCl_2$	Calcium chloride
Cl^-	Chloride ion
CO_2	Carbon dioxide
Cs	Cesium
CsCl	Cesium chloride
DABCO	Trietilendiamina
Dex-3k	Dextran 3000 molecular weight
Dex-70k	Dextran 70000 molecular weight
DG	Dentate gyrus
ECM	Extracellular matrix
ECS	Extracellular space
EGTA	Egtazic acid

EM	Electron microscopy
FTCS-method	Forward in time central in space finite difference method
GABA	gamma-aminobutyric acid
$GABA_A$-R	$GABA_A$ receptor
GAT	GABA transporter
HBSS	Hank's balanced salt solution
HEPES	2-[4-(2-hydroxyethyl) piperazin-1-yl] ethane sulfonic acid
HS	Horse serum
IOI	Integrative optical imaging
i.p. injection	Intraperitoneal injection
IPSC	Inhibitory post-synaptic current
ISM	Ion selective microelectrode
KCl	Potassium chloride
KY	Kynurenic acid
MEM	Minimum Essential Medium
Mg-ATP	Adenosine tri-phosphate magnesium salt
$MgCl_2$	Magnesium chloride
MRI	Magnetic resonance imaging
MTLE	Mesial temporal lobe epilepsy
n	number of samples in the experiment
Na^+	Sodium ion
Na_2-GTP	Guanosine tri-phosphate di-sodium salt
NaCl	Sodium chloride
NaF	Sodium Fluorescein
NaH_2PO_4	Sodium phosphate
$NaHCO_3$	Sodium bicarbonate
NIP	Nipecotic acid

ns	non-significant
O_2	Oxygen
PBS	Phosphate-buffered saline
Pen-Strep	Penicillin-Streptomycin
PFA	Paraformaldehyde
PMT	Photomultiplier
PSF	Point-spread function
PTX	Picrotoxin
QX-314	Lidocaine N-methyl Bromide
r	Pearson Correlation Coefficient
RTI	Real-time iontophoresis
SD	Standard deviation
SI-units	International system units
SMEI	Severe myoclonic epilepsy of infancy
STED-microscopy	Stimulated emission depletion microscopy
SUSHI	Super-resolution shadow imaging
SWCNT	Single-walled carbon nano-tubes
TBS	Tris-buffered saline
TLE	Temporal lobe epilepsy
TMA^+	Tetramethylammonium
TR-FAIM	Time-resolved fluorescence anisotropy imaging
Trolox	6-hydroxy-2,5,7,8-tetramethylchroman-2-carboxylic acid
UI	User interface
WT	Wild type
α	Volume fraction
λ	Tortuosity
$\boldsymbol{A}$	Unit area

$\boldsymbol{C}$	Concentration
$\boldsymbol{D}$	Diffusion coefficient
$\boldsymbol{D_{av}}$	Average diffusion coefficient
$\boldsymbol{D_{free}}$	Free diffusion coefficient
$\boldsymbol{F}$	Faraday's constant ($F = 96485.33\ C/mol$)
$\boldsymbol{I}$	Iontophoretic current magnitude
$\boldsymbol{J}$	Diffusion flux
$\boldsymbol{M}$	Mass
$\boldsymbol{N_A}$	Avogadro's number ($N_A = 6.022 \cdot 10^{23}$)
$\boldsymbol{S}$	Source magnitude
$\boldsymbol{T}$	Total simulation time
$\boldsymbol{n}$	Number of released particles
$\boldsymbol{n_t}$	Transport number of the iontophoretic electrode
$\boldsymbol{p}$	Diffusion probability
$\boldsymbol{t}$	unit time
$\boldsymbol{z}$	Valency of the ion
$\boldsymbol{\kappa}$	Clearance coefficient
$\boldsymbol{v}$	Velocity field
$\Delta\boldsymbol{t}$	Time step
$\Delta\boldsymbol{x}, \Delta\boldsymbol{y}, \Delta\boldsymbol{z}$	Pixel sizes in the x, y, z dimensions respectively

ABSTRACT

The extracellular space (ECS) is a vast and highly complex space that consists of narrow interconnected channels and reservoirs, and is limited by the resident cells. Even though the ECS is huge in extension, the ECS substructures are usually few nanometers wide and consequently, they are very difficult to visualize. In the last years, researchers have put increasing efforts to investigate the ECS fine geometry and to understand its role in brain functions, such as cellular communication. The brain ECS is a very dynamic structure, that changes at different temporal scales. These structural changes can be physiological, as it has been observed during the sleep-wake cycle, or they can have a pathological cause. In fact, astrocytic swelling at the expense of the ECS volume is one of the hallmarks of epilepsy. Particularly, we are interested in how ECS volume changes affect GABAergic inhibition, the main source of inhibition in the brain and one of the most studied processes in the onset of epileptogenesis.

On the other hand, most intercellular signalling in the brain occurs by diffusion of particles through the ECS channels. Diffusion is the movement of particles from high to low concentration regions. Understanding how diffusion is regulated by the fine geometry of the brain neuropil is becoming the focus of interest for researchers. However, progress in this field is limited by the difficulty to access local ECS diffusion with experimental techniques. As a result, computational modelling has been used over the last years to complement those scientific studies and shed some light in this matter. Recently developed techniques, such as super-resolution shadow imaging (SUSHI), are opening the doors to understand diffusion of molecules through the brain sub-micron ECS structures. In this study, we aim to investigate how the nano-scale ECS geometry of the live brain tissue shapes the diffusion of molecules in the interstitial fluid at different spatio-temporal scales. As well as to understand the impact of ECS local geometry on cellular communication. To attain this goal, we have developed a novel computational model, based on SUSHI images, to study diffusion in the live brain ECS.

GENERAL INTRODUCTION

The extracellular space (ECS) is a vast space of high morphological complexity limited by the cellular membranes. It is composed of narrow interconnected channels and reservoirs containing interstitial fluid and the extracellular matrix (ECM). The ECM is a network of extracellular macromolecules, such as collagen, enzymes and proteoglycans, that provide structural and biochemical support to surrounding cells [1]. The interstitial fluid fills the spaces in the ECS and constitutes an essential microenvironment for the transport of nutrients, neurotransmitters, ions, therapeutic agents, metabolites, etc. Although the overall extent of the ECS is large, millimeter to centimeters, it is very difficult to visualized and study, as the ECS substructures are down to few nanometers wide. As a results, in the past years, researchers have put a lot of effort into investigating the ECS geometry at different scales [2]. Moreover, in the brain, the ECS surrounds billions of neurons and glial cells that are unequally distributed across brain regions. Neurons are highly specialized cells for integration and transmission of signals in networks. They vary enormously in shape and size, depending on their type and physiological state. However, they all present some common structures (Figure 1): I) The soma or cell body that contains the nucleus and major organelles. II) The dendrites that receive incoming synaptic signals. Neurons present an extensively branched dendritic tree, which hosts typically thousands of individual post-synapses. Glutamatergic post-synapses are commonly found on the tip of small protrusions in the dendritic membrane called spines. III) The axon is the output structure of the neuron, and is typically also extensively branched. It harbors typically thousands of presynaptic terminals in bulbous boutons, which each pairs with a post-synapse to form a synapse.

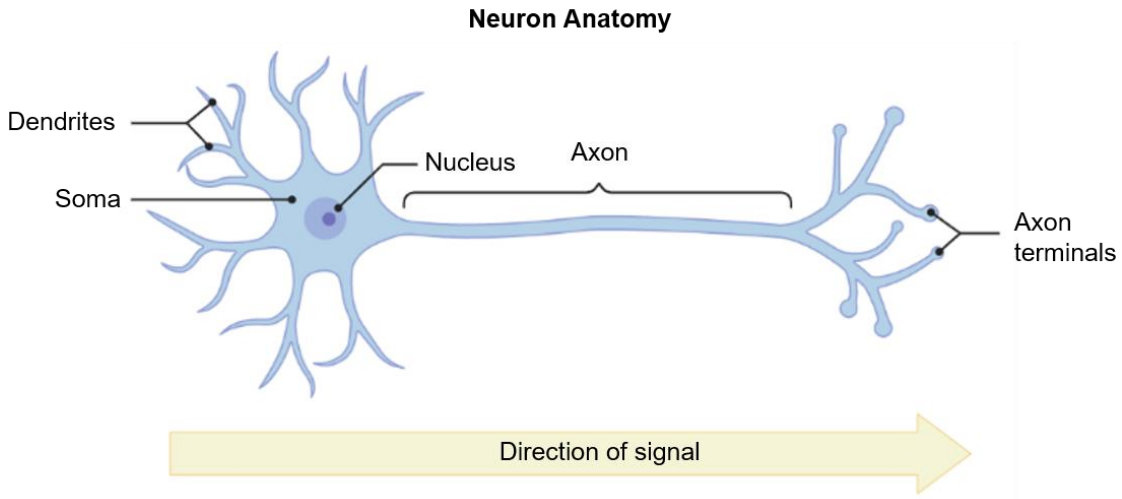

Figure 1 Graphical representation of the general neuron anatomy. Neurons consists of a cell body (soma), where the nucleus is located. They receive input signals from other cells from the dendrites, and the signal is transmitted through a long process (axon). At its end, the axon splits into several branches that end in a protrusion called axon terminals that serve as output for the signal.

Communication between neurons through the release of neurotransmitters at the synapse occurs at the synaptic cleft, where neurotransmitters are released from synaptic buttons (pre-synaptic neuron) and they activate synaptic receptors in a neighboring dendrite (post-synaptic neuron). This type of communication is called *synaptic transmission* [28]. When neurotransmitters escape the synaptic cleft or are released from extra-synaptic sites they diffuse over longer distances and activate neighboring synapses or extra-synaptic receptors. This other form of communication is known as *volume transmission,* [28]. Neuronal processes can extend over long distances (up to 1 m) and are deeply entangled shaping the complex morphology of the brain neuropil. As a result of this intricate mesh, it has been reported that, on average, synapses (pre- and post-synaptic pair) are 0.5 µm away from the closest neighboring synapse [3]. These density and proximity make it likely, if not inevitable, that in some cases neurotransmitters escaping from one synapse will impact the immediate neighbor(s) through extracellular *synaptic crosstalk*, though the functional implications of this remain poorly understood. Thus, the ECS is facilitating all signaling events between cells, spanning distances from of few tens of nanometers across the synaptic cleft, up to conceivably hundreds of microns, as in volume transmission [4].

There are several technical limitations that hinder the study of the brain ECS complexity. Most of the state-of-of-the-art techniques simplify the ECS geometry and describe it merely in terms of volume fraction and tortuosity. The ECS volume fraction (α) is defined as the proportion of brain tissue volume occupied by ECS, while the tortuosity (λ) is the hindrance to diffusing molecules that the tissue imposes in comparison to free diffusion in homogeneous medium. It has been generalized that the brain ECS volume occupies a 20% of the total tissue volume and has an average tortuosity of 1.6 [5], [6]. However, as one can expect, recent publications show that the ECS α drastically varies across brain regions, developmental stages and pathologies [7], [8], as well as the tortuosity [9]–[11].

Currently available techniques to investigate the ECS morphology do not reconcile live-tissue compatibility with submicron imaging resolution. Among the most used methods to address the ECS properties is Real Time Iontophoresis (RTI) together with Integrative Optical Imaging (IOI). RTI measures the diffusion of a tracer (commonly the tetramethylammonium cation – TMA^+) released in the brain ECS iontophoretically by a current pulse, either *in-vivo* or in live slices. Diffusion of the released tracer concentration is measured by an ion-selective microelectrode (ISM) normally located at 100-150 µm from the source point (Figure 2 A). Beforehand, the source-detector microelectrodes are calibrated for a given distance in agar, representing free diffusion. Then, the ECS α and λ values can be extracted by comparing the diffusion curves in brain tissue an in agar (Figure 2 B). Though RTI allows time-lapse measurements in live brain tissue, it does not visualize the ECS geometry and provides very low spatial resolution. The extrapolated ECS properties are averaged over distances of 50-150 µm, determined by the distance between the two-microelectrodes.

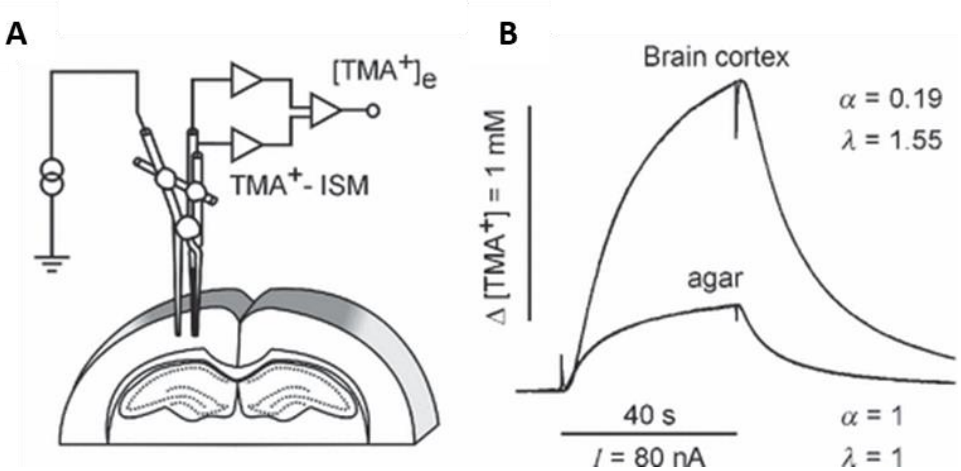

Figure 2 A) Schematic drawing of the microelectrodes' arrangement for *in-vivo* real-time iontophoresis measurement of TMA^+ diffusion in the brain cortex. TMA^+ is released iontophoretically from a micropipette from where it spreads and is measured by an ion-selective microelectrode (ISM) located around 100 microns away. B) TMA^+ diffusion curves over time, measured at the same distance in agar and in the mouse brain. ECS volume fraction (α) and tortuosity (λ) were extracted from the curves. Images taken from *Vorisek and Sykova (2009)*, [12].

Integrative Optical Imaging (IOI) uses epifluorescent microscopy to quantify diffusion of fluorescently-labeled macromolecules over time after pressure ejection in the live brain ECS (Figure 3). While IOI permits very fast time-lapse acquisition *in-vivo* or in slices, it has limited optical resolution spanning over hundreds of microns. Thus, as RTI, it only provides information about volume-averaged properties of the ECS across large volumes. An advantage of IOI over RTI is that we have access to the spatial distribution of the fluorophore in the live tissue and the diffusional properties are extracted from the acquired diffusion pattern. In addition it allows to capture fast dynamics as it presents better temporal resolution [13]. In fact, several studies using IOI have reported heterogenous diffusion patterns across brain regions [14]–[16].

Similar to IOI, there's Intrinsic Optical Signal (IOS) Imaging, a widefield label-free imaging technique which detects changes in the tissue transmission of light. IOS allows almost real-time resolution at a spatial resolution of a few microns and is live tissue compatible. However, it shows low contrast and we cannot distinguish individual neurons.

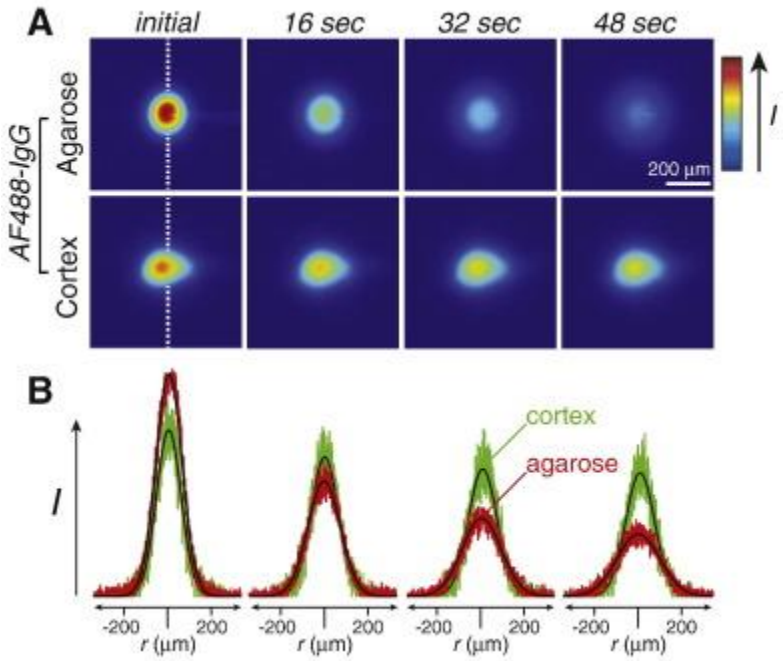

Figure 3 A) Representative IOI images acquired after pressure ejection of AF488-IgG in agarose or cortex. Scalebar 200 µm, color-bar represents fluorescence intensity (B) Fluorescence intensity data extracted along the white dashed line from the IOI images in agar (red) and in the cortex (green). Image borrowed from *Wolak et al. (2015)*, [15].

On the other hand, scanning fluorescence microscopy, such as two-photon (2P) and confocal imaging, allow high resolution imaging of both live and fixed tissue. Even though these techniques have not been commonly used to directly study ECS properties, they have been use together with fluorophore release and spread in the brain ECS to investigate diffusivity of molecules [17]. In 2008, a novel strategy used extracellular administration of fluorophores to produce a negative image of unlabeled neurons using *in-vivo* 2P microscopy [18]. In this work, 2-photon shadow imaging was used to performed targeted patch-clamp electrophysiological recordings of neurons. Recently, 2P shadow imaging has been finally utilize to assess ECS properties in live tissue slices of the mouse retina [7]. As shown in Figure 4 A and C, 2P shadow imaging provides access to the ECS geometry with a lateral (x, y) resolution of around 400 nm and 1 µm axially (z). Even though with this resolution we cannot distinguish structural details in the ECS, Figure 4 C captures the high heterogeneity of the ECS and how fast the ECS distribution changes across hundred microns in live tissue. As for confocal imaging, this technique presents twice as better axial and lateral resolution, 500 nm x 200 nm respectively. Even then, the nanoscale organization of the ECS is not yet visible and is not compatible for imaging deep into tissue due to the low wavelengths used by confocal microscopy.

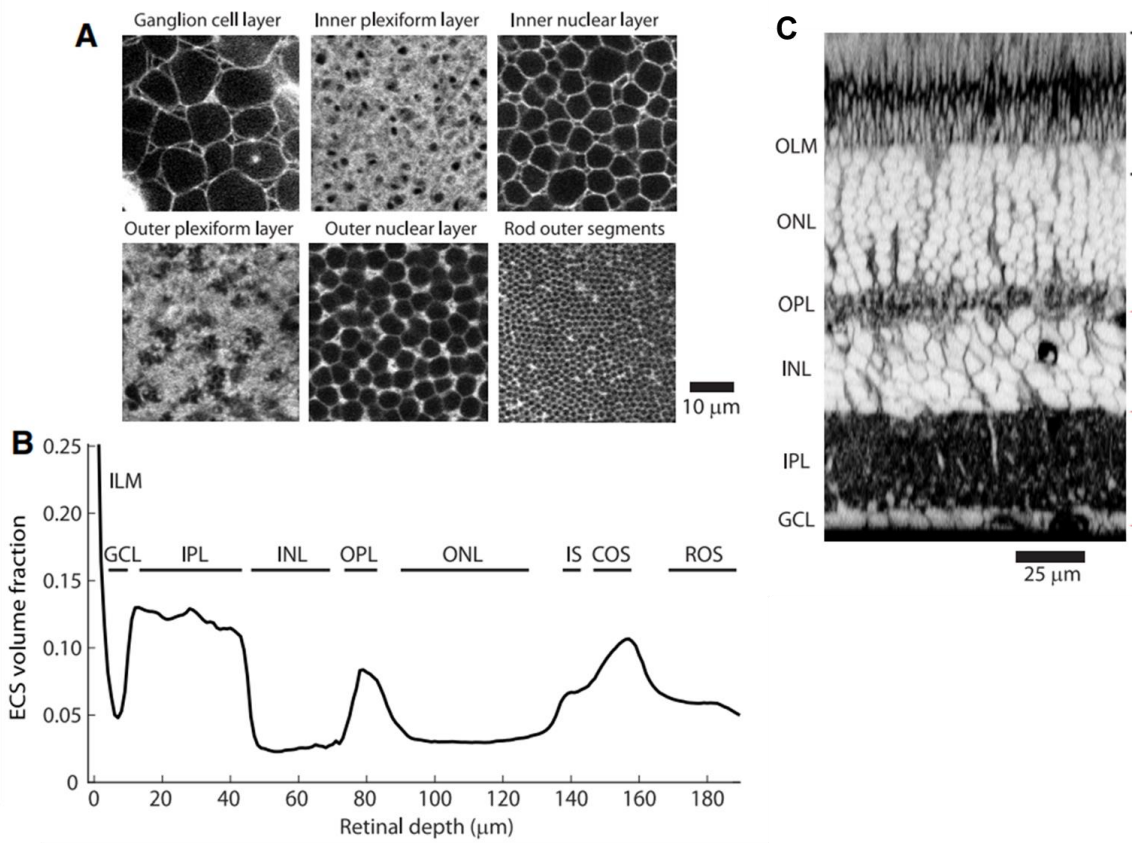

Figure 4 A) 2P shadow images of the different layers of the mouse retina labelled with 0.1 mM extracellular calcein. Scalebar 10 µm. B) ECS volume fraction of the different retinal layers ordered by retinal depth: inner limiting membrane (ILM), ganglion cell layer (GCL), inner plexiform layer (IPL), inner nuclear layer (INL), outer plexiform layer (OPL), outer nuclear layer (ONL), inner segment (IS), cone outer segment (COS) and rod outer segment (ROS). IS, COS and Ros are part of the outer limiting membrane (OLM). C) Z-stack reconstruction (1 µm step size) of retina. Image contrast is inverted showing calcein-labeled extracellular spaces in dark and cells in bright. The image illustrates the geometry of the different retinal layers: as indicated in B. Scalebar 25 µm. Modified image from *Kuo et al. (2020)*, [7].

Among the techniques that provide the highest resolution, electron microscopy (EM) has been widely used to visualized the nanoscale distribution of the brain neuropil and ECS. For a long time is has been the only source of images of the brain ECS. Although this technique provides detailed information of the brain ECS structure, it has one major disadvantage. EM requires tissue fixation and therefore is incompatible with live tissue imaging. In addition, classical chemical fixation is known to dehydrate the tissue and consequently shrink the extracellular compartment, [19], [20]. In comparison to classical fixation, it has been shown that cryofixation preserves better the ECS structure [20],as shown in Figure 5. Still, it has not been validated against real live tissue images.

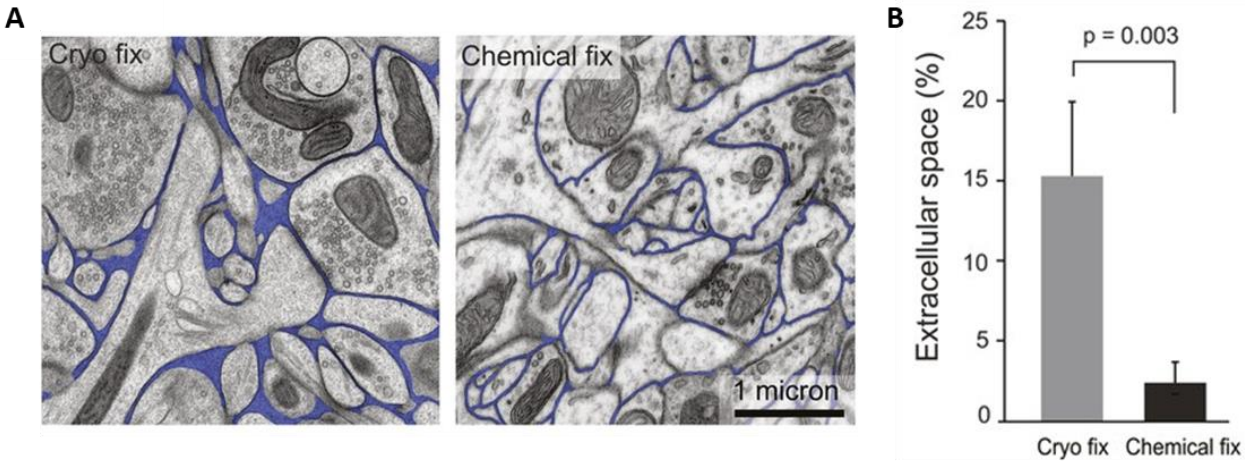

Figure 5 A) Electron microscopy images of the brain neuropil and ECS (in blue) from cryo-fixed (left) and chemically fixed (right) tissue. Scalebar 1 µm. B) Extracellular space volume fraction (α) comparison between cryo-fixed and chemically fixed tissue. Chemical fixation causes ECS shrinkage and underestimation of α. From *Korogod et al. (2015)*, [20].

Lately, super-resolution fluorescence microscopy techniques have become more popular to investigate the geometric nano-structure of the ECS. These techniques bypass the diffraction limit of light microscopy to increase spatial resolution. Particularly, super-resolution shadow imaging (SUSHI) was developed in 2018 by *Tønnesen et al.* to decipher the ECS sub-micron geometry in the dense brain parenchyma in live tissue [21] (Figure 6 A)., and it is based on 3D stimulated emission depletion (3D-STED) microscopy. STED microscopy generates super-resolved images through selective activation and then deactivation of fluorophores, thus, minimizes the area of illumination at the focal point while increases the achievable spatial resolution [22]. SUSHI works as the previously described 2P shadow imaging [7]. Live brain tissue slices are placed in a 3D-STED imaging chamber and perfused with an extracellular hydrophilic fluorophore that labels the interstitial fluid and makes cellular structures visible as shadows. Due to the extremely high spatial resolution of STED microscopy (50 nm laterally, 150 nm axially, [21]) with SUSHI we can recognized individual sub-cellular structures such us pre- and post-synapses and thus obtain images of the live neuropil like never seen before (Figure 6 B). In fact, since the interstitial fluid compartment is completely complementary to the ECS geometry, we can nearly fully optically resolve the ECS meshwork. In addition, SUSHI allows time-lapse imaging with good temporal resolution. The principal disadvantage of this technique, as happens with confocal microscopy is that the imaging depth is limited to 50 µm, though is sufficient to apply the technique in acute slices and in rodents *in-vivo*.

Another super-resolution microscopy approach to study the ECS consists on imaging and tracking fluorescent single-walled carbon nanotubes (SWCNTs) inoculated into the brain ECS *in-vivo* and in live tissue slices. This technique enables acquisition of real-time data on the dynamics of these nanotubes , from which nanoscale structure and local diffusion properties can be determined, [23] [24]. Still carbon nanotubes might be stuck and therefore stop providing dynamic

information, and spaces of the ECS smaller than these nanotubes will not be accessible and remain invisible.

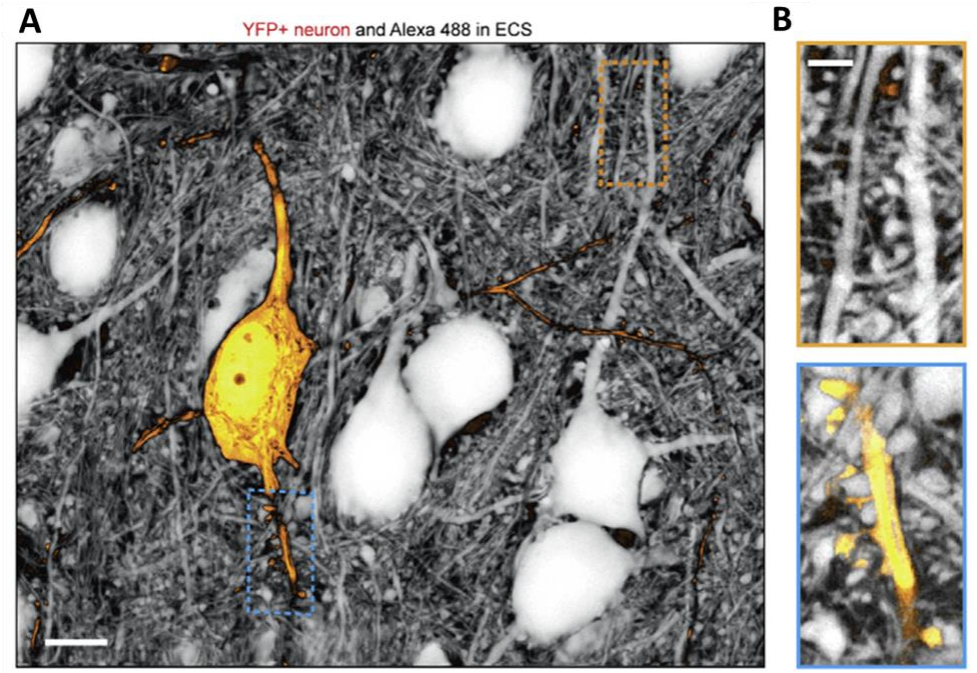

Figure 6 A) SUSHI image, illustrating a YFP-labeled CA1 neuron and the surrounding neuropil. Scalebar 10 µm. ECS channel was inverted so that cellular structures appear in white and interstitial fluid appears dark. YFP-channel was not inverted. (B) Zoom-in areas displaying unlabeled dendritic spines (top yellow box) and unlabeled presynaptic partners of YFP-labeled dendritic spines (blue bottom box). Scalebar, 2 µm. Borrowed from *Tønnesen et al. (2018),* [21].

Although many other different approaches have been used to investigate the ECS such us microfiber optical measurements [25], magnetic resonance imaging (MRI) [26], and time-resolved fluorescence anisotropy imaging (TR-FAIM) [27]; in this introduction we just described some of the most relevant ones for our work.

In contrast to what has been commonly accepted, the brain ECS is a highly dynamic structure. ECS volume changes have been reported in very different conditions and at different temporal scales. For instance, raising the potassium concentration 5 mM can cause ECS shrinkage and elicit seizure activity in the CA1 area of the hippocampus [28]. In fact, ECS shrinkage can elicit epileptiform activity in slices even when synaptic activity is blocked [29]. Multiple studies have shown that epileptiform activity can be induced by reducing the extracellular osmolarity which in turn reduces the ECS volume; while hyper-osmolar conditions produce the opposite effect [30], [31].On the other hand, recent work has reported that astrocytic microstructures swell after hypo-osmotic challenge at the expense of ECS microdomains, thus increasing the astrocytic-cellular interphase [32]. In pathological ECS, a recent study has reported enlarged ECS volume and increase diffusivity under degenerative conditions [24]. Also, It has been observed that the ECS expands during sleep to facilitate metabolite clearance through convective flow [33], [34].

This increase in ECS volume during sleep enhances diffusion and reduces the extracellular concentration of neurotransmitters, what in turn lowers the threshold for neuronal activity [6]. We hypothesize that these changes in ECS morphology will also shape cellular signaling at very different spatial and temporal scales.

More specifically, we are interested in how ECS volume changes affect GABAergic inhibition, the main source of inhibition in the brain and one of the most studied processes in the onset of epileptogenesis. We will further explain our interest in GABAergic tonic inhibition in the first part of this thesis.

In addition, we would like to verify if changes in ECS morphology also shape the diffusion of molecules in the interstitial fluid at any spatio-temporal scale. For that, we have developed a computational model based on SUSHI images to study diffusion in the live brain ECS on the synaptic scale, as it is described in the second part of this thesis.

PART 1: The extracellular space and GABAergic tonic inhibition

Introduction

Synapses can be excitatory or inhibitory in nature, depending on the main transmitter phenotype of the cell types involved. Glutamate is the main excitatory neurotransmitter that acts primarily through ionotropic glutamate receptors, including AMPA, NMDA and Kainate types. Glutamatergic AMPA receptors are the household receptors for excitatory signaling, and upon activation they open to allow primarily Na+ to enter the postsynaptic cell and give rise to a depolarizing current that brings the neuron towards action potential firing threshold.

GABA (gamma-aminobutyric acid) is the main inhibitory neurotransmitter in the brain, and is commonly released from somato-dendritic synapses that are formed directly on somata or dendritic trunks and not on spines. (Figure 7).

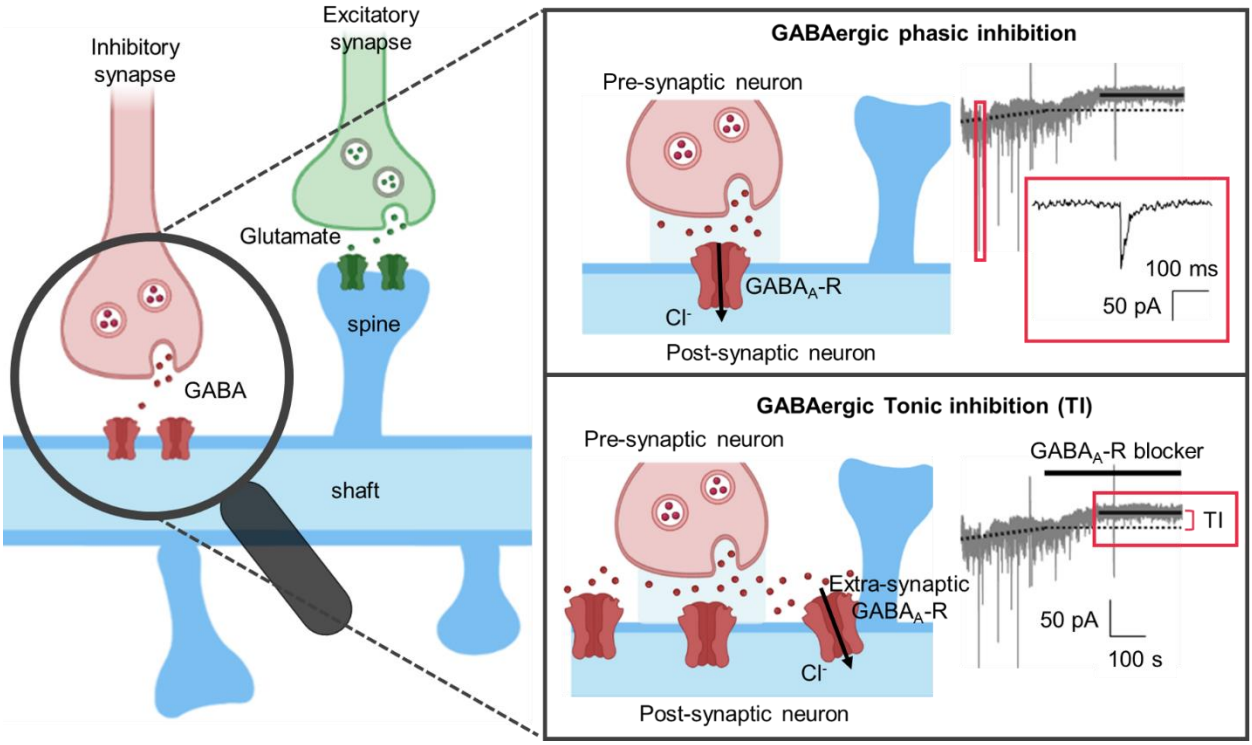

Figure 7 Graphical representation of the types of GABAergic inhibition. On the left, a GABAergic inhibitory synapse is represented at the dendritic shaft, and a glutamatergic excitatory synapse at the dendritic spine. On the right we have a more detail graphical explanation of the two types of GABA inhibition. Phasic inhibition (top panel) occurs when synaptic GABA release from the pre-synaptic neuron activates synaptic $GABA_A$ Receptors ($GABA_ARs$), leading to fast-inhibitory post-synaptic currents. Tonic inhibition (bottom panel) results from the slow and continuous activation of extra-synaptic $GABA_ARs$ by GABA spillover.

Upon activation, the ionotropic $GABA_A$ Receptor ($GABA_A$-R) becomes permeable to Cl- that enters the postsynaptic neuron to hyperpolarize it and bring it further away from action potential firing threshold. Synaptic GABAergic inhibition is also known as phasic inhibition (Figure 7). In addition to this phasic inhibitory effect, GABA escapes the synaptic-cleft through spill-over and activates extra-synaptic $GABA_A$-Rs on the same and other neurons through volume transmission [35], [36]. Notably, low ambient concentrations of interstitial GABA can result in a persistent tonic activation of extra-synaptic $GABA_A$-Rs to give rise to GABAergic tonic inhibition [37]–[39]

Given its sustained nature, tonic inhibition is a key player in controlling neuronal excitability [37], and it has been studied extensively in the context of pathological neuronal excitability such us epilepsy. Epilepsy is a complex neurological syndrome which affects to around 1% of the global population [40].It is characterized by neuronal hyperexcitability and sudden synchronized excitatory neuronal discharges that can manifest behaviourally as seizures. One of the most common and severe forms of epilepsy is mesial temporal lobe epilepsy (MTLE), and 70% of patients suffering from MTLE do not respond to currently available antiepileptic drugs [41].

MTLE is characterized by neuronal hyperactivity originating in the hippocampus. The hippocampal circuit in the brain connects the entorhinal cortex with the dentate gyrus (DG) through the perforant pathway. The DG granule cells send mossy fibers to CA3 pyramidal neurons, which send Schaffer collateral projections to CA1 pyramidal neurons, which send projections back to the entorhinal cortex (Figure 8). This trisynaptic circuit seemingly underlies the susceptibility for seizure generation. As a result, GABAergic inhibition in the hippocampus is key in controlling neuronal excitability [42].

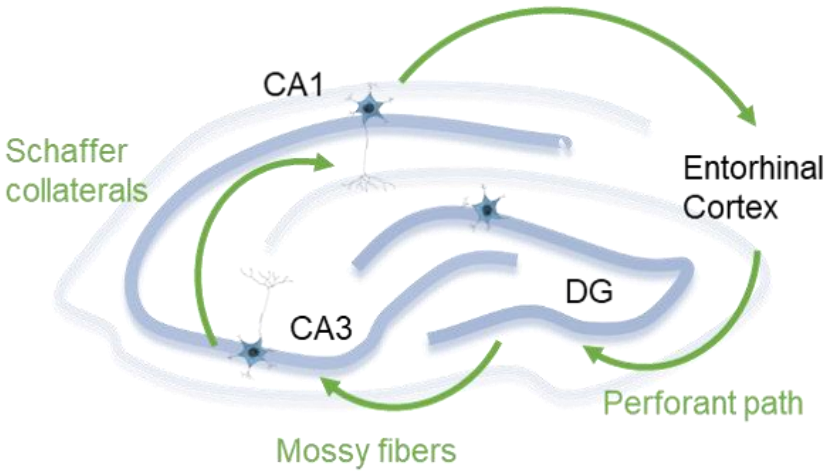

Figure 8 Graphical description of the trisynaptic hippocampal circuit. The entorhinal cortex connects with the dentate gyrus (DG) through the perforant pathway. DG granule cells send mossy fibers to the CA3 neurons, which connect with CA1 pyramidal neurons through Schaffer collaterals. CA1 neurons send projections back to the entorhinal cortex.

MTLE is commonly associated with hippocampal sclerosis, which consists of astrocytic proliferation, loss of dendritic spines, and neuronal death. However, it is unknown how these

structural changes translate into neural network hyperexcitability. It is expected that loss of interneurons and reduced number of GABAergic synapses would result in an overall decrease in GABA release and consequently reduced GABA concentration in the ECS and decreased phasic and tonic inhibition [43]. Though this is not the case, because while synaptic $GABA_A$ receptor mediated inhibition is reduced [44],experimental evidence shows that GABAergic tonic currents are maintained in hippocampal neurons after the epileptogenic period [45]–[47]. Some studies have even reported increased tonic inhibition [48]–[50]. In human MTLE and related animal models of MTLE there is reportedly a downregulation of α5 and δ extra-synaptic $GABA_A$ R subunits [46], [51]–[53] , which mediate GABA tonic inhibition in the hippocampus [54].

A possible explanation for the maintained/increased tonic inhibition in epileptic conditions could be maintained or increased extracellular GABA concentration. But from where does this extracellular GABA come from as there is less synaptic GABA released? Given the reduction of phasic inhibition in epilepsy, we can discard that such increase is due to enhance synaptic release. A possibility would be reversed or altered activity of GABA transporters (GATs), [43]. GATs play an important role in the reuptake of GABA after synaptic release. There are several GABA transporters (GAT1, GAT2 and GAT3) but GAT1 is the most important one in this function [55]. GAT1 is mainly localized in GABAergic axons and nerve terminals of pyramidal neurons, though it has also been found in astroglial processes, in oligodendrocytes and in microglia [56]. Even though recent studies suggest that GAT1 and GAT3 disfunctions are associated with MTLE and other types of epilepsy [57], [58],still little is known about the role of these GATs in epilepsy.

A common factor in many epilepsy models is astrocyte swelling. As water flows into cells causing cellular edema, the ECS shrinks [30]. One would predict that this reduction in extracellular volume fraction increases the effective concentration of ions and neurotransmitters in the brain ECS. This could explain the sustained hyperexcitability observed in epileptogenesis. As expected, neurons are very sensitive to changes in extracellular osmolarity and several studies show that epileptiform activity appears in hypo-osmolar conditions or can be abolished by increased extracellular osmolarity [59], [60].

We hypothesize that tissue swelling observed in MTLE would results in a decrease in extracellular volume fraction which consequently will increase the extracellular GABA concentration and enhance tonic inhibition. This could explain that we observe a maintained or even increased GABAergic tonic current while the phasic inhibition is reduced in settings of hyperexcitability.

Hypothesis & Objectives

The goal of the first part of this study it to evaluate if a general change in brain ECS volume in live tissue can affect cellular signaling globally.

We focus on the role of the brain ECS in GABAergic tonic inhibition, we hypothesize that cellular shrinkage during hyperosmotic conditions would results in an increase in extracellular volume fraction which consequently will decrease the extracellular GABA concentration and reduce tonic inhibition.

In order to test this hypothesis, first we will assess experimentally induced ECS volume changes using 2-photon shadow imaging in acute hippocampal mouse brain slices.

- We will assess our protocol to transiently expand the ECS during hyperosmotic conditions. This will allow us to consistently compare tonic inhibition under conditions of different ECS volumes.
- We will assess cell soma area changes during the hyperosmotic challenge, in order to confirm that ECS expansion is due to water coming out of cell soma causing cellular shrinkage

Then, we will evaluate if this hyperosmotic challenge protocol and its consequent increase in ECS indeed lead to a decrease in GABAergic tonic.

- We will measure GABAergic tonic inhibition in normo-osmolar and hyper-osmolar conditions to compare tonic inhibition for different ECS volumes.

In order to verify if ECS volume changes are enough to alter tonic inhibition we will investigate the effect of hyperosmotic challenge on synaptic GABA release, cellular properties and GABA uptake by GABA transporters.

- We will measure GABA synaptic release and we will evaluate cellular properties in normo-osmolar and hyper-osmolar conditions. This will allow us to confirm that any observed changes in Tonic inhibition are due to ECS volume changes and not to changes in synaptic release or cellular properties.
- We will measure GABAergic tonic inhibition in the presence of a GATs blocker both in normo-osmolar and hyper-osmolar conditions. Again, this will allow us to confirm that any observed changes in Tonic inhibition are due to ECS volume changes and not to changes in extracellular GABA uptake.

Materials & Methods

GABAergic Tonic Inhibition Measurement

Animals

The experimental work presented here was performed in acute brain slices from C57BL6J male wildtype (WT) mice used between the ages of 1 to 3 months. Mice were housed at 24 C with a 12-h light–dark cycle. They were provided with food and water *ad libitum* and with nesting materials.

All procedures were performed according to Spanish law (Real Decreto 53/2013, BOE 08-02-2013) and European Communities Council Directive (2010/63/EU) regulations; and were approved by the Ethics Committees of the University of the Basque Country EHU/UPV (M20-2017-006, M20-2020-098). All efforts were made to avoid animal suffering and to minimize mice pain and stress.

Solution preparation

All products where purchased from Sigma-Aldrich except when indicated.

Table 1 shows the composition of the dissection solution. The pH of the solution was 7.2-7.3.

Table 1. Dissection solution.

Compound	Molecular weigh	Concentration (mM)
Sucrose	342.3	195
Glucose	180.16	7
KCl	74.55	2.5
NaH_2PO_4	119.98	1.25
$MgCl_2$	95.21	7
HEPES	238.3	5
$NaHCO_3$	84.01	25
Na-Ascorbate	198.11	1
Na-Pyruvate	110.04	3
$CaCl_2$	147.01	0.5

Table 2 shows the composition of the artificial cerebrospinal fluid (ACSF). The pH of the solution was around 7.4 and the osmolarity between 300-310 milliosmoles/L.

Table 2 ACSF solution

Compound	Molecular weigh	Concentration (mM)
NaCl	58.44	119
KCl	74.55	2.5
NaH_2PO_4	119.98	1
$MgCl_2$	95.21	1.6
HEPES	238.3	5
$NaHCO_3$	84.01	26
Glucose	180.16	10
$CaCl_2$	147.01	2.5

Both solutions (Table 1 and Table 2) were continuously bubbled with 95% O_2 5% CO_2.

In order to model hyperosmotic stress condition, we prepared a hyperosmolar ACSF by increasing the osmolarity 50 milliosmoles with Mannitol (Fisher). Table 3 shows the composition of the solutions used in each condition.

Table 3 ACSF composition for hyperosmotic conditions. *The other components of the solution remained the same as in the control ACSF.*

Osmotic Condition	Mannitol	Osmolarity
Control ACSF	-	300-310 mOsm
Hyperosmolar ACSF	50 mM	350-360 mOsm

Table 4 shows the composition of the cesium-based high chloride intrapipette solution. The pH of the solution was around 7.2 and the osmolarity between 280-290 milliosmoles.

Table 4 Cs-based high chloride intrapipette solution.

Compound	Molecular weigh	Concentration (mM)
CsCl	168.36	135
NaCl	58.4	3.6
$MgCl_2$	95.21	1
HEPES	238.3	10
EGTA	380.35	0.1
Mg - ATP	507.18	2
Na_2 - GTP	523.18	0.4
QX-314 (Abcam)	343.31	5

In order to obtain stable recordings and keep the ionic balance in the hyperosmotic condition we added Mannitol to the Cs-based high Cl intrapipette solutions as shown in Table 5.

Table 5. Intrapipette solution for hyperosmotic conditions. The other components of the intrapipette solution remained the same as in the control Cs-based high Cl internal solution.

Osmotic Condition	Mannitol	Osmolarity
Control	-	280-290 mOsm
Hyperosmolar	50 mM	330-340 mOsm

Acute slices preparation

Mice were anesthetized with Isoflurane and decapitated. The brain was removed and placed in ice-cold dissection solution (Table 1) and the solution was continuously gassed with 95% O_2 5% CO_2. The tissue was cut using a vibratome (Precisionary Compresstome VF-300) into 300-350 µm hippocampal slices as shown in Figure 9 from *J. Bischofberger* protocol [61]. The slices were collected and incubated in dissection solution in a custom-made submerged chamber at 37 ^{0}C for at least 30 minutes. After this incubation period, the slices were transferred and kept into oxygenated ACSF (Table 2) at room temperature until the experiment began.

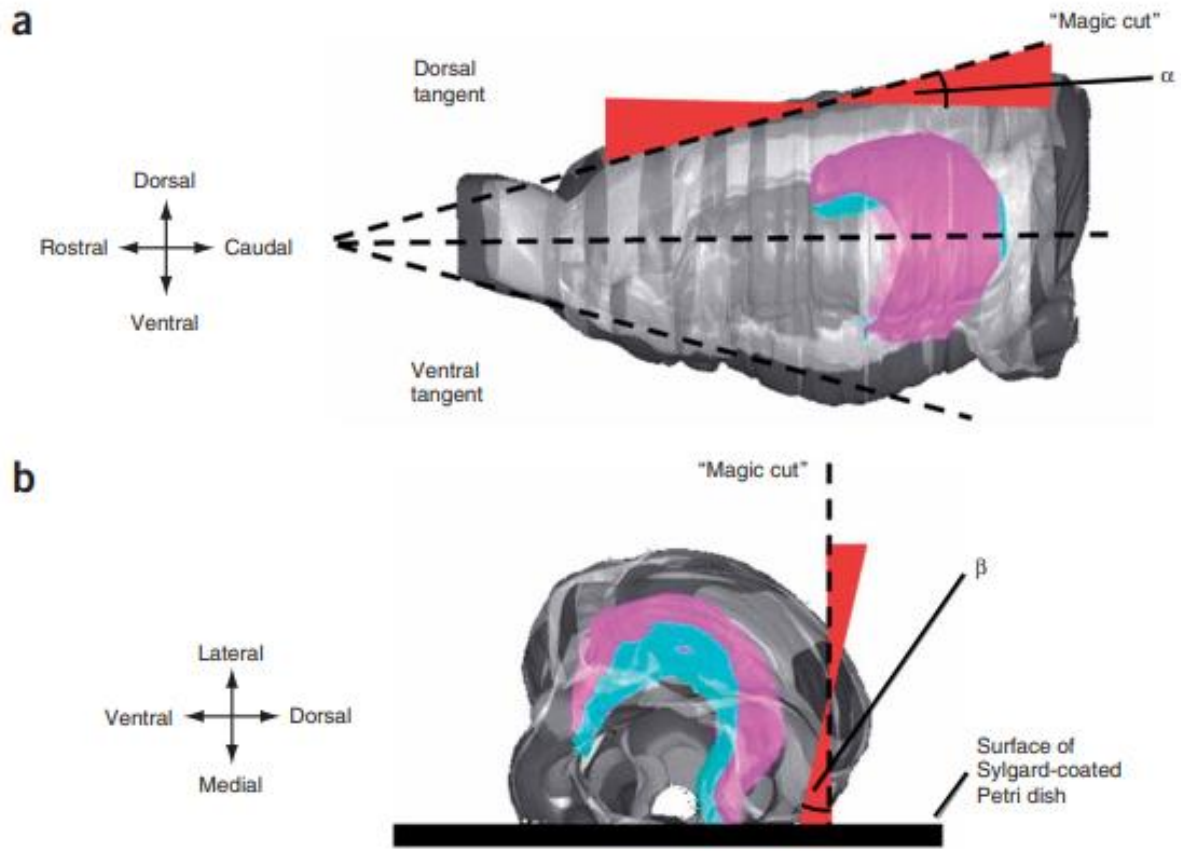

Figure 9. Schematic illustration of the ‘‘magic cut’’. (a) View of the left hemisphere from top. Red sectors indicate the range of ‘‘magic cut’’. (b) View of left hemisphere from caudal. Red sectors indicate the range of ‘‘magic cut’’. The optimal values for α and β for CA1 pyramidal cell recording are around 10 °. Magenta corresponds to CA3 and CA1 regions; cyan corresponds to dentate gyrus.

Electrophysiological Recordings

The slices were placed in a recording chamber on the microscope's stage and they were continuously perfused with the corresponding ACSF for each condition (Table 3) at 35 ºC. Hippocampal CA1 pyramidal neurons were visually identified using an MCI Clever Scope set up, and recorded with a HEKA EPC10 double amplifier. The recordings were made using glass micropipettes (Science Products, Hofheim, Germany) pulled with a vertical puller (NARISHIGE PC-10) with tip resistances between 3-6 MΩ. The pipettes were filled with the corresponding cesium-based high chloride internal solution for each condition (Table 5). We added 1 mg biocytin per 500 µL of intrapipette solution to label the patched neurons.

Whole-cell voltage-clamp continuous recordings were performed at −70 mV. The access resistance was estimated from test pulses evoked by a 5-mV voltage command step every 4 minutes of recording. Recordings were discarded if the access resistance changed by more than a 20%, or if the access resistance surpassed 35 MΩ at any time during the experiment. The electrophysiological data was sampled at 10 kHz and filtered at 2.9 kHz.

After 4 minutes of stable recording, we recorded GABAergic tonic inhibition by adding 100 µM Picrotoxin (PTX, Abcam) to the perfusion ACSF to block all $GABA_A$-Rs. The recording was maintained during this process and lasted until the PTX effect was observed and the signal was stabilized again (Figure 10). GABAergic tonic inhibition was measured both in control and hyperosmotic conditions. In addition, 3 mM Kynurenic Acid (KY, Sigma-Aldrich) was added into the recording solution in all the experiments to block glutamate receptors. In a group of experiments, 1 mM Nipecotic Acid (NIP, Abcam) was also added to the recording solution to block all GABA Transporters (GATs).

Data Analysis

The electrophysiological data was analysed using a custom-built MATLAB (MathWorks, R2019b) program. First, the raw signal was filtered to preserve the baseline of the recording and a line was fitted to the first 4 minutes to observe the tendency of the signal. GABAergic Tonic Inhibition was calculated as the change in current before and after adding PTX (Figure 10 C). To do so, we compared the mean of the last 30 seconds of the fitted line before blocking GABAergic inhibition with PTX, with the mean current of the first 30 seconds after steady-state effect of PTX. We measured GABAergic tonic inhibition both in control and hyperosmotic conditions, as well as in the presence of NIP.

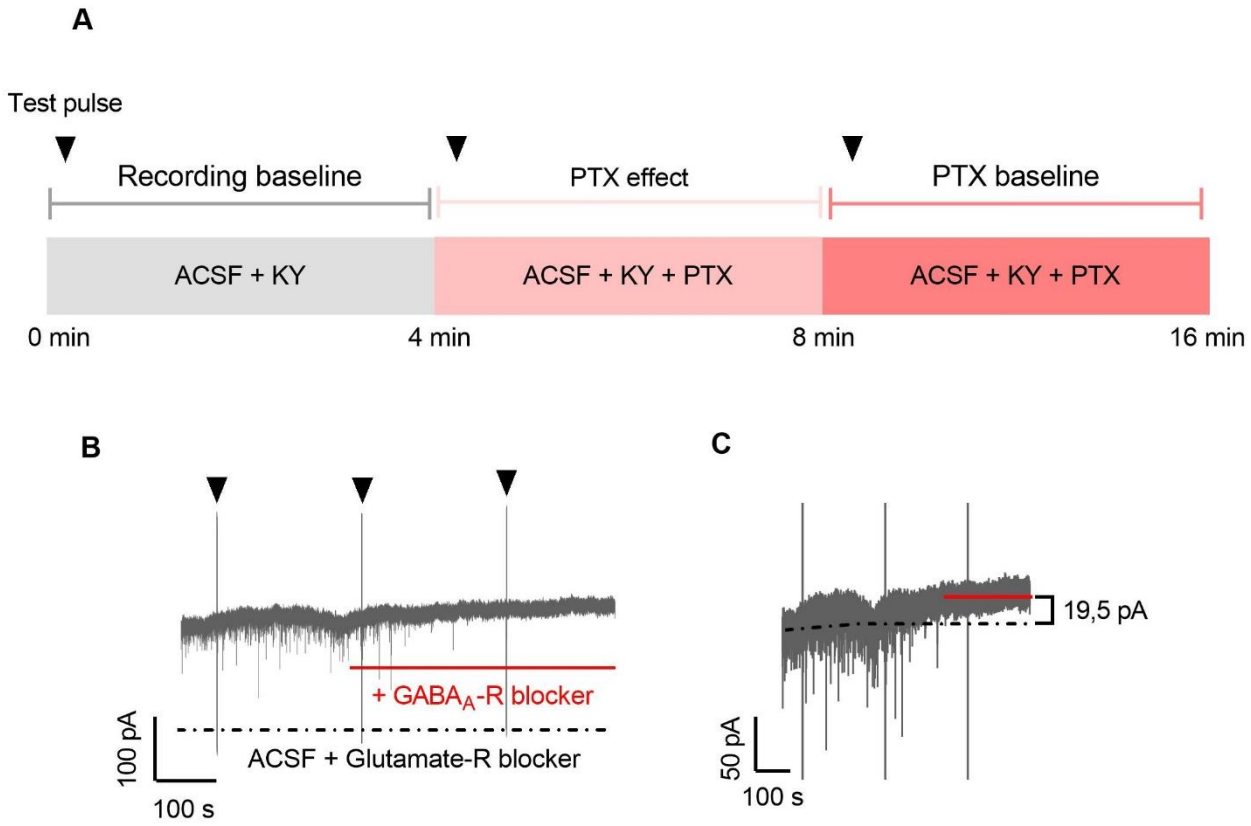

Figure 10. GABA tonic inhibition measurement scheme. A) Experimental timeline for the measurement of GABAergic tonic inhibition. Triangles represent test pulses taken every 4 minutes of recording. First the slice was perfused with ACSF + Kynurenic acid (KY) a glutamate receptor (Glutamate-R) blocker (gray). After 4 minutes of stable baseline, the slice was perfused with ACSF + KY + Picrotoxin (PTX), a $GABA_A$-R blocker. PTX took around 4 minutes to make effect and stabilized again (light red), so after that time, we recorded another 4 minutes of PTX stable baseline (dark red). B) Representative recording of 16 minutes of GABA tonic inhibition measurement. C) Representative recording of GABA tonic inhibition measurement. Y axis is amplified to show how the tonic inhibition is estimated as the difference between the recording and the PTX baselines.

In addition, we analysed GABA synaptic released in NormoOsmolar and HyperOsmolar conditions. To measure GABA synaptic release frequency and amplitude in each condition we used a function in our custom-built Matlab program that identified individual $GABA_AR$-mediated synaptic currents. Then the function estimated the number of events per second from the first 4 minutes of stable recording as well as the average amplitude in each condition.

All data was visualized and statistically analysed in GraphPad Prism. Control and hyperosmotic conditions data were presented as median with maximum and minimum values and individual measurements. An unpaired Student's t-test was used for statistical analysis between the two groups with a significance level of 5%.

Immunohistochemistry

To identify patch-clamped neurons and to label astrocytes, the slices were collected from the recording chamber after each successful experiment and placed in 4 % paraformaldehyde (PFA,

Sigma-Aldrich) for at least 1h. After fixation, the slices were washed with PBS and then stored at -20 °C in a cryoprotectant (PBS + 30% sucrose).

After accumulation of several slices, we defrosted them at room temperature under agitation and washed them first with PBS and then with a TRIS-buffered saline (TBS) solution with 0.25% Triton (Alfa Aesar) and 1% horse serum (HS, GIBCO). The sections were blocked with a blocking solution (TBS, 0.25% Triton, 4% HS) for 1 h before the overnight incubation with the primary antibody (1:1000 rabbit anti-GFAP in TBS, 0.25% Triton, 1% HS) at room temperature. After rising again (TBS, 0.25% Triton, 1% HS) the slices were incubated for 4h with the secondary antibody (1:400 Goat Anti-Rabbit IgG H&L Cy3, in TBS, 0.25% Triton, 1% HS) to label astrocytes and with Streptavidin (1:200 Native Streptavidin protein Cy5 in TBS, 0.25% Triton, 1% HS) to label de patch-clamped neurons. The brain sections were mounted on a glass slide using Moviol (Sigma-Aldrich) embedding medium (3.75 g of Moviol in 12.5 mL of glycerol, 37.5 ml of TBS [0.1 M, pH 8.5], 125mg DABCO).

Fluorescent cells were imaged on a Carl Zeiss ApoTome2 microscope (inverted Axio Observer).

All antibodies were purchased from Abcam.

Two-Photon Shadow Imaging

Animals

For these experiments, we used the same animals with same ages and in the same conditions as the animals used in the GABAergic Tonic Inhibition Measurement section (Animals)

Solution preparation

For the two-photon shadow imaging (2PSI) experiments we used the same dissection medium and ACSF as described in the GABAergic Tonic Inhibition Measurement section (Table 1 and Table 2).

Again, to model hyperosmotic stress condition, we prepared a hyperosmolar ACSF as shown in Table 3

Acute slices preparation

Acute slices for the 2PSI experiments were prepared as described in the GABAergic Tonic Inhibition Measurement section (Acute slices preparation)

Two-photon microscope

All images were acquired in a two-photon Femtonics 2D upright microscope (Olympus BX61 WI) we used 4X Olympus objective to identify the Hippocampal CA1 region and a 20x water immersion Olympus objective was used during the image acquisition. The step up consists of a Spectra-Physics MAI THAI (HPDS-007) laser and all images were taken at 810nm.

Extracellular labelling and Imaging

For the osmotic stress experiments the slices were transferred to an imaging chamber and perfused (1-2 mL/min) with ACSF at 36 °C. Hippocampal CA1 pyramidal neurons were identified

using bright-field microscopy. To label the extracellular space we switched the perfusion medium to ACSF with 40µM calcein disodium salt (Sigma-Aldrich). After 8 minutes of perfusion with calcein the dyed had filled completely the slice and we started our imaging protocol.

We took a z-stack of 4-5 frames with a z-width of 1.5 µm every 3 minutes during at least 30 minutes. Z-stacks were taken to correct for drift in the z-plane focus during the experiment. For the hyperosmotic condition, after acquiring 3-4 z-stacks we changed the perfusion solution to the hyperosmotic ACSF with 40µM calcein during 15 minutes and then back again to the control ACSF with calcein.

Image and Data Analysis

All images were processed and analyzed using ImageJ software. For each experiment, we obtained a x, y, z, t hyper-stack of 4-5 z-planes per time-point. We manually went through each image in the stack to identify the images corresponding to the same z-plane of focus and generate a time-lapse from the hyper stack. After performing a stack-registration on the time-lapse using ImageJ translation we adjusted the brightness and contrast using ImageJ's '*Brightness and Contrast'* function. No other image processing, such as deconvolution, was applied.

Fluorescence intensity within areas of interest was measured in ImageJ using the area '*Measure*' function. We measured fluorescence intensity at 4 different areas of interest for each time-point avoiding big cellular structures such as somata. The fluorescence intensity was then averaged for each frame and normalized with respect to the first frame. Cell soma area was measured over time for 1 to 3 cells per experiment using ImageJ '*Measure'* function. Area measurements were again normalized with respect to the first frame of the time-lapse.

All data were represented and statistically analysed in GraphPad Prism. To compare hyperosmotic and control conditions both between and within groups, data were represented as mean with maximum and minimum values and individual points before during and after the osmotic stress. 2 ways ANOVA statistical analysis was used to compare between and within groups. The significance level was set at 5%.

Results

ECS volume increases after hyperosmotic stress

To investigate how changes in osmolarity affect the ECS volume we temporarily raised the osmolarity of the perfusing ACSF (from 304 ± 3 to 352 ± 3 mOsm/L; mean ± SD) by adding mannitol (50mM) to the perfusion ACSF. The effect was observed by taking time-lapse 2-Photon Shadow Images (Figure 11 A) with a constant fluorophore concentration in control and hyperosmotic conditions.

Our hypothesis is that hyperosmotic extracellular conditions should drive water molecules from cells to the ECS. Thus, leading to an expansion of the extracellular compartment at the expense of cell volumes.

In agreement with this, during transient hypertonic conditions, we observed ECS swelling (n = 9 slices, Figure 11 A and B), as evident by an increase in ECS fluorescence intensity to 129 ± 17 % of controls (mean with SD, HyperOsmolar: n = 9 slices, NormoOsmolar: n = 8 slices; Šídák's multiple comparisons test, ** p-value = 0.0058), which dropped to 118 ± 22 % after reperfusion with normal ACSF (Figure 11 C and D).

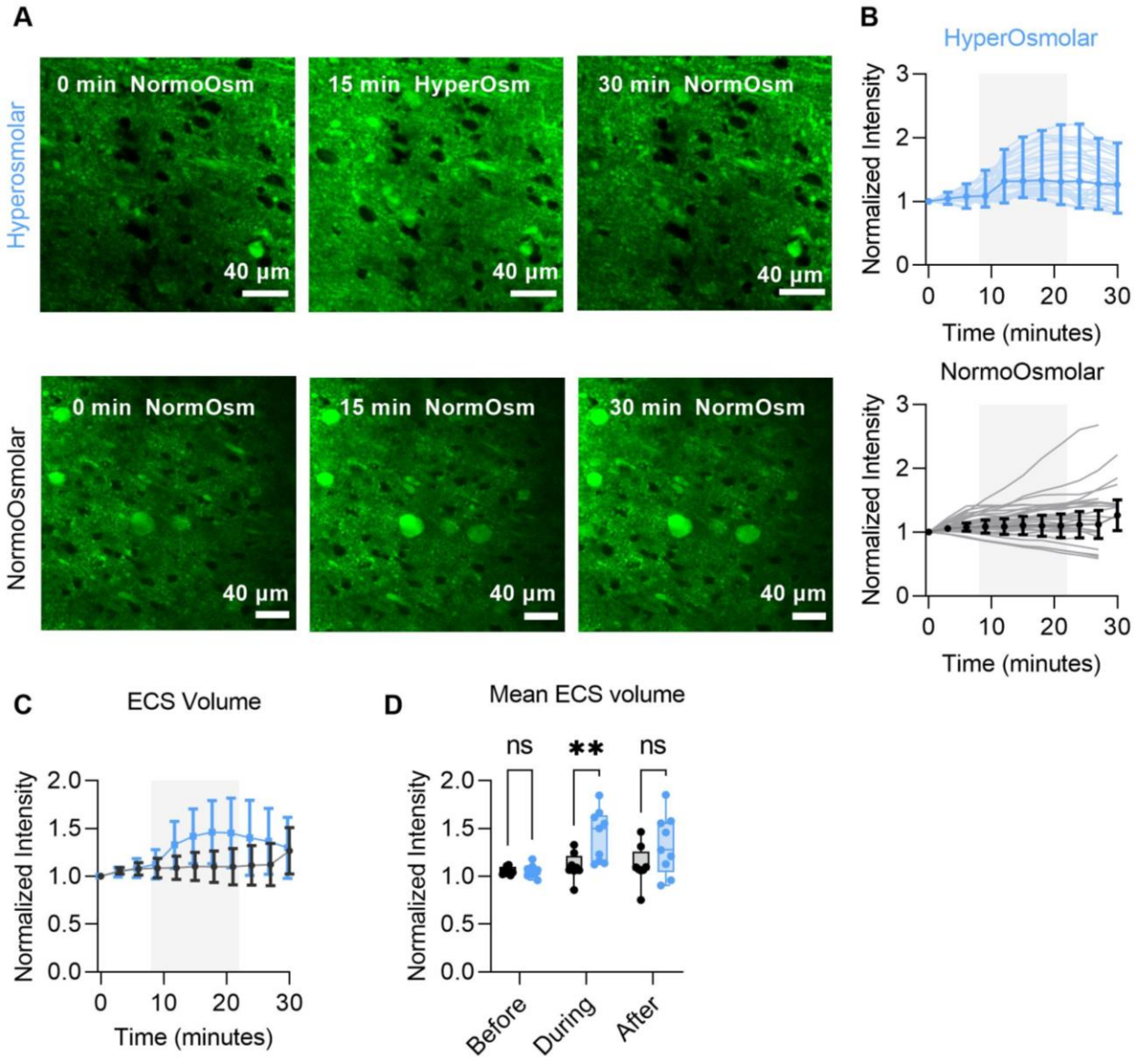

Figure 11. ECS volume A) 2PSI time-lapse sequence of the brain ECS in control conditions (NormoOsmolar) and during a transient hyperosmotic challenge (HyperOsmolar). B) ECS normalized intensity across individual frames during HyperOsmolar (n=9 slices, blue) and NormoOsmolar conditions (n=8 slices, black). C) Mean and SD of the normalized intensity in HyperOsmolar and NormoOsmolar conditions. D) ECS mean intensity measured before during and after the hyperosmotic challenge. Each point represents the mean intensity of the frames corresponding to each scenario before during and after from n=9 slices (HyperOsmolar) and n= 8 slices (NormoOsmolar). Asterisks report result from Šídák's multiple comparisons test. The transient increase in osmolarity triggered a transient increase in ECS intensity, consistent with an increase in ECS volume fraction.

In addition, we noticed a reduction in the cell soma area that coincided with the increase in ECS volume (Figure 12 A and B). Cell soma area was measured quantitatively and normalized before during and after the osmotic challenge and our data show a reduction in cell soma area to 63 ± 18 % of controls (mean with SD, HyperOsmolar: n = 9 slice, NormoOsmolar: n = 8 slices; Šídák's multiple comparisons test, * p-value = 0.0113), which raised to 85 ± 12 % after reperfusion with normal ACSF (Figure 12 C and D).

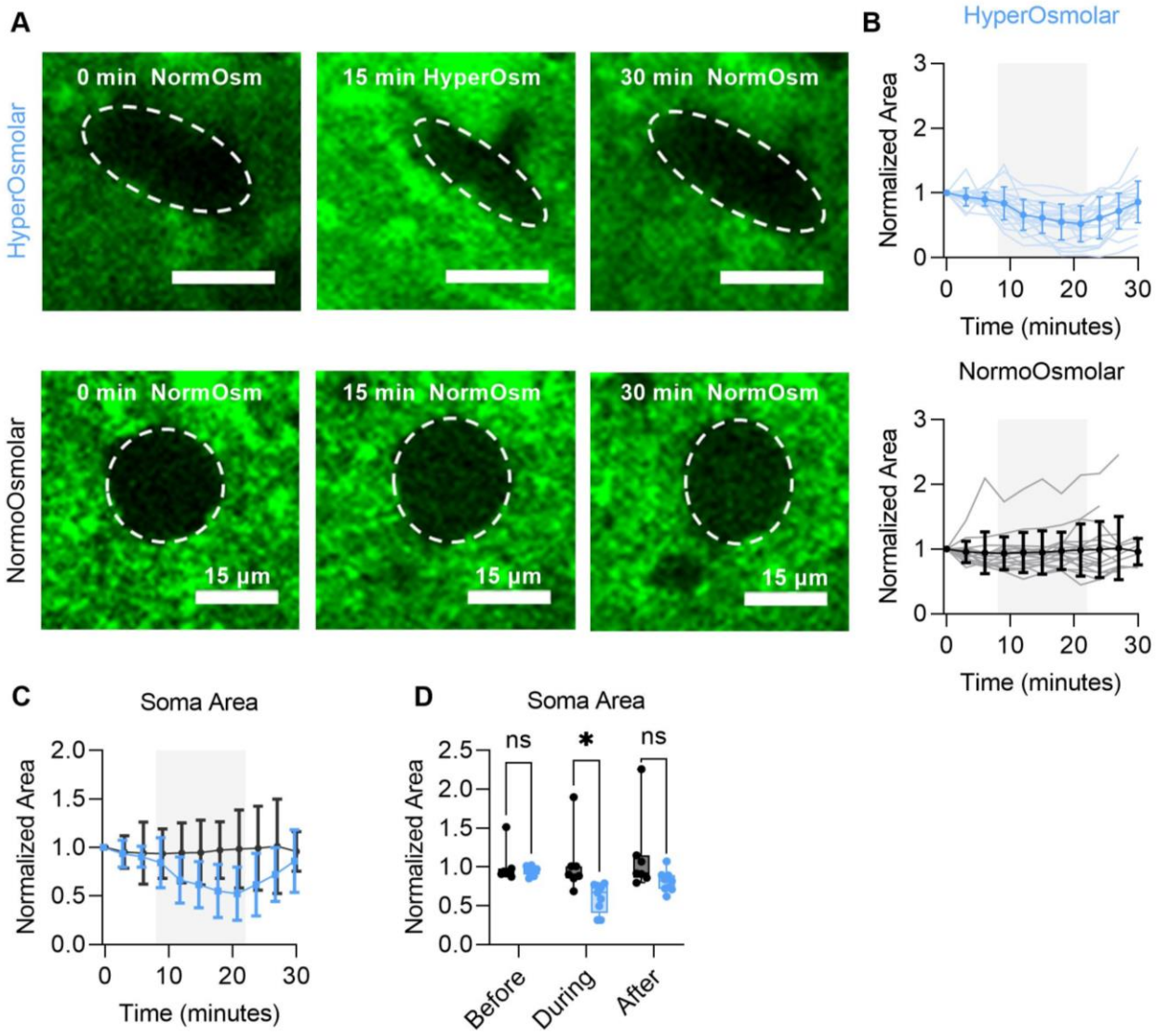

Figure 12. Cell soma area. A) 2PSI time-lapse sequence of a cell soma in control conditions (NormoOsmolar) and during a transient hyperosmotic challenge (HyperOsmolar). B) Normalized soma area across individual frames during HyperOsmolar (n=9 slices, blue) and NormoOsmolar conditions (n=8 slices, black). C) Mean and SD of the normalized area in HyperOsmolar and NormoOsmolar conditions. D) Cell soma mean area measured before during and after the hyperosmotic challenge. Each point represents the mean area of the frames corresponding to each scenario before during and after from n=9 slices (HyperOsmolar) and n=8 slices (NormoOsmolar). Asterisk reports result from Šídák's multiple comparisons test. The transient increase in osmolarity triggered a transient decrease in cell soma area, consistent with a decrease in cell soma volume.

Together these results indicate that increased osmolarity of the interstitial fluid drives water molecules out of cells causing presumed neuronal cell soma to shrink while the ECS volume reciprocally expands.

GABAergic Tonic Inhibition decreases after hyperosmotic stress

After verifying that transient hyperosmotic conditions increase ECS volume, we aimed to understand how swelling of the extracellular compartment affects GABAergic tonic inhibition. We reasoned that, all other things equal, increasing the ECS volume will dilute the extracellular GABA available to activate extra-synaptic $GABA_A$ receptors, and therefore will reduce GABAergic tonic inhibition without changing synaptic GABAergic transmission. To examine this hypothesis, we measured tonic inhibition both in control and hyperosmotic conditions. To discard the possibility that any observed changes in tonic inhibition during hyperosmotic conditions are due to altered synaptic release, we in parallel analyzed the amplitude (Figure 13 A) and the frequency (Figure 13 B) of inhibitory post-synaptic currents (IPSC) in NormoOsmolar (n=12 slices) and HyperOsmolar (n=14 slices) conditions. The results show that synaptic release of GABA is not affected by changes in the extracellular osmolarity, which is true for both the amplitude and the frequency (unpaired t-test, p = 0.5596 and p = 0.5459 respectively). In addition, Figure 13 D and F show representative test-pulses taken before and after blocking $GABA_A$Rs, and these confirm that cell membrane properties where preserved during the whole recording.

Then, we measured tonic inhibition in the CA1 pyramidal layer of the hippocampus (Figure 14 B), both in NormoOsmolar conditions (301 ± 3.5 mOsm, mean with SD, n=12 slices) and during HyperOsmolar conditions (353.9 ± 3.1 mOsm, mean with SD, n=14 slices). Increasing the osmolarity of the perfusing medium a 17 ± 1 % resulted in a 62.4 ± 24.1 % decrease in GABAergic tonic inhibition (from 24.5 ± 19.8 pA mean with SD, n=12 slices, to 9.2 ± 9.3 pA mean with SD, n=14 slices, unpaired t-test, p =0.0162), as show in their respective representative traces (Figure 14 D and E).

Finally, we evaluated if this decrease in GABAergic tonic inhibition observed in hyperosmolar conditions was due to an increased GABA uptake by GABA transporters (GATs). To do so, we measured tonic inhibition after blocking all GABA transporters with nipecotic acid (NIP), as shown in Figure 14 C. Once again, experiments were carried both in NormoOsmolar conditions (304 ± 2.7 mOsm, mean with SD, n=9 slices) and during HyperOsmolar conditions (352.0 ± 3.2 mOsm, mean with SD, n=10 slices). Increasing the osmolarity of the perfusing medium resulted in a tendency of GABAergic tonic inhibition to decrease (from 289.0 ± 78.19 pA mean with SD, n=9 slices, to 230.34 ± 78.39 pA mean with SD, n=10 slices, unpaired t-test, p =0.1214), as shown by their respective representative traces (Figure 14 F and G). Though the observed tendency was strong, the decrease was not significant. We predict that the effect may turn significant when we increase the sample number to obtain sufficient power for testing for the relatively modest numerical effect, based on the effect size in the conditions of not blocking GATs.

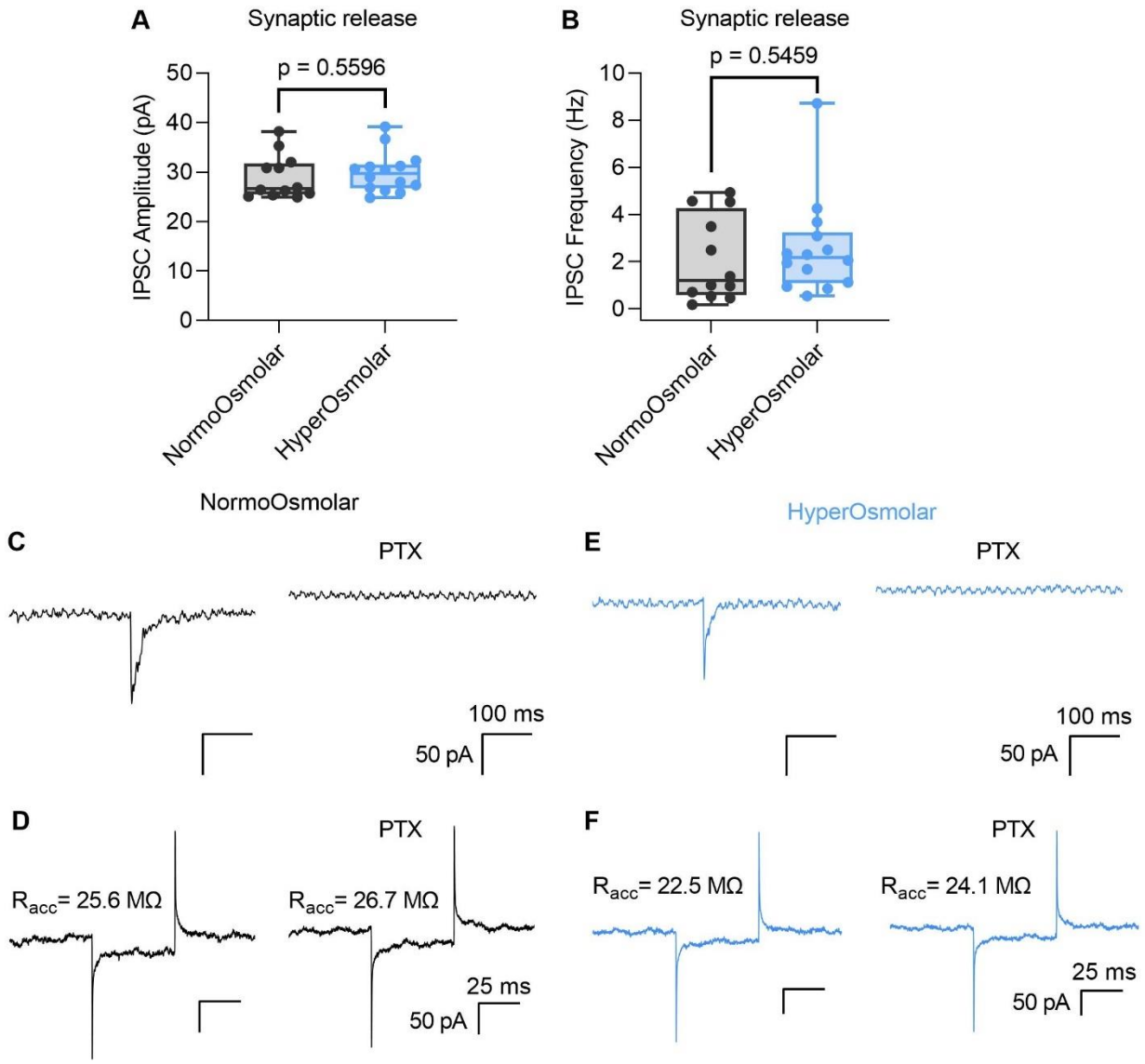

Figure 13. A) IPSC amplitude, each individual point represents the mean amplitude over a period of 4 minutes for NormoOsmolar (n = 12 slice, black) and HyperOsmolar conditions (n = 14 slices, blue), results report non-significant difference (p = 0.5596, unpaired t- test). B) IPSC frequency measured over a period of 4 minutes for NormoOsmolar (n = 12 slice, black) and HyperOsmolar conditions (n = 14 slices, blue), results report non-significant difference (p = 0.5459, unpaired t- test). C, E) Representative IPSC event before and after blocking GABAergic inhibition with picrotoxin (PTX) 100µM in NormoOsmolar and HyperOsmolar conditions respectively. D, F) Representative test pulse before and after blocking GABAergic inhibition with picrotoxin (PTX) 100µM in NormoOsmolar and HyperOsmolar conditions respectively.

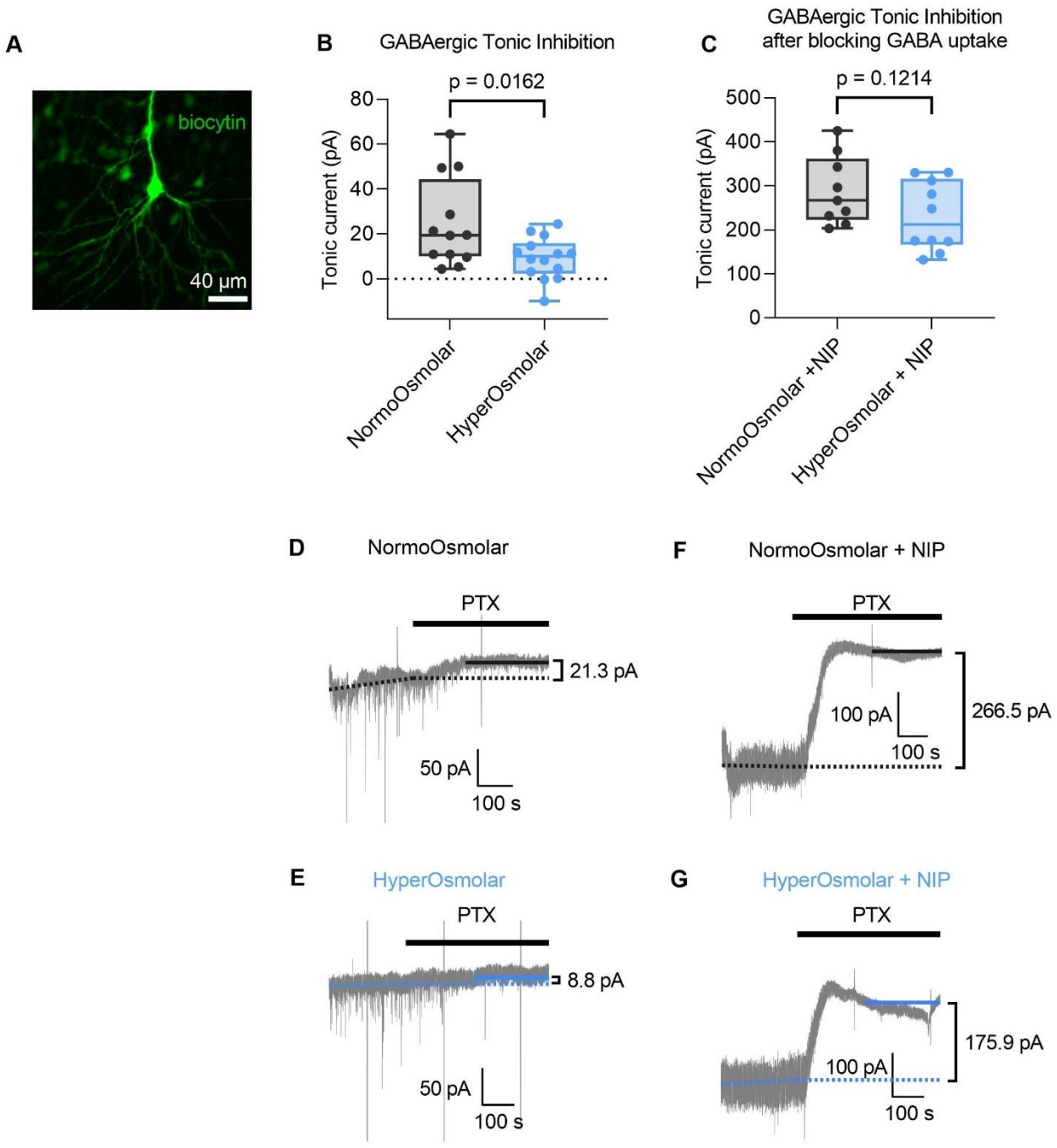

Figure 14 A) Biocytin labelled CA1 pyramidal neuron of the hippocampus. B) GABAergic tonic inhibition measurements represented as median with maximum and minimum values and individual points in NormoOsmolar (n = 12 slice, black) and HyperOsmolar conditions (n = 14 slices, blue). Results report significant difference between NormoOsmolar and Hyperosmolar conditions (p = 0.0162, unpaired t- test). Increased osmolarity lead to a reduction in GABAergic tonic inhibition. C) GABAergic tonic inhibition measurements after blocking GABA uptake with nipecotic acid (NIP), represented as median with maximum and minimum values and individual points in NormoOsmolar (n = 9 slice, black) and HyperOsmolar conditions (n = 10 slices, blue). p = 0.1214 reports the result from unpaired t- test. D, F) Representative trace of a measurement of tonic inhibition in NormoOsmolar conditions before and after blocking GABA uptake. C, E) Representative trace of a measurement of tonic inhibition in HyperOsmolar conditions before and after blocking GABA uptake.

Discussion

Reduction of the ECS volume fraction due to hypo-osmotic conditions has been shown to induce epileptiform activity while expansion of the ECS reverses this effect [30], [31]. Unexpectedly, experimental evidence shows that GABAergic tonic inhibition is sustained or even increased in hippocampal slices after experimental epileptogenesis [45]–[47], even when synaptic GABAergic inhibition is reduced [44]. The purpose of this part of the study was to investigate whether hyper-osmotic conditions that increase ECS volume through cell shrinkage can have a dilution effect on GABA in the interstitial fluid and thereby reduce tonic inhibition independently on synaptic release mechanisms and GABA receptor functional states.

ECS volume changes were assessed using two-photon shadow imaging technique in acute hippocampal mouse brain slices. As predicted, raising the osmolarity of the interstitial fluid led to a transient expansion of the extracellular space. In addition, we provided measurements of cell soma area during hyperosmotic challenge, for the first time. Thus, confirming that ECS expansion in hyperosmolar conditions is due to water coming out of cell soma causing cellular shrinkage. These results are in line with previous studies in the field. *Tønnesen et al.* reported a transient ECS expansion in acute brain slices during perfusion of hyperosmolar ACSF. Hyperosmotic conditions consisted on raising the osmolarity from 300 to 380 mOsm using NaCl, and the observed ECS expansion corresponded to a 20% increase in ECS fluorescence intensity [21]. On the other hand, swelling of astrocytic microstructures at the expense of ECS pools has been observed during hypo-osmotic conditions, by reducing the osmolarity of the normal ACSF from 300 to 200 mOsm [32].

Next, we used whole cell patch-clamp electrophysiological recordings to evaluate the effect of hyper-osmolar conditions on GABAergic tonic inhibition. Our results showed that, under hyper-osmotic stress, $GABA_A$-R mediated tonic current significantly decreases. This effect on tonic inhibition could be explained by the fact that hyperosmolar conditions expand the ECS. We expect that increased ECS volume would dilute the extracellular GABA available and thus reduce the GABA concentration that would potentially activate extra-synaptic $GABA_A$Rs. GABA release and GABA receptor independent regulation mechanisms of tonic inhibition may help explain why GABAergic inhibition is maintained or even increased while synaptic GABA release is reduced in epileptic conditions [42]–[45]. ECS volume reduction due to astrocytic swelling is one of the landmarks of epilepsy [30]. Given our results, one would expect that ECS shrinkage would increase the extracellular GABA concentration and overcome the lower synaptic GABA release observed in epileptogenesis. Thus, tonic inhibition could be maintained in epileptic conditions. We are currently working on measuring tonic inhibition in hypo-osmotic conditions, though this is more difficult to design experimentally, as we have to effectively use a non-physiological ACSF with low ionic osmolarity.

Notably, we verified that increased osmolarity did not alter GABA synaptic release frequency or amplitude, and that the cellular properties (such as cell membrane and access resistances) were

maintained during the whole experiment. Altogether, these results support the idea that the ECS can modulate signaling independently of classical neuronal parameters, such as release probability, vesicular quantal size, and receptor states, and that sustained GABAergic tonic inhibition in epilepsy may be related to a reduction in ECS volume.

Another plausible explanation for the constant level of $GABA_AR$-mediated tonic current during epileptogenesis could be the decreased expression of GABA transporters. It has been reported a reduced expression of GAT-1 and GAT-3 after kainate injection but an increased expression of the Betaine/GABA transporter (BGT-1) in the rat hippocampus [62]. BGT-1 is localized on dendrites of neurons in the cortex and hippocampus and it uses both GABA and betaine, which is thought to be a protective osmolyte in the brain[62]. On one hand, low expression of GAT-1 and GAT-3 might lead to less GABA uptake by neurons and astrocytes, respectively. This in turn, would translate in more extracellular GABA available to compensate for the decrease GABA synaptic release observed in epileptic conditions and activate extra-synaptic $GABA_AR$ mediating tonic inhibition. On the other hand, increased BGT-1 expression in glial cells could increase GABA uptake. Nevertheless, this effect most likely is very small as BGT-1 is a weak GABA transporter [62]. Still, the role of GABA transporters in epilepsy remains controversial, as various studies support all the hypothetical scenarios of unchanged up- or down-regulation of GAT-1, GAT-3 or BGT-1 [63]–[65]. These conflictive results could be a consequence of the high variability of models used to study epilepsy and the specific mechanisms that are affected in each of them. Another alternative to explain increased extracellular GABA levels in epileptic conditions is GABA transporters reversal. In physiological conditions, the main source of extracellular GABA in the hippocampus is supposed to be synaptic release and GAT-1 and GAT-3 operate in the normal mode removing GABA from the extracellular space. However, significant elevations of intracellular Na^+ could result in GAT-3 reversal. Indeed, elevated neuronal activity such us epileptic activity could reverse GAT3 transporter to release GABA and maintain GABAergic tonic inhibition [66]. Interestingly, it has been reported that GAT-1 mediated GABA uptake is not reversed during epileptiform activity [67].

Clearly, the role of GABA transporters in epilepsy is not yet understood and it seems to be mediated by complex mechanisms. Therefore, in this section we have investigated the role of GABA transporters in mediating GABA tonic inhibition in hyperosmotic conditions. Our results show a strong tendency for tonic inhibition to decrease in hyperosmotic conditions in the presence of a GAT blocker (NIP). Though with the current number of experiments (n) we don't see a significant difference between the control and hyperosmotic group, we expect that increasing the number of experiments will conclude that GABAergic tonic inhibition is also reduced in hyperosmotic conditions when blocking GABA uptake. These results would suggest that sustained GABA tonic inhibition in epileptic conditions could be explained by the reduction in ECS volume and that although other mechanisms, such as GABA transporters, may have a role, they are not the main players in the regulation of GABAergic tonic inhibition.

Conclusion

Regarding the first part of the thesis, *the extracellular space and GABAergic tonic inhibition*, our results prove that modifying the ECS structure globally can impact volume transmission.

First, our two-photon shadow imaging experiments reproduced the ECS expansion after raising the osmolarity of the interstitial fluid, in line with the literature. And for the first time, we provided measurements of cell soma area during hyperosmotic challenge. This confirms that ECS expansion is due to water molecules coming out of cells, leading to cell shrinkage.

More importantly, we investigated whether this changes in ECS volume affect volume transmission in the form of GABAergic tonic inhibition. Our results demonstrate that ECS expansion during hyper-osmolar conditions decreases GABAergic tonic inhibition. We verified that the reduction in tonic inhibition was independent of synaptic GABA release or membrane properties of the postsynaptic neuron.

Then we tested if the increase in ECS volume, in hyperosmotic conditions, also reduces $GABA_A$-R mediated tonic current when GABA uptake by GATs is blocked. Though our results in this regard are not conclusive, they show a strong tendency for GABA tonic inhibition to decrease. We predict that increasing the number of experiments will lead to a significant decrease in tonic inhibition.

In summary, this work suggests that changes in ECS volume due to osmotic stress have a relevant role in cellular signaling. ECS volume changes could explain the unexpected maintained GABAergic tonic inhibition observed in epilepsy. Although other mechanisms, like GABA uptake by GATs, are probably affected, we see a strong tendency to believe that GATs are not the main players in the sustained tonic inhibition during epileptogenesis. Still, more experiments need to be performed regarding the effect of hyper-osmolar ECS volume expansion in tonic inhibition when GABA uptake is blocked to reach conclusions.

PART 2: Computational modelling of microscale diffusion in brain ECS

Introduction

Transport of molecules in the brain occurs through different physical processes and pathways. Some ions and molecules move from one cell to another though gap junctions, intercellular channels that connect neighbouring cells. However, all remaining intercellular signalling occurs through the narrow interstitial fluid filled channels of the brain extracellular space (ECS). Small particles in aqueous medium move mostly stochastically by diffusion, which in essence is a passive physical transport mechanism where particle movement is driven by a concentration gradient. Particles move randomly from high concentration regions towards low concentration areas until equilibrium is reached (Figure 15). In addition, particles can move by advection, which is the movement of particles by bulk flow of fluid due to a pressure gradient. There is currently no consensus on whether or where there is interstitial fluid bulk flow in the brain, though there is compelling evidence that it occurs at least around perivascular spaces, i.e. the fluid-filled spaces that surround some arteries [68].

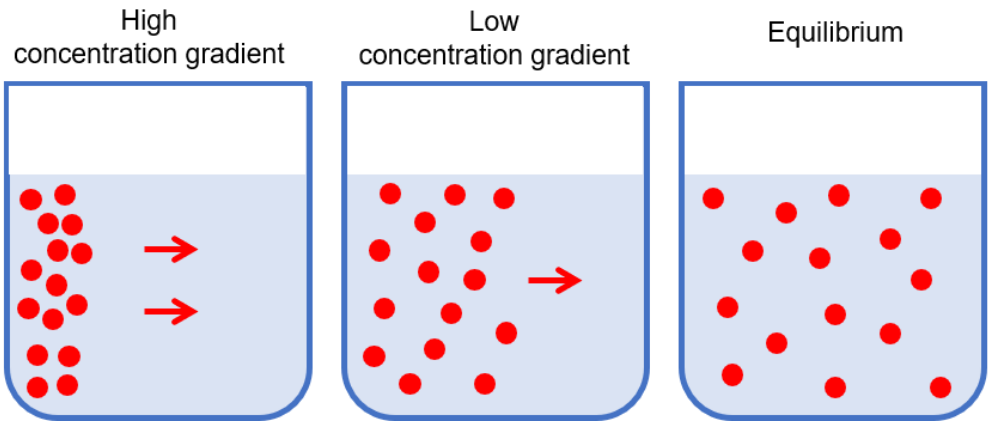

Figure 15. Graphical description of the diffusion process of particles moving from high to low concentration regions until equilibrium is reached.

The ECS is a highly dynamic compartment due to the relatively fast retraction or protraction of microglial process and to swelling/shrinkage of vessels, neurons and astrocytes. These dynamic phenomena occur frequently and span different timescales, from hours, as is the case of the ECS volume changes with circadian rhythm [33], to seconds , as cell swelling in hyper-excitatory epileptiform discharges [69], [70]. The ECS channels will change their morphology and thus, local ECS geometry changes will momentarily alter the diffusion pathways for intercellular signaling. The impact of ECS structure and dynamics on sub-micron scale diffusion of molecules in the live brain ECS is still not well understood, largely due to the lack of techniques reconciling live brain ECS imaging with nanoscale resolution and real time analysis of molecular diffusion.

In the past years, experimental techniques have been combined with mathematical and computational models to investigate diffusion in the brain parenchyma. Most experimental work done in the field over the last two decades is based on well-established proven techniques: real time iontophoresis (RTI) and integrative optical imaging (IOI) [13], [14], [71]–[74]. However, these provide very low spatial resolution and averaged information about the ECS geometry and diffusion properties. Though much less popular, magnetic resonance imaging (MRI) has been used to study diffusion of contrast agents in the *in-vivo* brain ECS [26]. MRI is an applicable tool to assess clearance by the glymphatic system on a regional or global scale, but its low spatial resolution limits its application to investigate local diffusion in the ECS, where it cannot resolve individual channels. Novel techniques, such as super-resolution shadow imaging (SUSHI) and single-walled carbon nanotube tracking (SWCNT), have opened the door to the nano-scale world in live tissue. Recently, SWCNT has been used to assess ECS diffusivity in the vicinity of a synapse in the living brain tissue [75], providing unprecedented data of the nanoscale diffusion properties of the live brain ECS. SUSHI, in turn, readily reveals ECS microstructure, though it has not yet been used to investigate diffusion in the brain parenchyma [21]. Two-photon shadow imaging (2PSI) has been implemented by *Kuo et al*. (2020) to visualize larger ECS geometric structures across the different cellular layers of the mouse retina and asses calcein diffusivity after iontophoretic release in the retina ECS [7]. Though 2PSI does not provide structural information at the nanometer scale, is sufficient to identify individual cells and observe changes in the gross morphology of different cellular layers and the subsequent diffusivity. Our goal, is to take advantage of the high resolution provided by SUSHI images to further study diffusion in the brain ECS and how changes in the morphology of the brain neuropil will affect cellular signaling around individual cellular sub-structures.

Computational models have been widely used to investigate diffusional phenomena in the brain at different spatio-temporal scales and complement the information obtained experimentally. To understand how models of extracellular diffusion work, we need to consider Fick's first and second laws of diffusion. First Fick's Law states that the diffusion flux is directly proportional to the concentration gradient, and that it goes from high to low concentration regions. For diffusion in one dimension, the diffusion flux is defined as in Equation 1:

Equation 1

$$J = -D \cdot \frac{\partial c}{\partial x}$$

Where J is the diffusion flux, D is the diffusion coefficient, and $\partial c/\partial x$ is the concentration gradient. Fick's second law describes how the concentration changes over time due to diffusion, as represented in Equation 2 for diffusion in one dimension.

Equation 2

$$\frac{\partial C}{\partial t} = D \cdot \frac{\partial^2 c}{\partial^2 x}$$

Where $\partial C/\partial t$ is the change in concentration over time, D is the diffusion coefficient, and $\partial^2 c/\partial^2 x$ is the second derivative of the change in concentration over space. In two or more dimension, Equation 2 can be rewritten using the Laplacian (Δ) as a generalization for the second derivatives (Equation 3).

Equation 3

$$\frac{\partial C}{\partial t} = D \cdot \Delta C$$

Fick's laws of diffusion allow mathematical modelling of diffusion under the assumption that diffusion is free, but, as we have seen, the ECS is structurally complex and diffusion in the brain parenchyma will be restricted by cellular structures, and interactions with other resident molecules of the interstitial fluid, including putative effects of the extracellular matrix. As a result, Fick's second law of diffusion is usually modified to incorporate more spatial dimensions, molecular-uptake, advection, space dependency of D and other variables.

The development of new computational models has been limited by the techniques available to optically resolve the ECS morphology. Thus, most models are based on artificial ECS geometries that recapitulate volume-averaged geometries. Some of the first computational models were developed to study glutamate diffusion and its kinetics in the synaptic cleft or extra-synaptically using the diffusion equation together with a term to incorporate uptake [3], [76]. While these computational models describe very well the biophysical behavior of glutamate, they oversimplified the geometries used to represent the synaptic and extra-synaptic environments, for example describing the synaptic cleft as a 2D flat cylinder [64]. Surprisingly, one of the few models that uses actual microscopy images of the brain ECS is one of the very first attempts to model diffusion in brain tissue by *Lipinski (1990)*, [77]. In this work, light microscopy images of histological preparations of the brain were binarized so that pixels where white or black corresponding to cellular or extracellular space respectively (Figure 16, A-D). Then diffusion in the ECS geometries was simulated using Monte Carlo probabilistic method (Figure 16, G-H). Though this model was quite advanced to its time, it is limited by the imaging resolution that does not allow visualization of ECS structural details.

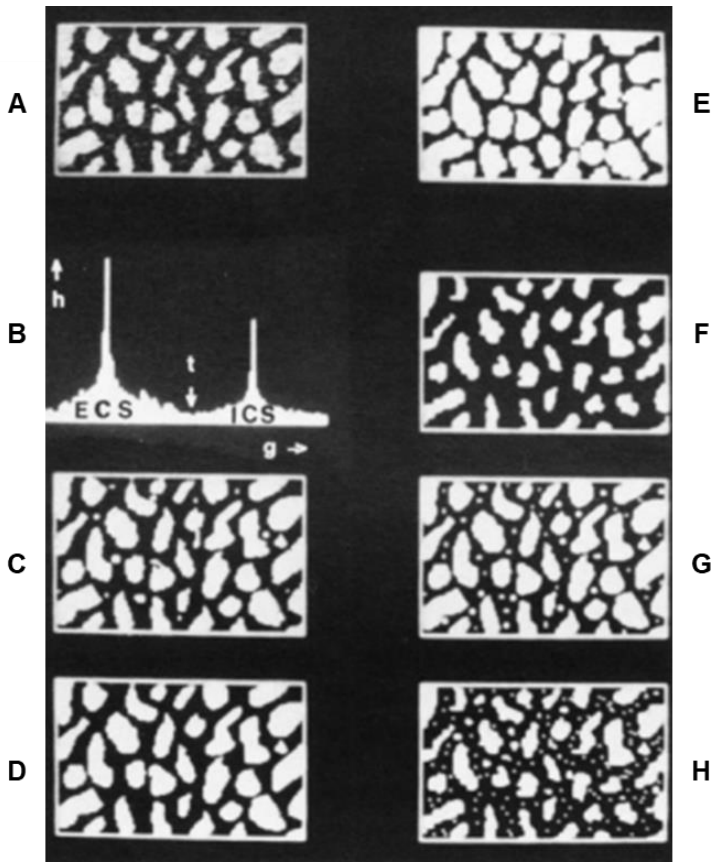

Figure 16 A) Digital image of a hippocampal histological preparation. B) Histogram of the image in A. C) Binary image resulting from the image in A. D) Image C after thresholding to remove noise. E) Image D after dilatation to simulate cellular swelling. F) Image D after erosion to simulate cellular shrinkage. G, H) Monte Carlo simulation of the diffusion of individual particles in the original (image D) and the dilated ECS (image F) respectively. Image from *Lipinski 1990,* [77].

Later models employed hypothetical structures arranged in different lattice patterns to represent cells laying in the ECS. This type of arrangements usually presents a high degree of symmetry and therefore represent a very homogeneous tissue, where ECS channel's width is constant (Figure 17 A). After simulating diffusion in different lattice patterns, researchers have reached to the conclusion that highly uniform lattices are not sufficient to replicate the diffusion observed in live brain tissue. However, introducing dead-spaces or different sized channels (Figure 17 B) will bring diffusion parameters closer to more physiological values [78], [79]. The above-mentioned models show that a representative tissue model, with volume fraction (α) and tortuosity (λ) properties similar to those of the physiological brain ECS, is good enough to simulate the average diffusion observed in the live brain ECS. However, these synthetic models are not based on real ECS geometry, which is highly complex, and will therefore fail to replicate this complexity of the real ECS in the diffusion of molecules. Slightly more complex models, using synthetic 3D ECS structures incorporating vasculature (Figure 17 C), have been used to investigate whether transport in the interstitial fluid occurs mainly by diffusion or if bulk flow also contributes [80].

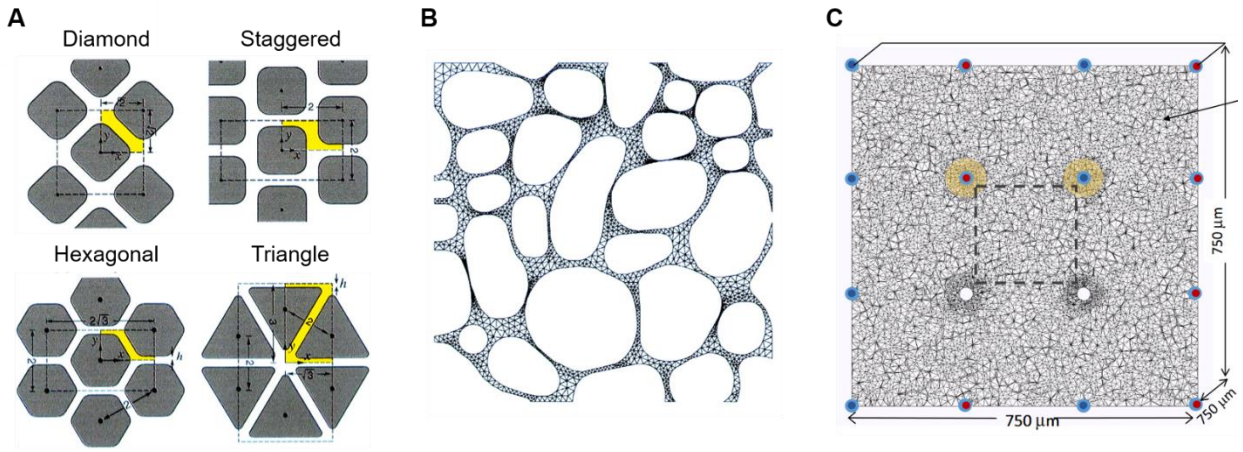

Figure 17 A) Schematic diagrams of different 2D lattice arrangements. Cells are represented by gray-colored obstacles arranged in a lattice structure. B) Hypothetical structure of a more realistic 2D neuropil arrangement. Cells are represented in white and the ECS structure has been triangulated. Images in A and B were modified from *Chen and Nicholson 2000*, [78]. C) Slice from 3D synthetic ECS structure incorporating the vasculature. The tetrahedral mesh represents the interstitial fluid, blue and red dots correspond to venules and arterioles respectively and the surrounding blue annulus is the perivascular space, the yellow annulus represents the perivascular region. Image from *Ray et al. 2019*, [80].

This study suggests that molecular transport in the ECS occurs both by diffusion and bulk flow, however previous work in the field disputed these observations [81]. This previous work used electron microscopy (EM) reconstructions of CA1 hippocampal rat brain slices to mathematically model molecular transport in the CA1 region. The simulations implied that transport of molecules in the CA1 tissue volume were mainly governed by diffusion and not bulk flow [81]. The use of electron microscopy (EM) reconstructions to model ECS morphology has increase not only the complexity of the models, as they capture the high variability of the ECS channels, but also the spatial resolution of the simulations. EM images provide access to the sub-micron structure of the brain neuropil in fixed tissue slice (Figure 18). Consequently, EM reconstructions allow modelling local diffusion of molecules in the sub-micron scale and reveal complex events that cannot yet be easily studied through experimental procedures [82]. The principal disadvantage of these models is that EM uses chemical tissue fixation, which has been reported to shrink the ECS volume a 30 % [20], leading α estimates of 8 % [82], well below *in-vivo* estimates (α = 20 %). To overcome this limitation, α is usually mathematically inflated to more physiological values and a corrected-EM reconstruction is generated, [82], as shown in Figure 18 C. Although, cryo-fixated EM images preserve better the ECS structure, such have not been used yet in computational modelling of diffusion in the brain ECS.

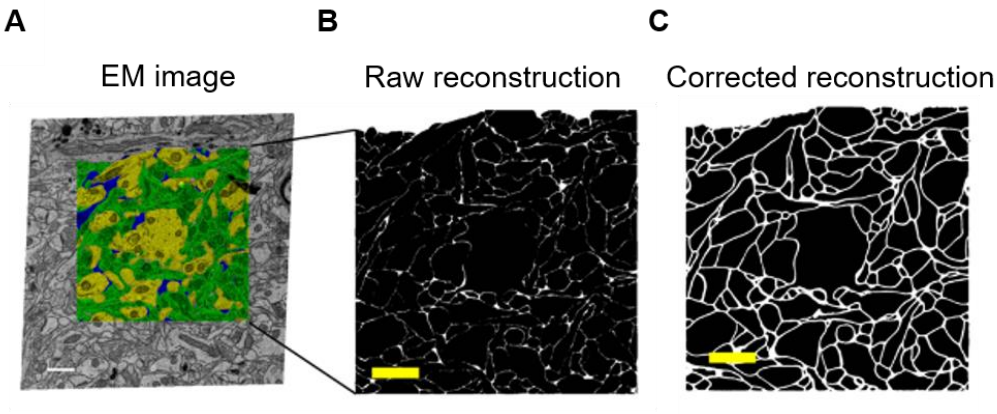

Figure 18 A) Electron microscopy (EM) image. B) Raw reconstructed EM image with ECS rendered in white and cellular structures in black. C) Corrected EM reconstruction with a physiological ECS volume fraction of 0.2. Scalebar in images A-C equals 1 µm. Images modified from *Kinney et al. 2013*, [82].

Some of the recently developed computational models have focused on settings of transmitter release and escape from the synaptic cleft (spillover). The diffusion of transmitters at these small and fast spatio-temporal scales will conceivably be shaped by the sub-micron ECS geometry. Given the complex and heterogeneous morphology of synapses they are not well modelled by lattice patterns. At the same time, they are difficult to resolve with live tissue imaging techniques, and they are distorted by tissue fixation techniques. As a result, these models have developed synthetic synaptic environments, based on randomly sized overlapping spheres, to evaluate the effect of peri-synaptic ECS structure and astrocytic processes around glutamatergic synapses [83], [84].

Fortunately, recently developed super-resolution shadow imaging (SUSHI) provides access to the nano-scale organization of the live brain ECS. However, SUSHI images have never been used to model diffusion of transmitters, experimentally or computationally. Thus, here we aim to build a computational model that takes advantage of the high resolution provided by SUSHI images to more precisely model diffusion in the brain ECS of live tissue at different spatio-temporal scales.

Hypothesis & Objectives

The general goal of the second part of this study it to evaluate how changes in brain ECS morphology in live tissue affect cellular signaling at local scales.

We hypothesize that changes in the nanoscale morphology of the live brain ECS will affect diffusion of molecules at local scales and thereby shape cellular signalling and volume transmission at the submicron level. To study diffusion of transmitters in the live brain ECS at the nanoscale we propose an innovative computational model based on SUSHI images.

- First, we will evaluate our computational model and compare the simulations obtained with published RTI data of TMA^+ diffusion in brain parenchyma and in free medium. In addition, we will also compare or simulations with published simulated data of the diffusion of different sized molecules. In this way, we will verify if the simulations provided by our computational model are in line with the literature.
- Then we will use the model to make predictions about the diffusion of transmitters in the brain ECS. Including: the effect on glutamatergic synaptic crosstalk, and the heterogeneity and directionality of the diffusion at different scales. Thus, we will shed some light in the importance of the brain ECS nanoscale geometry in cellular signalling.

Materials & Methods

Super Resolution Shadow Imaging

Animals

The experimental work for the organotypic cultures was performed in C57BL6J WT pups between postnatal days 5 to 7. Mice were housed at 24 ^{0}C with a 12-h light–dark cycle. They were provided with food and water *ad libitum* and with nesting materials. All procedures were performed according to Spanish law (Real Decreto 53/2013, BOE 08-02-2013) and European Communities Council Directive (2010/63/EU) regulations; and were approved by the Ethics Committees of the University of the Basque Country EHU/UPV (M20/2021/339). All efforts were made to avoid animal suffering and to minimize mice pain and stress.

Organotypic cultures preparation

Organotypic slices were isolated from 5 to 7-day old mouse pups. Mouse pups were quickly decapitated and hippocampi were dissected out in cold dissection medium, which consisted of HBSS (GIBCO) supplemented with 11.5 mM glucose (VWR), 2mM kynurenic acid (Sigma-Aldrich), 20mM HEPES (Sigma-Aldrich), and 1x Pen-Strep (GIBCO). Hippocampi were cut in 350 µm coronal slices using a vibratome (Precisionary Compresstome VF-300), and individual slices were placed on 0.1% poly-L-lysine (Sigma-Aldrich) coated coverslips (12 mm x 24 mm; Menzel-Gläser). Slices were embedded in 10 µL chicken plasma (Sigma-Aldrich) followed by 10 µL of 0.2% thrombin (VWR) in HBSS with 8 mM glucose, and the mix was allowed to coagulate for 30 min in the fridge. The coverslips with the slices were then transferred individually to cell culture tubes (3mL; Nuc) with 750 µL of culturing medium containing 60% MEM-Medium (GIBCO), 25% HBSS, and 10% horse serum (GIBCO), supplemented with 1% glutamine (Invitrogen), 2% B27 (GIBCO), 20mM sucrose (Fisher), 11.5 mM glucose, 10mM HEPES, 0.5 % Pen-Strep and 0.2mM Ascorbic acid (Sigma-Aldrich). The tubes were sealed and placed in a roller drum incubator at 10 rotations per hour at 35 ^{0}C. After 3-4 days in vitro, we added 10 µL of mitosis inhibitor (1mM Uridine, 1mM Ara-c and 1mM 5-Fluoro-2'-deoxyuridine) that was removed after 16-24h by changing 500 µL of medium. For the maintenance of the organotypic cultures 500 µL of medium were changed once a week. Cultures were typically used between 2 and 4 weeks of culturing.

STED microscope

We obtained SUSHI images on our custom build STED microscope, which is a modified version of the microscope design previously published by *Tønnesen* [21]. It is based around a Leica DMi8 body with an inverted 90x 1.3NA glycerol immersion objective with a motorized correction collar (Leica) to compensate aberrations emerging from varying the tissue imaging depth. The depletion laser is a Katana picosecond laser emitting at 592 nm with a repetition rate of 80 MHz. The depletion laser is synchronized as a slave to the 488 nm picosecond excitation laser (Quixx) that has an integrated variable sync pulse delay function to overlap the excitation and depletion pulses in time. The two beams are aligned and scanned across the sample using a Yanus IV galvo-

galvo scan head. Fluorescence from the sample is back-scanned and detected by an avalanche photodiode detector (APD).

To impose the respective donut and bottle beam point-spread functions (PSFs) on the depletion beam, this is split into two arms that are sent through respectively a 2-Pi vortex delay phase mask and a 1-Pi helical delay phase mask (both from Vortex Photonics). The two arms are recombined in a polarizing beam splitter, and the resulting beam aligned with the excitation beam on a dichroic mirror.

The beams and scanner and image-collection were performed using free Imspector Software and saved as 32-bit TIF files. Visualization and analyses were performed in ImageJ.

Extracellular labelling and Imaging

For imaging, organotypic culture slices were transferred on their glass coverslip to a custom imaging chamber. The perfusion medium (artificial cerebrospinal fluid, ACSF) consisted of 126 mM NaCl, 2.5 mM KCl, 2.5 mM $CaCl_2$, 1.3 mM $MgCl_2$, 25 mM HEPES, 10 mM Glucose, 1 mM Trolox, titrated to 300 mOsm and pH 7.4 with 1 M NaOH (all from Sigma-Aldrich).

To label the extracellular space we added 10 to 40 µM calcein disodium salt (Sigma-Aldrich) to the ACSF.

Figure 19 shows a summary of the steps previously explained to acquire SUSHI images.

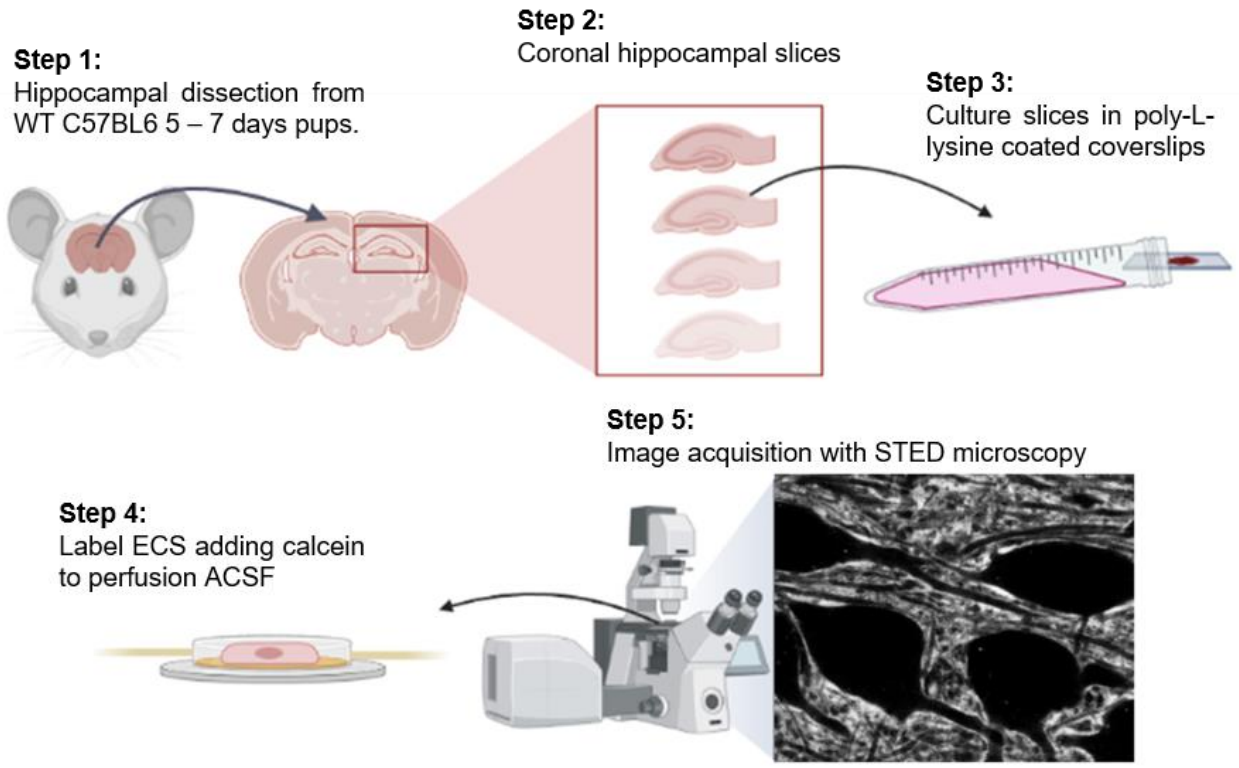

Figure 19. ← Previous page. Graphical summary of the steps for super-resolution shadow imaging. Step 1: The hippocampus is dissected from mouse pups 5-7 postnatal days. Step 2: both hippocampi are cut into coronal slices. Step 3: hippocampal slices are collected and cultured in coverslips in cell culturing tubes. Step 4: 2-4 weeks old organotypic cultures are placed into the imaging chamber and the ECS is labeled with ACSF perfusion supplemented with 10-40 µM calcein. Step 5: the imaging chamber is place back in the custom-built STED microscope, where SUSHI images are acquired.

Image Processing

All simulations were performed on raw images. For graphical presentations in figures, the image contrast was homogenously adjusted across the frame and images were subjected to a 1-pixel median filter to remove detector dark-count outlier pixels.

Computational Model of Diffusion

Model geometry

A computational model was developed to investigate diffusion in the live brain ECS. The model uses SUSHI images to determine the probability of a particle diffusing into a given point based on the pixel values of the image. Figure 20, shows a graphical scheme of the model. When acquiring SUSHI images, the fluorophore is homogeneously distributed in the interstitial fluid. As a result, fluorescence intensity of a single SUSHI image directly scales with the voxel occupancy. Thus, highly occupied voxels by cellular structures will have low pixel value while empty voxels corresponding to pure ECS will have the highest pixel values. In addition, the diffusion flux (J) is defined as the number of particles (M) that move through a unit area (A) per unit time (t), as described in Equation 4. So, in order to estimate the number of particles that move from one voxel to another we directly relate the diffusion coefficient to the pixel intensity. Finally, we solve the diffusion equation for each pixel in the SUSHI image.

Equation 4

$$J = \frac{M}{A \cdot t}$$

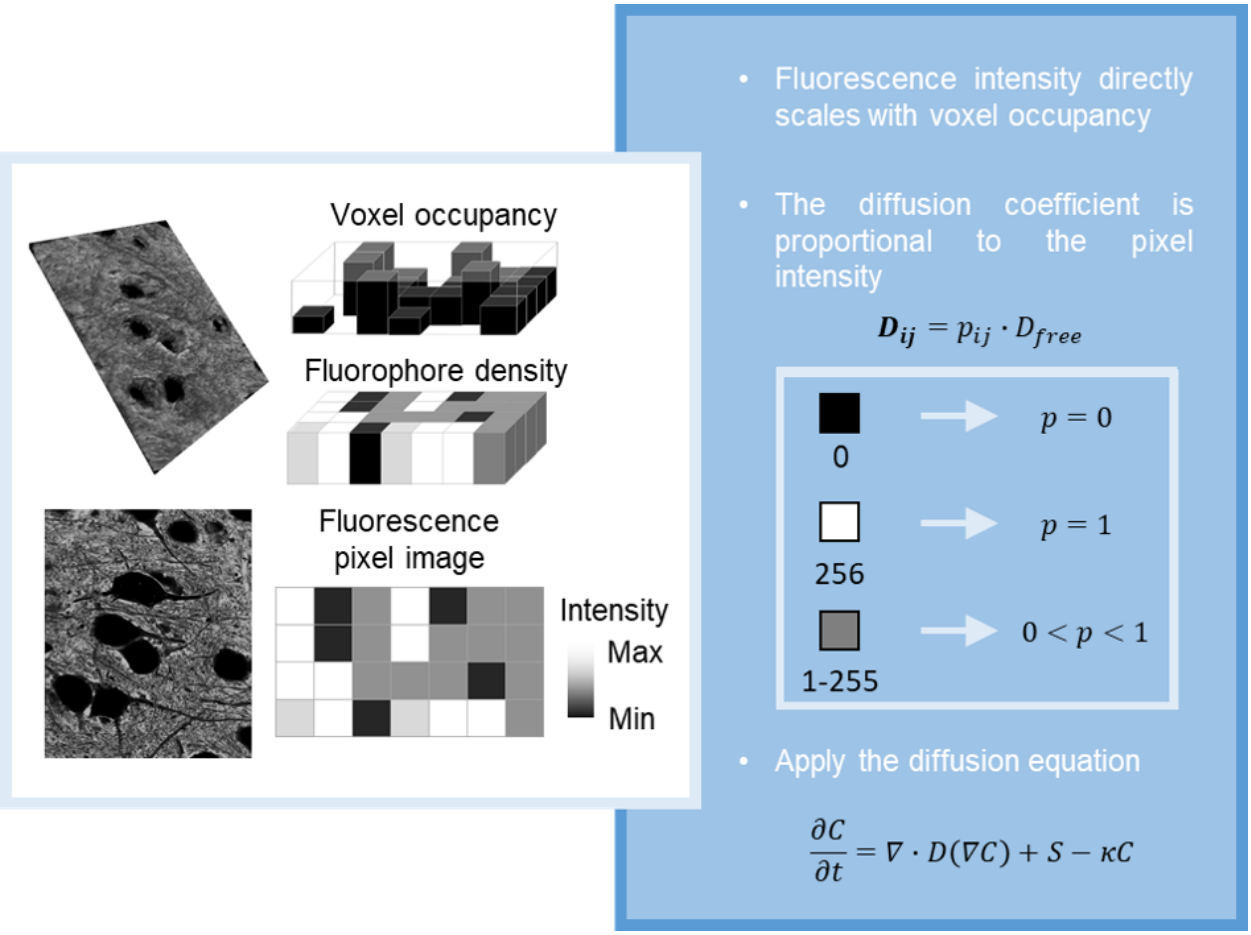

Figure 20 Graphical scheme of our computational model, with detailed explanations in the following text. Super-resolution shadow images borrowed from *Tønnesen et al. (2018),* [21].

Model parameters

The novelty of this model is that the diffusion coefficient (D) depends on the nanoscale geometry (Equation 5). Thus, for a given free diffusion coefficient D_{free}, the diffusion coefficient at each pixel in the image is determined by the diffusion probability (Figure 21 D):

Equation 5

$$D = p \cdot D_{free}$$

We define the diffusion probability (p) for each pixel as in Equation 6, (Figure 21 C):

Equation 6

$$p = \frac{Pixel\ value}{Max\ Pixel\ value}$$

The model was implemented for several images at different temporal and spatial scales. The time step ($\Delta \boldsymbol{t}$), the total simulation time (T), and the pixel size ($\Delta x, \Delta y$) are specified for each simulation example.

In addition, for each simulation we estimated the tortuosity and the volume fraction of the SUSHI image. The tortuosity (λ) in our model is defined as:

Equation 7

$$\lambda = \sqrt{D_{free}/D_{av}}$$

Where D_{av} is the average diffusion coefficient of the used SUSHI image. Once we estimated D scaled by the cell-structural obstacles in each pixel in the image, we calculated the mean diffusion coefficient of the whole SUSHI image used.

In this model the volume fraction (α) was described for each SUSHI image as the number of pixels corresponding to ECS over the total number of pixels in the image (Figure 21 B). The number of pixels corresponding to ECS was estimated as the number of pixels above a given threshold defined in Equation 8.

Equation 8

$$threshold = \frac{maximum\ pixel\ value - minimum\ pixel\ value}{2}$$

Mathematical model

Modelling diffusion around individual cellular sub-structures in the brain ECS was implemented using MATLAB software (Matlab R2019b). We used the adapted advection-diffusion equation (Equation 9) for mass transport in porous brain tissue, based on *Nicholson and Phillips* [85], [86]:

Equation 9

$$\frac{\partial C}{\partial t} = \nabla \cdot D(\nabla C) - \nabla \cdot (vC) + S - \kappa C$$

Where, C is the solute's concentration, D is the scaled diffusion coefficient, v is the velocity field, S is the source strength and κ is the clearance coefficient that accounts for non-specific clearance, such as cellular uptake of the diffusing molecule, as previously described [14]. Given that we are modelling transport of small molecules with relatively fast diffusivity, interstitial transport is presumably predominantly by diffusion [80]. Therefore, we assumed $(\mathrm{v} = 0)$ and disregarded the advection term $(\nabla \cdot (\mathrm{vC}))$ in the advection-diffusion equation. In our model the source (S) magnitude can be defined in two ways. Either as a sustained iontophoretic source

according to *Hrabětová and Nicholson* [87] (Equation 10); or it can be defined as an instant number of particles released per unit volume (Equation 11).

Equation 10 Iontophoretic source magnitude (S).

$$S = \frac{I \cdot n_t}{z \cdot F}$$

Where I is the magnitude of the iontophoretic current, n_t is the transport number of the iontophoretic electrode, z is the valency of the ion, and F is Faraday's constant (F = 96485.33 C/mol).

Equation 11 Number of particles source magnitude (S)

$$S = \frac{n \cdot N_A}{\Delta x \cdot \Delta y \cdot \Delta z}$$

Where n is the number of particles, N_A is the Avogadro's number ($N_A = 6.022 \cdot 10^{23}$) and $\Delta x, \Delta y, \Delta z$ are the pixel sizes in the x, y, z dimensions respectively.

We approximated the solution of the diffusion equation both in 2D (x, y) and in 3D (x, y, z) using the Forward in Time Central in Space (FTCS) finite difference method [88]. This approximation was then solved iteratively over time for each pixel in the SUSHI image (Equation 12 and

Equation *13*). Forward Euler Method was used to approximate the time derivative in the diffusion equation as follows:

Equation 12 Forward Euler finite difference approximation of the diffusion equation.

$$C_{t+\Delta t}^{x,y,z} = D^{x,y,z} \cdot \left(\frac{\partial^2 C}{\partial x^2} + \frac{\partial^2 C}{\partial y^2} + \frac{\partial^2 C}{\partial z^2}\right) \cdot \Delta t + S' - \kappa' C_t^{x,y,z} + C_t^{x,y,z}$$

Where $\kappa' = \kappa \cdot \Delta t$ *and* $S' = S_{(x,y,z)} \cdot \Delta t$.

The Central Difference Method was used to approximate the space derivatives so that:

Equation 13 Central difference approximation or the space derivatives.

$$\frac{\partial^2 C}{\partial x^2} \approx \frac{C_t^{x+\Delta x,y,z} + C_t^{x-\Delta x,y,z} - 2C_t^{x,y,z}}{\Delta x^2}$$

$$\frac{\partial^2 C}{\partial y^2} \approx \frac{C_t^{x,y+\Delta y,z} + C_t^{x,y-\Delta y,z} - 2C_t^{x,y,z}}{\Delta y^2}$$

$$\frac{\partial^2 C}{\partial z^2} \approx \frac{C_t^{x,y,z+\Delta z} + C_t^{x,y,z-\Delta z} - 2C_t^{x,y,z}}{\Delta z^2}$$

In order to reduce the computational cost of the simulations, we adapted the 3D model into a pseudo-3D model. The pseudo-3D model solves the diffusion equation in 2D but uses the clearance coefficient (κ) to account for diffusion in the z dimension to approximate 3D diffusion simulations. The value of κ was scaled by the diffusion probability (p) for each pixel in the 2D SUSHI image. Since Equation 9 was solved for each pixel, the corresponding scaled κ to that pixel was used (Figure 21 E). Thus, pixels with low pixel intensity (low diffusion probability) will present low escape in the z dimension (low κ).

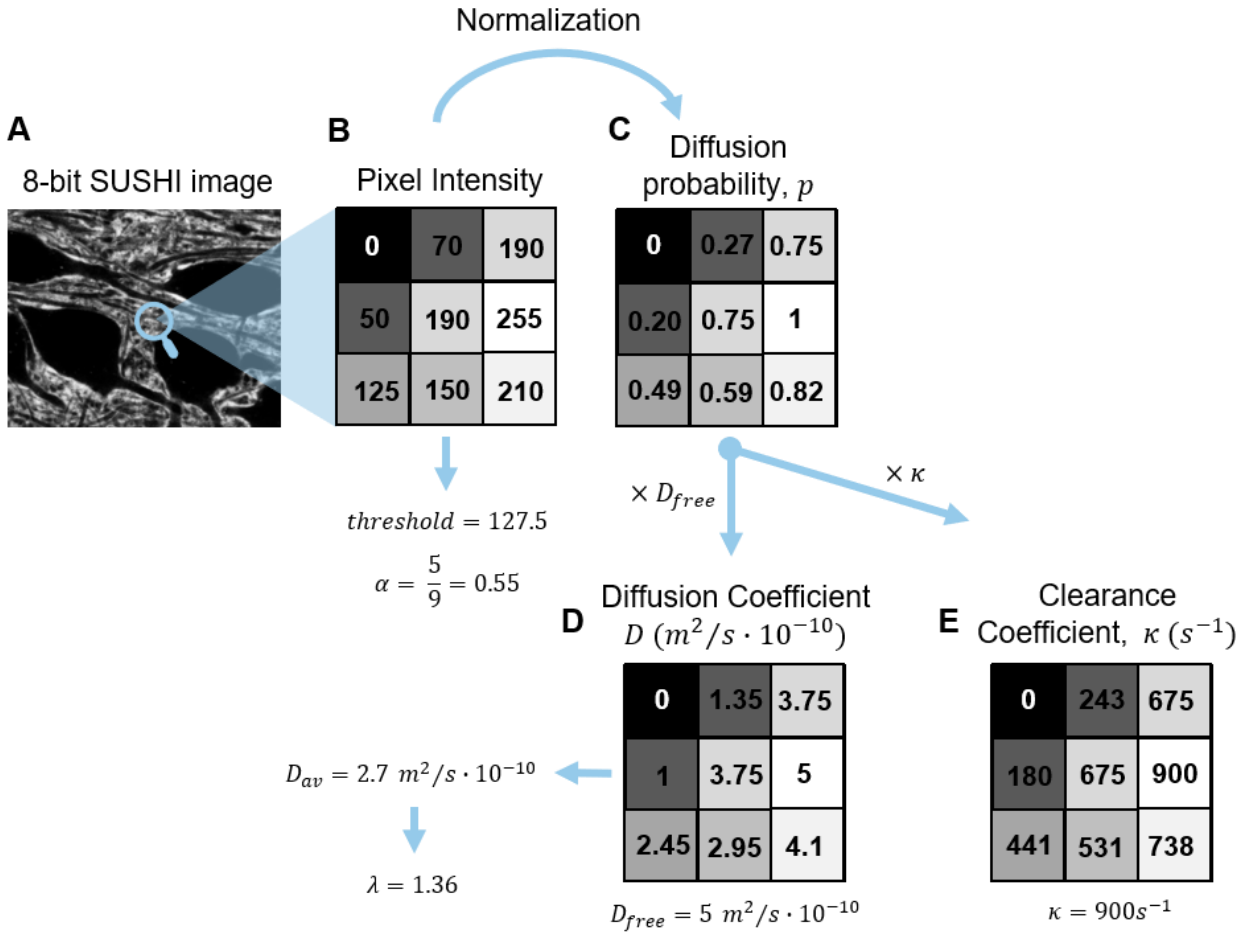

Figure 21 Schematic representation of how the different model parameters are calculated. A) Representative 8-bit SUSHI image. B) Section of the SUSHI image of 3x3 pixels. Pixel intensities are displayed for each pixel. From the pixel intensity α can be estimated as the number of pixels above the threshold over the total number of pixels. C) Diffusion

probability (p) array of 3x3 pixels, obtained after normalizing the pixel intensity. D) Diffusion coefficient (D) array of 3x3 pixels, obtained after multiplying the diffusion probability array by the free diffusion coefficient. From D, the average diffusion coefficient (D_{av}) and λ can be calculated. E) Clearance coefficient array of 3x3 pixels was calculated by multiplying the diffusion probability array by the clearance coefficient (κ).

Boundary conditions

In our model, we assumed an infinitely large space, so molecules can diffuse and escape at the edge of the image frame. We presumed that at the edge 90% of the arriving concentration escapes (Equation 14). This value was chosen by comparing our simulated data with the RTI measurements from *Hrabětová 2007* [87]. After running simulations with different escape coefficients, the value that resulted in a smoother diffusion at the edges and better matched the RTI curves was selected.

The concentration at the edge of the image is described by:

Equation 14

$$C_t^{1,y,z} = sc \cdot C_{t-\Delta t}^{2,y,z}$$

Where 1 and 2 denote pixel indexes, and sc is the scape coefficient ($sc = 0.9$). Equation 14 was solved for all the edges of the image in the x, y and z directions.

In addition, the model considers diffusion around cellular structures and prevents accumulation of molecules in their boundaries. The concentration at the boundary of a cellular structure is described by Equation 15 and it applies for the three dimensions x, y, z.

Equation 15

$$\frac{\partial^2 C}{\partial x^2} \approx \frac{C_t^{x+\Delta x,y,z} - C_t^{x,y,z}}{\Delta x^2} \qquad if D^{x-\Delta x,y,z} = 0$$

$$\frac{\partial^2 C}{\partial x^2} \approx \frac{C_t^{x-\Delta x,y,z} - C_t^{x,y,z}}{\Delta x^2} \qquad if D^{x+\Delta x,y,z} = 0$$

$$\frac{\partial^2 C}{\partial x^2} \approx 0 \qquad \text{if } D^{x+\Delta x,y,z} = 0 \text{ and } D^{x-\Delta x,y,z} = 0$$

Matlab code and post-simulation analysis

The computational model was programmed in Matlab R2019b. We developed a user interface (UI) to adjust all the parameters of each simulation in a user-friendly way (Figure 22). The UI allows the user to select the desired image from the user's folder and tune all the image parameters, such as pixel size, image dimensions, location of source point, etc. When the load

button is pressed the Matlab code runs a custom-built function (*LoadImage.m*), which loads the selected image into Matlab workspace, displays it in the UI, and calculates α for that image. Then the UI allows the user to introduce the simulation parameters (i.e. diffusion coefficient, time step, source duration) the source type and the saving options. Once the start button is pressed the simulation begins and Matlab code works as follows:

1. The custom-built function *LoadParam.m* reads all the input parameters that the UI has previously introduced and converts all the units to SI units (international system units).
2. The custom-built function *SolveEquations.m* solves the finite difference approximations of the diffusion equation (Equation 12 and
3. Equation *13*), either in 2D/pseudo-3D or in 3D using custom-built functions *NumericalSolver2D.m* and *NumericalSolver3D.m* respectively. These functions in turn use the Matlab *for* loop to solve the approximations iteratively in time.

Once the simulation finishes, the user can save a video of the concentration dispersion over time by pressing the green *play* button. At the same time a set of time-lapsed images of the concentration dispersion is displayed (custom-built function *SaveVideo.m*).

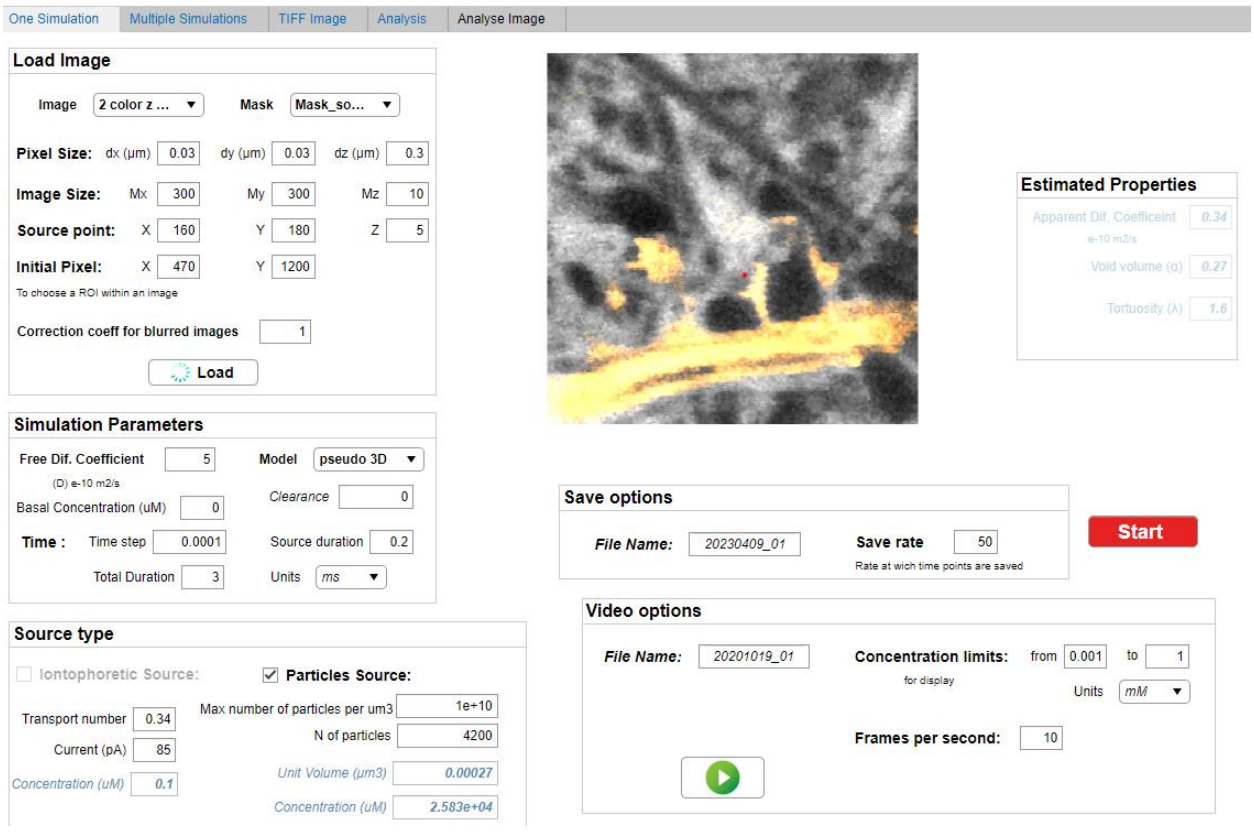

Figure 22 Matlab user interface (UI) of our SUSHI-based computational model. The UI allows the user to select the image from the user's folder and tune all the image parameters. The chosen image and source point are display in the UI. The simulation parameters (D_{free}, type of simulation, time step and duration of the simulation) are also defined by the user, as well as the source type. The user can choose the name of the file and start the simulation.

Once the simulation is finished a video and a set of time-lapsed images can be displayed. The estimated properties box displays the calculated α, λ and D_{av} for each SUSHI image.

The UI also allows to run several subsequent simulations at different source locations using the *Multiple simulations* window (Figure 23). To do so, the *SolveEquations.m* functions iterates the numerical solver (*NumericalSolver2D.m*) for each of the points in the source location file using again the Matlab *for* loop.

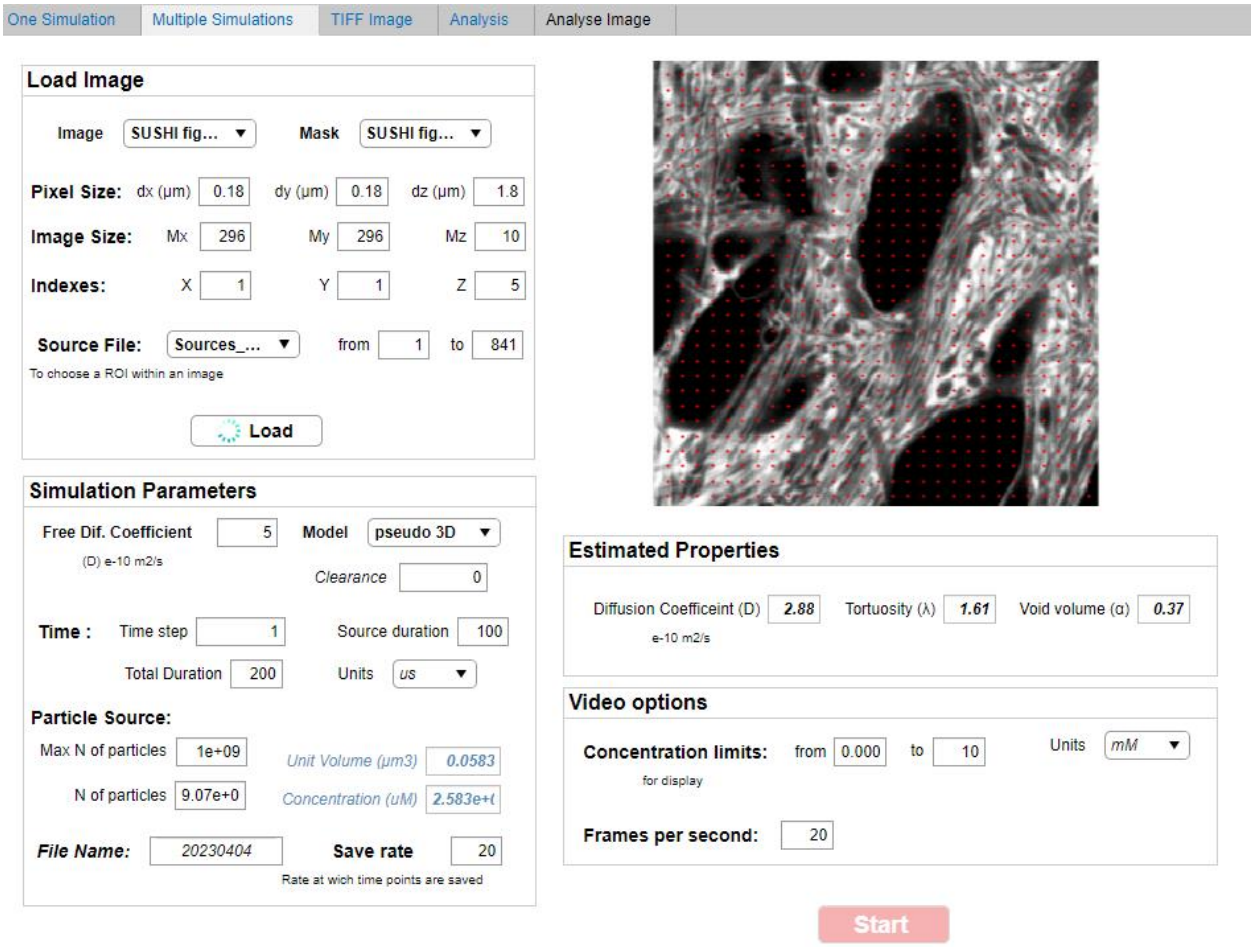

Figure 23 Matlab user interface (UI) of our SUSHI-based computational model. The UI allows the user to perform several subsequent simulations at different source locations. The chosen image and source point file are displayed in the UI. The rest of the interface works as for a single simulation.

The user interface further allows us performing all the presented post-simulation analyses. The analysis window (Figure 24) displays a menu with the different post-simulation analysis that the program can perform.

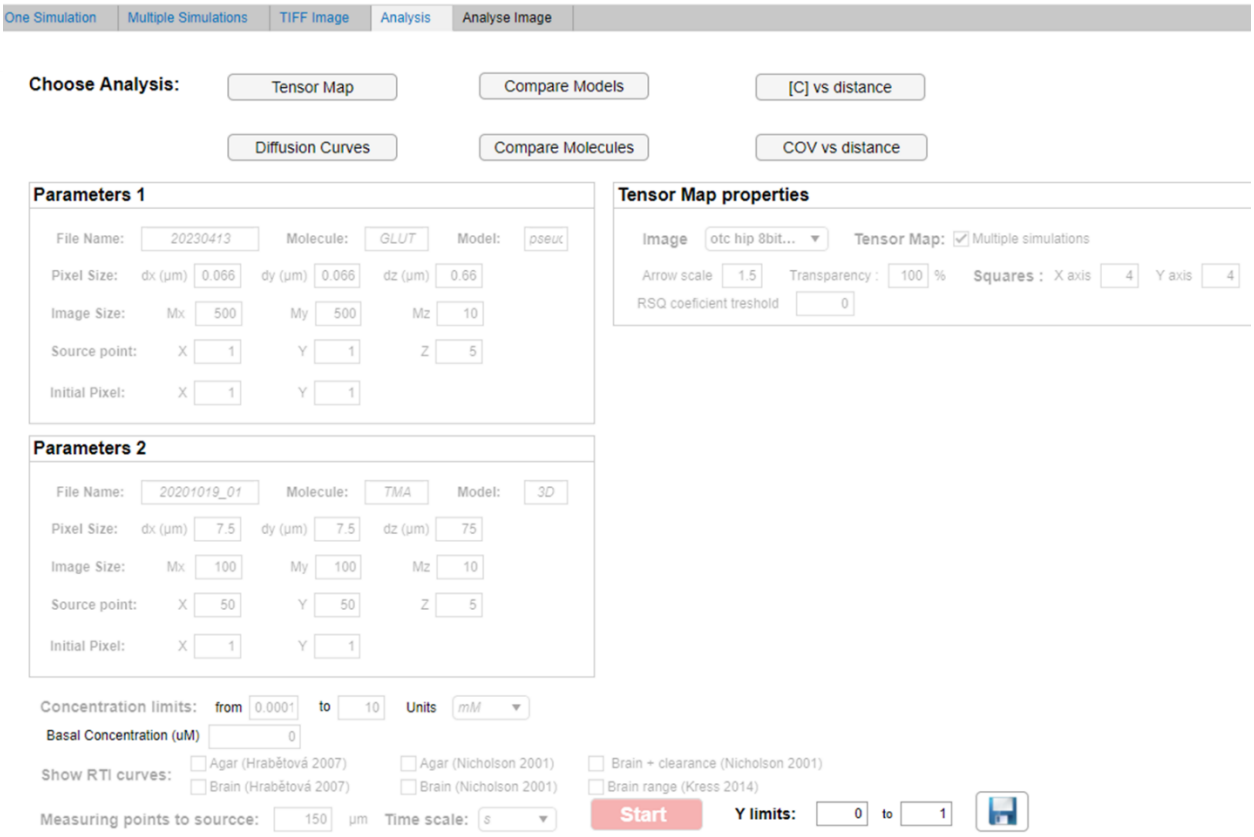

Figure 24 Matlab user interface (UI) of our SUSHI-based computational model, analysis window. Different post-simulation analyses can be performed, such as display tensor-maps, measure diffusion curves, calculate the index of dispersion over distance (COV vs distance), etc.

These include:

- Tensor Map analysis. After running multiple simulations, we can analyze the preferred direction for diffusion at each source location and represent it with a tensor. Tensor maps are obtained using the custom-built *tensormap.m* function.

  For each simulation of diffusional spread we identified the most prominent direction of the diffusion pattern at the end of the simulation. To do so, we calculated the distance of each pixel in the diffusion cloud to the source point and identified the farthest pixel (red point, top Figure 25). Then a linear fit was performed to the diffusion pattern and the Pearson's correlation coefficient (r) was measured for each simulation, which reported the goodness of the fit to the simulated data. Pearson's coefficient gives a value between -1 and 1, where 1 (or -1) means a good fit and 0 indicates that the linear fit does not represent well the data sample. For the purpose of our analysis we always used the absolute value of r. As shown in Figure 25 A and B if the diffusion cloud presents some directionality, r will be greater than zero. The more directional the dispersion the greater the value of r. On the contrary, if the diffusion is very homogeneous, the goodness of the fit (r) will be close to zero (Figure 25 C). Given that in general our simulations poorly fit a

line, we normalized Pearson's correlation coefficient with respect the highest r of the whole tensor map. Then, we assigned a vector from the source point towards the farthest point with a corresponding direction (angle) and magnitude. To account for the goodness of the fit, and therefore the strength of the directionality, we scaled the magnitude of the vector by the normalized Pearson's coefficient. In this way if the diffusion pattern is very homogeneous, the magnitude of the tensor would be almost zero (bottom Figure 25 C).

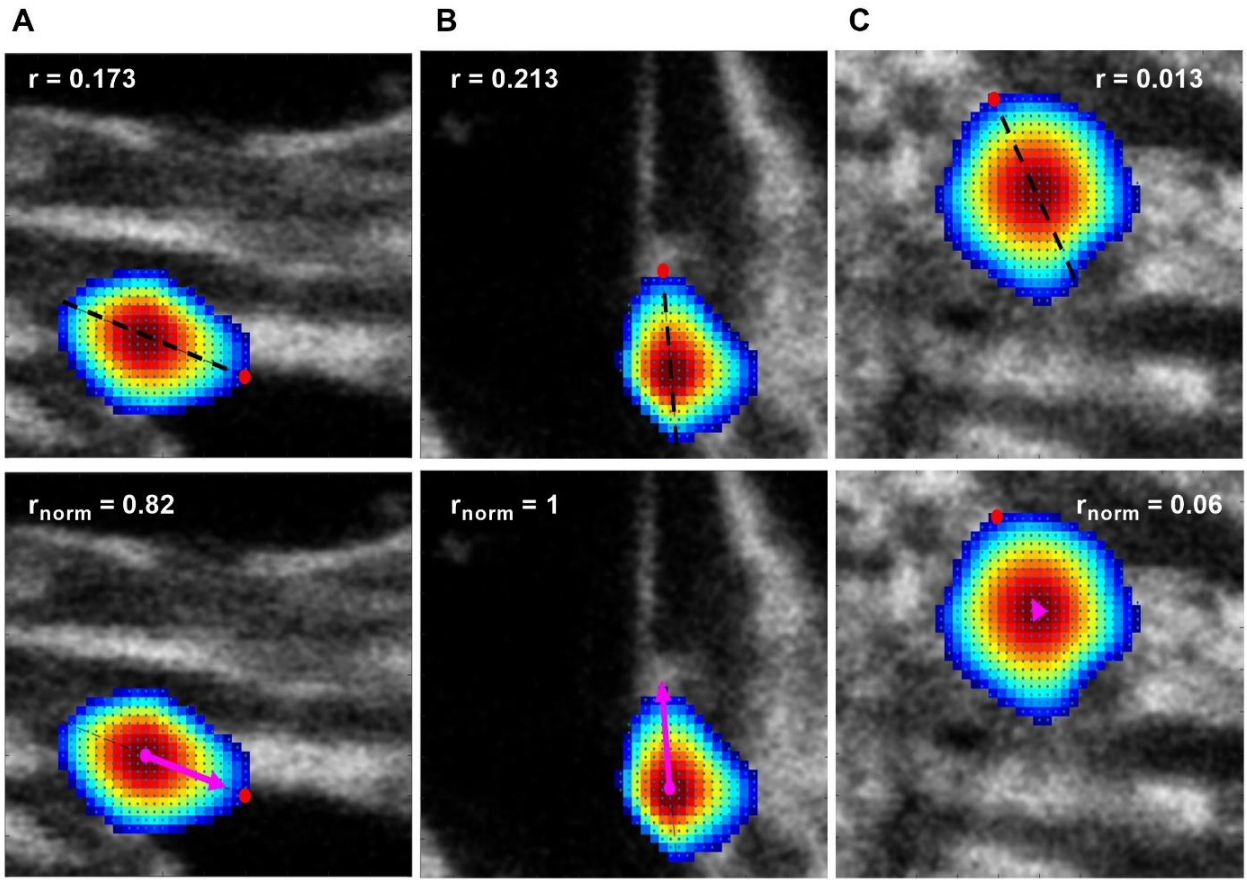

Figure 25 Preferred direction calculation. Individual SUSHI-based simulations of single vesicle glutamate release in the brain ECS are represented in each image. The three simulations in A, B and C were performed at different locations in the same SUSHI image. The red point represents the farthest point of the diffusion pattern from the source location. The black discontinuous line represents the linear fit of the concentration pattern. The Pearson correlation coefficient (r) is display for each image (A, B, C top images). The pink arrow corresponds to the tensor indicating direction and magnitude of the spread. The magnitude of the tensor is scaled by the normalized Pearson correlation coefficient (r_{norm}), (A, B, C bottom images).

- Diffusion curves. This analysis provides the concentration profile over time measured for 16 different points located at a distance from the source specified by the user.
- Compare Models. This analysis overlaps the diffusion curves of simulations from different models (i.e. pseudo-3D vs 3D).

- Compare Molecules. This analysis overlaps the diffusion curves of simulations using different molecules (i.e. different diffusion coefficients).
- [C] vs distance. Displays how the concentration profiles changes with distance at a selected time point.
- COV vs distance. This analysis calculates the index of dispersion of the concentration profile at different distances.

Results

Simulations vs published data

Many computational models use real time iontophoresis to experimentally validate their simulations. As a first step to verify that our computational model is working properly, we compared RTI measurements of TMA^+ both in agar and in brain parenchyma from *Hrabětová 2007* [87] against our simulated data. To do so, we simulated released of TMA^+ by an iontophoretic source with a current pulse of 100 nA during 50s and the subsequent diffusion in 3D during 120 s in free diffusion medium and in live brain ECS, to replicate the same experimental conditions as used experimentally by *Hrabětová.* To simulate free diffusion, a white image with tortuosity (λ) and ECS volume fraction (α) equal to 1 was used, as experimentally observed in the literature in agar experiments. Diffusion in live brain ECS was simulated using a SUSHI image with values for λ and α similar to those reported by *Hrabětová,* (SUSHI image: λ=1.6, α=0.22, RTI: λ=1.6, α=0.23). In addition, *Hrabětová* reported a measured diffusion coefficient of 1.25 10^{-9} m^2/s and a clearance of 0.0095 s^{-1}, so we used those same values as diffusion coefficient (D) and clearance coefficient (κ) in Equation 9. Both images, free diffusion and SUSHI image-based diffusion, were 100x100x10 pixels with an imposed field of view size of 750x750x750 µm. As a result, Figure 26 A shows the simulated concentration patterns of TMA^+ at different time points in the middle z-plane in agar (top) and in live brain ECS (bottom). Then, we measure the concertation over time at 16 different concentric points at distance of 120 µm from the source, as in *Hrabětová*. As shown in Figure 26 B, our simulated data, represented as mean (red line) + standard deviation (SD, shadow), closely matched the RTI curves from *Hrabětová*, though with a slightly slower recovery at the end of the iontophoretic pulse.

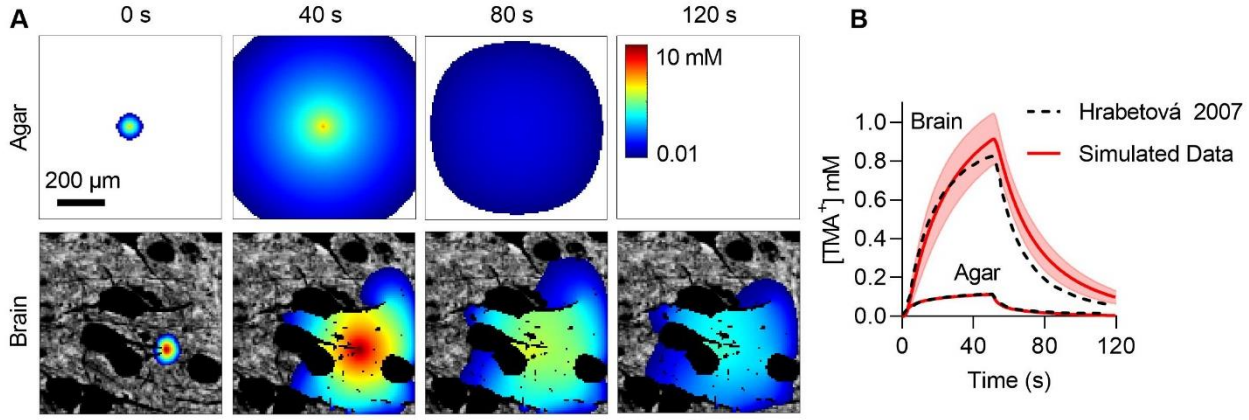

Figure 26 Simulations vs literature RTI measurements from *Hrabetová 2007* [87]. A) Representative simulations of TMA^+ released by an iontophoretic source (100 nA during 50s) and its spread during 120 s both in agar (top) and in brain (bottom). Scalebar 200 µm and color bar from 0.01 to 10 mM. B) TMA^+ concentration profile over time both in brain and agar measured at 120 µm from the source. The iontophoretic pulse lasted 50 s. The TMA^+ simulated data is represented as mean (red line) + SD (shadow) against the RTI curves from *Hrabětová 2007* [87].

In addition, we compared our simulations with published simulations of iontophoretic release and diffusion of different sized molecules: TMA^+, dextran 3.000 Daltons (Dex3k), bovine serum albumin (BSA) and dextran 70.000 Daltons (Dex70k) with reported diffusion coefficients of 1.2, 0.23, 0.083, 0.038 10^{-9} m^2/s respectively (*Nicholson 2001* [85]). We simulated released of those different molecules at a rate of 4 10^{-6} mol/s during 50 s and their diffusion in 3D during 400 s in agar, live brain ECS, and in live brain ECS considering uptake of molecules by cells, to replicate the same conditions as in the simulations reported by *Nicholson*. To simulate diffusion in agar and in live brain we used the same images as in Figure 26 A (estimated λ=1, α=1 and λ=1.6, α=0.22, respectively). *Nicholson* reported α=0.2 and an average λ=1.6 for TMA^+ and λ=2 for bigger molecules in live brain parenchyma. To simulate diffusion in live brain with uptake of molecules we used a clearance coefficient, κ = 0.005 s^{-1}, as the one used by *Nicholson.*

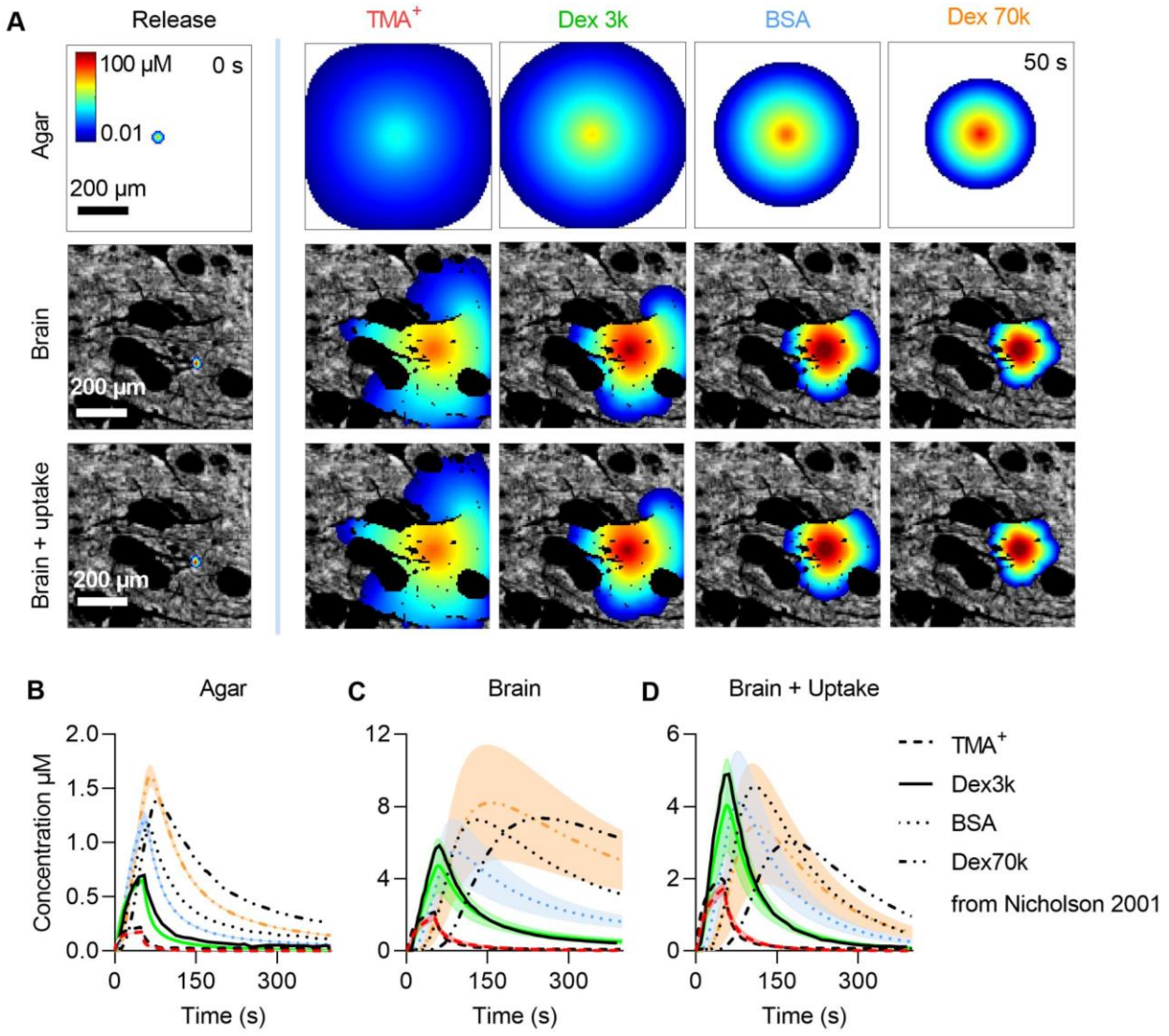

Figure 27. Original simulations vs published simulated data from *Nicholson 2001* [85]. A) Original simulated release (left) and diffusion (right) of TMA^+(red), Dex 3k (green), BSA (blue), Dex 70k (orange) after 50 s. Diffusion was

simulated in agar (top), brain ECS (middle) and in brain ECS considering also uptake of molecules (bottom). Scalebar 200 µm and color bar from 0.1 to 10 µM. B, C, D) Concentration profiles over time measured at 100 µm from the source in agar, brain and brain + uptake respectively. The original simulated data for TMA^+(red), Dex 3k (green), BSA (blue), Dex 70k (orange) is represented as mean (line) and SD (shadowed) against the published simulated data (black) from *Nicholson 2001* [85].

Figure 27 A shows the simulated concentration patterns of the different sized molecules (TMA^+, Dex3k, BSA and Dex70k) at the time of release (0 s) and after 50 s in agar (top), live brain ECS (middle) and live brain ECS with uptake (bottom). To compare our simulations with the published data, we measured the concentration over time at 16 different concentric points at 100 µm from the source, as reported in *Nicholson 2001.* While the simulated data matched the published simulations in all the scenarios for small molecules (TMA^+ and Dex3k), our simulations failed to describe the concertation profiles observed for bigger molecules, as show in Figure 27 B-D. In fact, our model showed a faster diffusion profile for bigger molecules such us BSA and Dex70k.

3D vs Pseudo 3D model

We built a computational model of diffusion that works both in 2D and 3D. In order to improve the applicability to biological scenarios of the simulations, we developed a pseudo-3D model that solves the diffusion equation (Equation 9) in 2D but considers escape of molecules in the z-axis through the clearance coefficient (κ). To test our pseudo-3D model, we simulated glutamate spread over a period of 2 ms after modelled single vesicular release in the live brain ECS using both the 3D and pseudo-3D model. Recent estimates of the number of glutamate molecules per synaptic vesicle are around 7000-8000 molecules [89], [90] and previous models have used 120nm wide 20 nm tall disk as an approximation for the synaptic cleft volume [83]. Thus, we have calculated a point release of 4200 molecules in $2.7 \cdot 10^{-4}$ μm^3 during 0.2 ms for the simulations that required single vesicular release of glutamate. For both simulations a SUSHI image of a labeled dendritic segment and the surrounding ECS was used (estimated λ=1.78, α=0.27). For 3D simulations we used a SUSHI z-stack of 300x300x10 pixels with a field of view size of 9x9x3 µm, pseudo-3D simulations used just one frame of the 3D z-stack (the middle plane). Figure 28 A displays the resulting glutamate spread over time in live brain tissue using the 3D model (top) and the pseudo 3D model (bottom, $\kappa = 900\ s^{-1}$). Again, to compare both models, we measure the concentration over time at 15 different concentric points (dotted circle in Figure 28 A) at a distance of 1 µm from the source. Figure 28 B and C show the individual concentration profiles for each of the 15 points. The difference between each of the individual profiles was estimated as shown in Figure 28 D. As a result, the pseudo-3D model faithfully describes the 3D concentration profile but with much less computational cost, as it is shown by the compared concentration profiles and their difference in Figure 28 E and F respectively (represented as mean + SD).

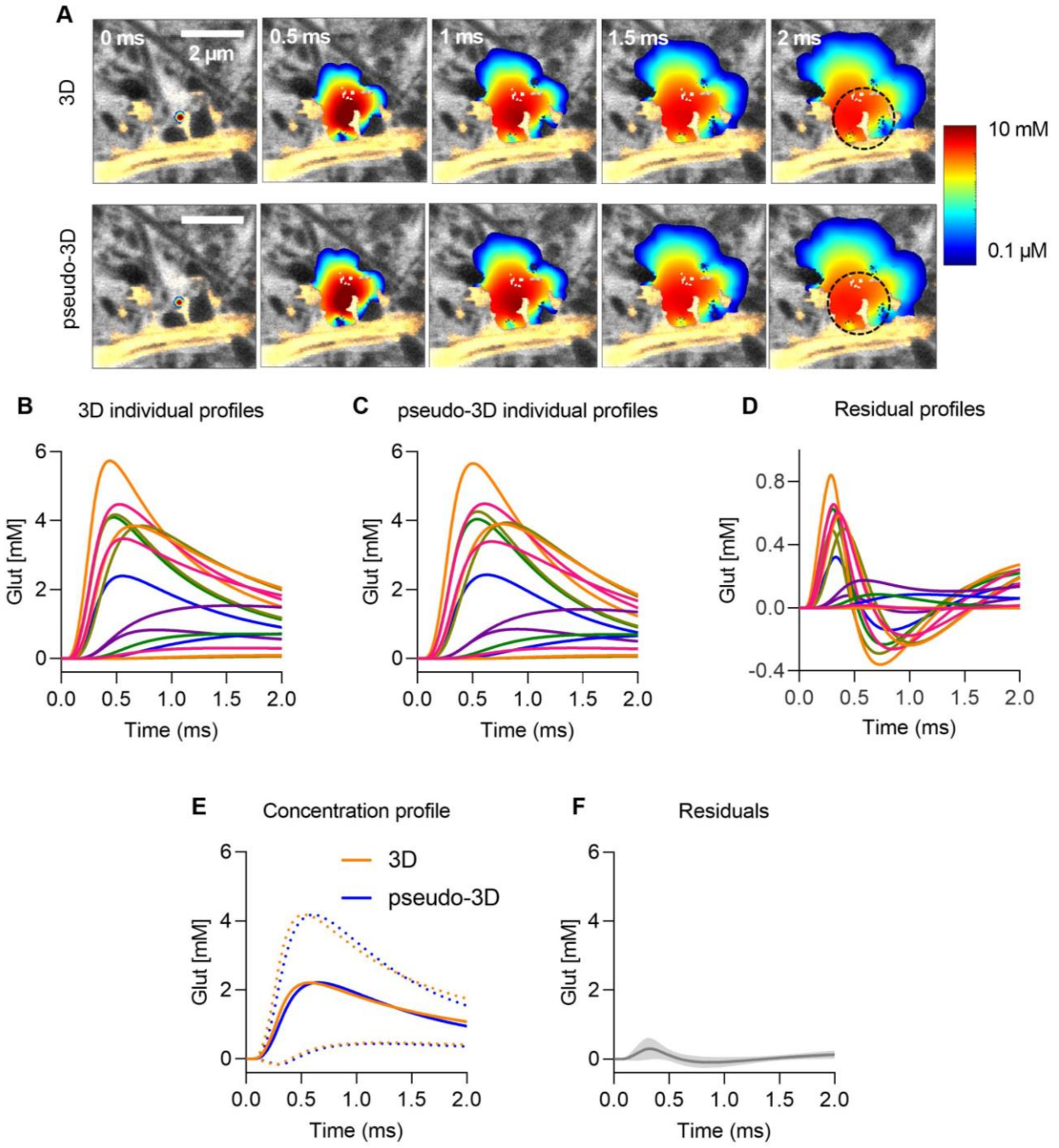

Figure 28. 3D vs pseudo-3D model. A) 3D (upper) and pseudo-3D (bottom) simulations of glutamate spread over 2 ms after single vesicular release of glutamate. Scalebar 2 µm and color bar from 0.1 µM to 10 mM. The dotted circle represents the distance at which the concentration profiles where measured. B, C) Individual concentration profiles measured at 15 points at 1 µm from the source, for the 3D and pseudo-3D simulations respectively. D) Residual individual profiles corresponding to the difference between the 3D and pseudo-3D individual profiles. Note that the range in y-axis is different. E) 3D and pseudo-3D concentration profiles represented as mean (line) and standard deviation (SD, dotted line). F) Residual profile corresponding to the difference between 3D and pseudo-3D individual profiles represented as the mean (gray line) and SD (shadow).

Predictions about ECS diffusion

Osmotic challenge effect on extracellular concentration

First, we investigated how expansion of the live brain ECS, caused by hyperosmotic conditions, affects the diffusion of glutamate at different source locations. GABAergic synapses are commonly formed on dendritic trunks or somatas, and in these areas, we see in the SUSHI images that there are usually larger extracellular spaces; at least in organotypic slices. Thus, after a hyperosmotic challenge we expect to have a higher dilution effect in the concentration of transmitters close to somatic areas, and therefore conceivably higher impact on the GABAergic tonic inhibition. To test our hypothesis, we used previously published SUSHI images obtained before and after increasing the osmolarity a 27 % (from 300 mOsm to 380 mOsm) from *Tønnesen et al. (2018),* [21]. We used the NormoOsmolar (with estimated λ=1.67, α=0.32) and HyperOsmolar (with estimated λ=1.46, α=0.49) SUSHI images to run simulations of single vesicular release of glutamate at different locations in them. Both images were 450 x 450 pixels with a field of view of 54 x 54 µm. The spread of glutamate was simulated over 3 ms for all the source locations (Figure 29 A-C). In order to evaluate the effect of the brain ECS expansion on the diffusion of glutamate, we measured the concentration profiles at 16 different points at 2µm from the source point for the NormoOsmolar and HyperOsmolar SUSHI images (Figure 29 D, represented as mean + SD). This figure shows that, at 2 µm from the source, ECS expansion facilitates the diffusion of transmitters so the concentration raises faster than in NormoOsmolar conditions. However, after a few milliseconds, the concentration starts to be higher at 2 µm from the source in the NormoOsmolar condition as its spread is more constrained (Figure 29 E). Together, Figure 29 D and E show that, close to somatic areas where we can find large ECS volumes (Sources A and B), glutamate diffusion is enhanced and the concentration of transmitters at 2 µm from the source is increased for a while in Hyperosmotic conditions. However, in regions where the ECS is more constrained (Source C), hyperosmotic conditions briefly enhance the diffusion of neurotransmitters in the brain neuropil, but actually the dilution effect is stronger (Figure 29 D and E, Source C). Closer to the source, at 0.5 µm, very fast the concentration of the neurotransmitter is diluted in hyperosmotic conditions by a factor between 1.5 and 2 for the three source locations (Figure 29 F and G). At 0.5 µm from the source, the dilution effect is still slightly stronger in regions where the extracellular compartment is more constrained (Source C).

Altogether, these results suggest that the dilution effect of ECS expansion during hyperosmotic challenge will be greater in regions where the ECS is more constrained by cellular or ECM structures.

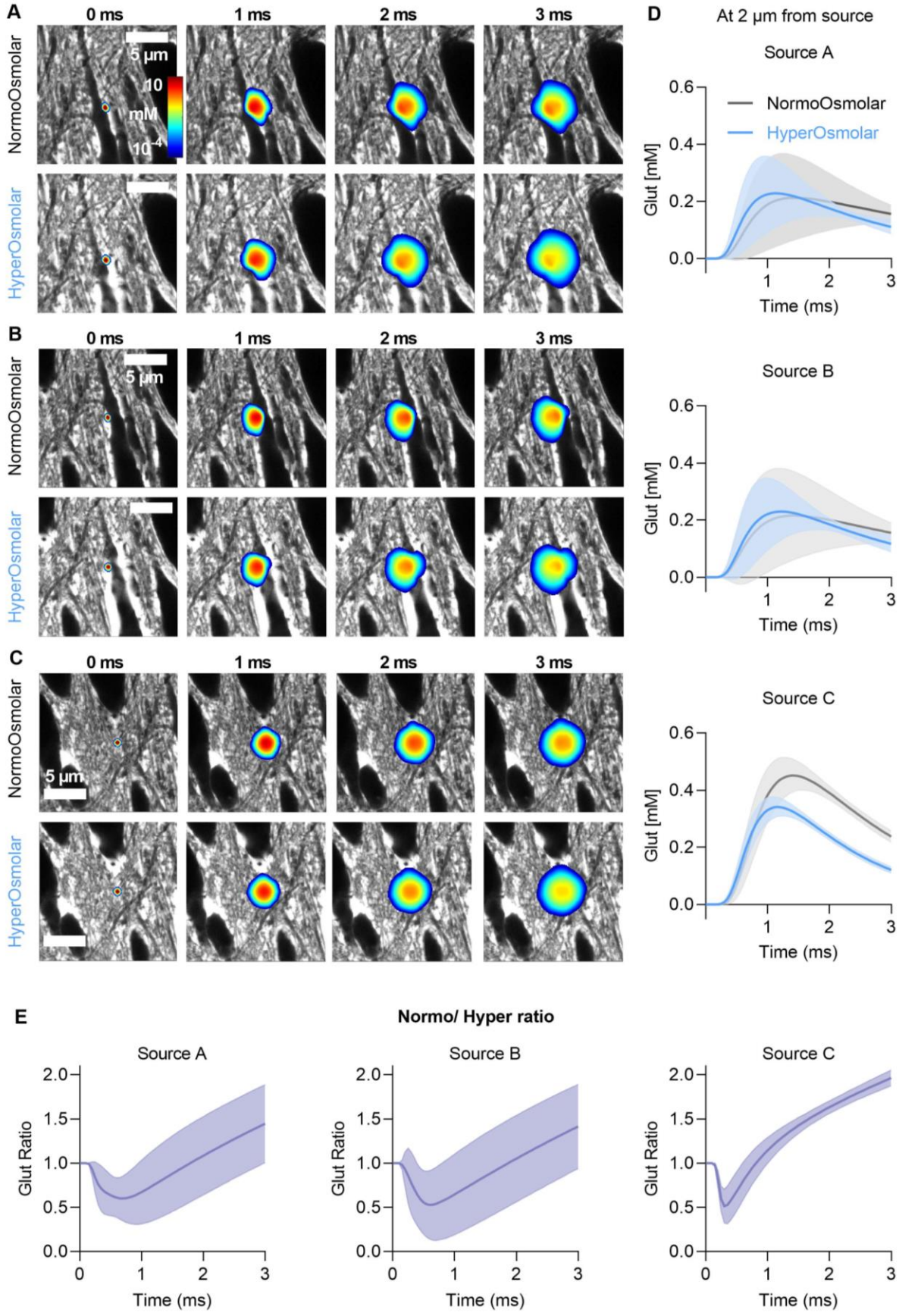
A
0 ms
1 ms
2 ms
3 ms
NormoOsmolar
HyperOsmolar
5 µm
10
mM
10-4
B
C
D
At 2 µm from source
Source A
Source B
Source C
NormoOsmolar
HyperOsmolar
Glut [mM]
Time (ms)
E
Normo/ Hyper ratio
Glut Ratio

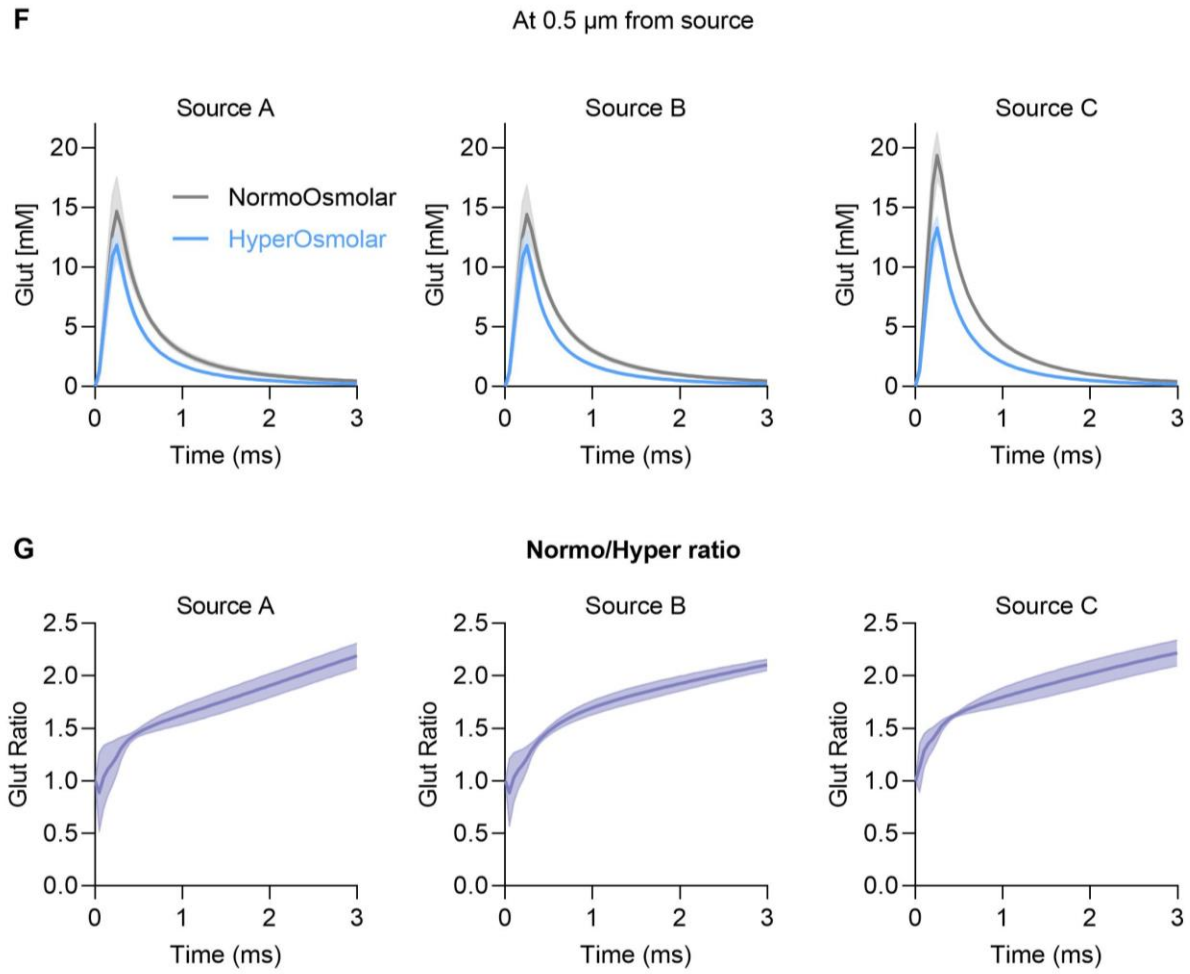

Figure 29. ← Starts in previous page. A, B and C) Simulations of glutamate spread over 3 ms after single vesicular release of glutamate at three different source locations A, B and C respectively. Simulations were run in a SUSHI image of the live brain ECS under NormoOsmolar (top image) and HyperOsmolar conditions (bottom image). Scalebar 5 µm. Color bar represents glutamate concentration from 0.1 µM to 10 mM. SUSHI images were borrowed from *Tønnesen et al. 2018,* [21]. D) Glutamate concentration profiles over time measured at 16 points at 2 µm from each of the source location (A: X = 315, Y = 250; B: X = 300, Y = 300; and C: X = 170, Y = 300) in NormoOsmolar (gray) and HyperOsmolar (blue) conditions. Data is represented as mean (line) + SD (shadow). E) Glutamate concentration ratio at 2 µm from each source location. Glutamate concentration in NormoOsmolar conditions over the concentration in HyperOsmolar conditions for each source location A, B and C. Data is represented as mean (line) + SD (shadow). F) Glutamate concentration profiles over time measured at 16 points at 0.5 µm from each source location (A, B and C) in NormoOsmolar (gray) and HyperOsmolar (blue) conditions. Data is represented as mean (line) + SD (shadow). G) Glutamate concentration ratio at 0.5 µm from each source location. Glutamate concentration in NormoOsmolar conditions over the concentration in HyperOsmolar conditions for each of the source locations A, B and C. Data is represented as mean (line) + SD (shadow).

Synaptic crosstalk

The next step was to apply the diffusion model to investigate if the ECS nanoscale morphology shapes diffusion of released neurotransmitters and if it imposes a directionality to modify signaling. To test our hypothesis, we simulated single vesicular release of glutamate onto a post-synapse on a dendritic spine in three different scenarios: in a SUSHI image of the dendritic segment with its surrounding ECS (SUSHI, estimated λ=1.58, α=0.27), in an image of the dendritic segment with homogeneous background instead of actual ECS structures (Auto-effect, λ=1.58, α=0.27) and a completely homogeneous background image with neither dendrite nor ECS (Homogenized ECS, λ=1.58, α=0.27). All the images were 300x300 pixels with a field of view size of 9x9 µm. The spread of glutamate was simulated over 3 ms in all the scenarios (Figure 30 A). In order to evaluate the effect of the brain ECS geometry on the diffusion of glutamate and synaptic crosstalk, we measured the arriving concentration at the locations of the neighboring spines of the dendritic segment (measuring points A and B in Figure 30 B and C) for the three scenarios. Presumably these neighboring spines will harbor other synapses. Thus, spillover from the release point would potentially alter the concentration at these neighboring synapses A and B leading to synaptic crosstalk. Our results show that the concentration arriving at the neighboring spine A is almost 700 times bigger in the homogenized ECS than in the SUSHI scenario, while is only 15 times bigger in the Auto-effect case (Figure 30 E and F). Notably, the concertation reaching neighboring spine B in the SUSHI case is almost 20 times less of what we observe in the Homogenized ECS, and nearly half of what we see in the Auto-effect scenario (Figure 30 G and H). Taking a closer look to the SUSHI scenario, we can observe that it predicts a directional glutamate spread towards spine B, while almost no spillover reaches spine A (Figure 30 E and G). Our simulations show that actually the glutamate concentration reaching spine B is 80 times greater than that reaching spine A in the SUSHI scenario, while in the auto-effect and homogenized cases this difference is gentler (Figure 30 B). As expected glutamate spread in the homogenous ECS has no preferred direction, so the higher concentration reaching spine B is just due to the fact that spine B is closer to the source point than spine A. As a result, our model predicts that homogenized ECS models using volume-averaged parameter will display faster and more intense diffusion profiles and are not capable of reporting differences in spread directionality. Regarding the auto-effect scenario, it shows diffusion profiles closer to the ones observed in the SUSHI scenario. Still glutamate spread towards both spines is quite balanced, Figure 30 B shows that the concentration reaching spine B is just around 15 times greater than the glutamate concentration arriving to spine A. Actually, compared to the homogenized ECS and bearing in mind that spine B is closer to the source, the auto-effect scenario predicts an enhance glutamate spread towards spine A. Altogether these predictions suggest that the structural information provided by the dendritic segment is not sufficient to capture the directionality that the ECS nanoscale geometry imposes.

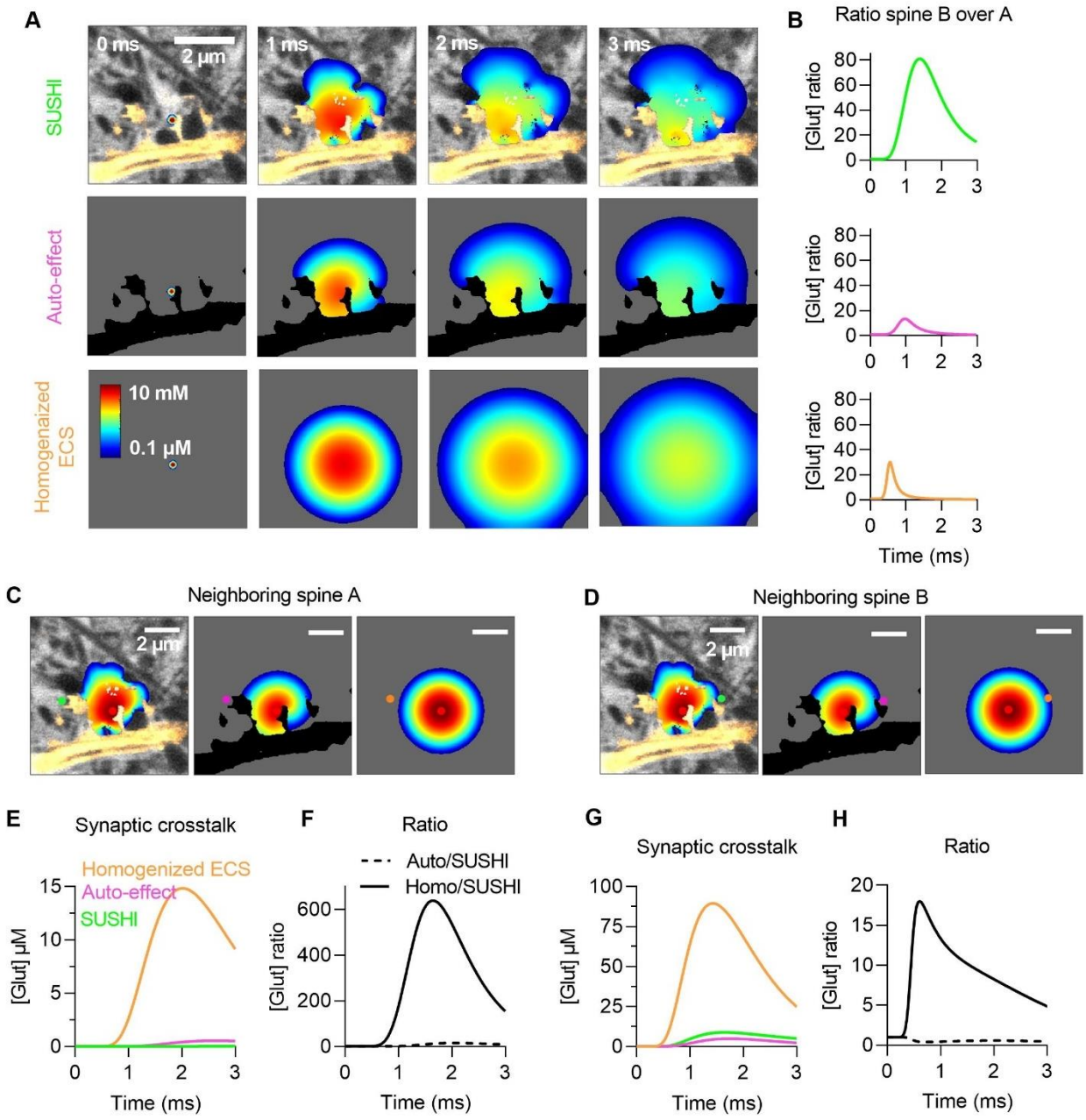

Figure 30. Synaptic crosstalk. A) Simulation of glutamate spread over 3 ms after single vesicular release of glutamate in 3 scenarios: in a SUSHI image (green), in a dendritic segment (pink) and in the homogenized ECS (orange). Images are 300x300 pixels. SUSHI images were borrowed from *Tønnesen et al. 2018,* [21]. B) Ratio of the arriving glutamate concentration at spine B over the arriving concentration at spine A for the three scenarios. C, D) Representative images of the glutamate spread showing the release point (X = 160, Y = 180) and the measuring points A (X = 70, Y = 160) and B (X = 225, Y = 160) respectively for each of the scenarios (SUSHI, Auto-effect, Homogenized ECS). E, G) Measured concentration over time at the spines A and B respectively, for each of the scenarios SUSHI (green), Auto-effect (pink) and Homogenized (orange). F, H) Ratio of Auto-effect and Homogenized concentration profiles over the SUSHI concentration profile for both spines A and B respectively. Scalebar 2 µm. Color bar from 0.1 µM to 10 mM.

Index of variation over distance

To test how the nanoscale geometry of the ECS shapes the dispersion of molecules at different distances from the source, we ran simulations of single vesicle release of glutamate and its spread over 2 ms in four different SUSHI images of the live brain ECS (Figure 31 A and B). Images in A were 400x400 pixels with a field of view size of 12x12 µm, borrowed from *Tønnesen et al. 2018* [21]. The images in A had a calculated λ=1.6, α=0.44 (top) and λ=1.54, α=0.31 (bottom). Images in B were obtained in our lab and they were 500x500 pixels with a field of view size of 33x33 µm (λ=1.66, α=0.32 and λ=1.61, α=0.31 for the top and bottom images in B, respectively). To account for the dispersion of molecules we used the index of dispersion (also known as relative variance), which reports how far a set of values are spread out from the mean. In order to estimate the index of dispersion of glutamate in each case, first we measured the concentration at time 2 ms at 16 different concentric points at different distances (see white concentric circles in Figure 31 A): 0.2, 0.5, 1, 2, 3 and 5 µm for images in A, and 0.5, 1, 2, 3, 5 and 7 µm for images in B. Then, for each point at a given distance we measured the index of dispersion of that point as follows:

Equation 16 for a given point x, y at a given distance.

$$Index\ of\ dispersion = \frac{(C_{x,y} - C_{mean})^2}{C_{mean}}$$

Were $C_{x,y}$ is the concentration at a given point at a given distance and C_{mean} is the average concentration of all the points at the same distance from the source.

For each simulation in Figure 31, the indexes of dispersion were normalized by dividing by the highest index of dispersion value. As a result, Figure 31 C shows that in the four simulations, the index of dispersion decreases with distance. As glutamate is released, very quickly (at 0.5 µm distance) molecules will hit obstacles in some directions but not others. Then as we move a few µm away from the release source particles will start finding obstacles in the other directions as well. Thus, the concentration pattern is smoothened and the index of dispersion decreases in the ECS. When particles reach big cellular structures, they will again impose a directionality to the diffusion pattern at larger scales. In this scenario, we will observe a high index of dispersion at further distances from the source (2-3 µm), as shown in Figure 31 C (corresponding to top B image).

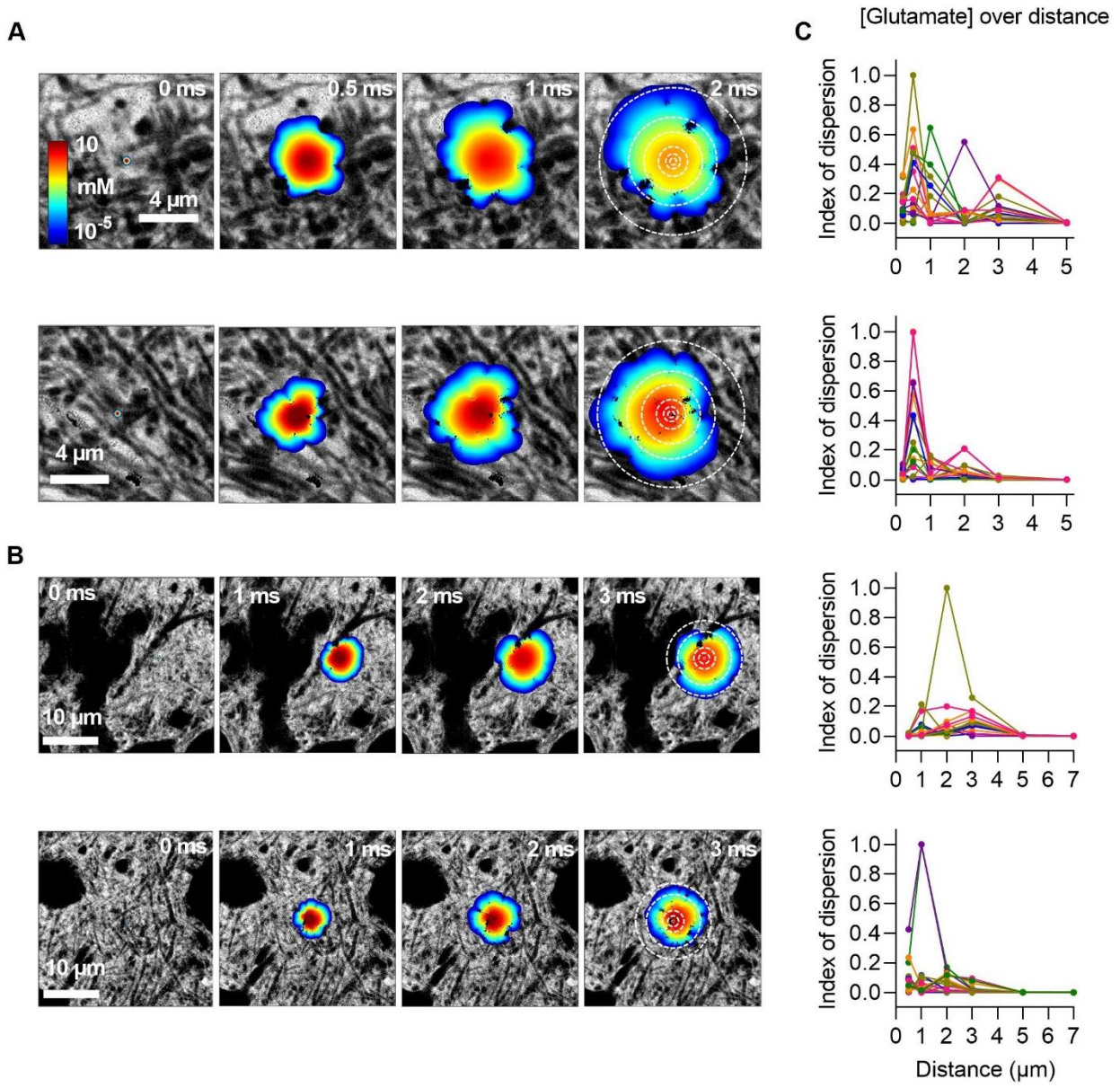

Figure 31. Index of dispersion over distance. A) Simulations of glutamate spread over 2 ms after single vesicular release of glutamate in two different fields of view. Scalebar 4 µm and color bar from 10^{-5} to 10 mM. Dotted white concentric circles represent the radiuses at which the index of dispersion was estimated: 0.2, 0.5, 1, 2, 3 and 5 µm. SUSHI images were borrowed from *Tønnesen et al. 2018,* [21]. B) Simulations of glutamate spread over 3 ms after single vesicular release of glutamate in two different SUSHI images. Scalebar 10 µm and color bar from 10^{-5} to 10 mM. Dotted white concentric circles represent the radiuses at which the index of dispersion was estimated: 0.5, 1, 2, 3, 5 and 7 µm. C) Normalized index of dispersion of the glutamate concentration measured at 16 concentric points at different radial distances from the source point, in each the fields of view.

Glutamate Spread

A recent study (*Matthews 2022*) has put focus in understanding glutamate spread between synapses in the brain neuropil [91]. In this publication, glutamate spread is analyzed optically after its release in hippocampal mouse brain slices using glutamate uncaging or actual synaptic glutamate. *Matthews*, reports that glutamate can spread and activate synaptic receptors within a neighborhood of 2 µm. We wanted to use our model to learn more about how perisynaptic ECS geometry may shape such extracellular synaptic crosstalk, and if indeed ECS geometry is involved in shaping crosstalk. To do so, we simulated single vesicular release of glutamate and its spread over 2 ms in a homogenized ECS image with λ=1.58, α=0.27. We ran simulations with different extracellular basal glutamate concentrations of 0.1, 1 and 10 µM, as reported from different animal models and brain regions [92]–[95], (Figure 32 A). Figure 32 B shows the glutamate concentration profile over time and distance for the different basal concentrations. In order to assess the range of glutamate spread, we identified where the concentration was above a 5% over the basal concentration (white lines, Figure 32 C) for different distances from the source (0.2, 0.5,1 ,2 and 4 µm). Our results showed that at 4 µm glutamate concentration falls below the 5% of the basal concentration for the 1 and 10 µM scenarios, but for the 0.1 µM basal concentration the concentration was still slightly above the 5% threshold. These model results suggest that for physiological values of basal glutamate concentration, glutamate would have a > 5 % effect only at distances below 4 µm, in excellent agreement with *Matthews* results [91].

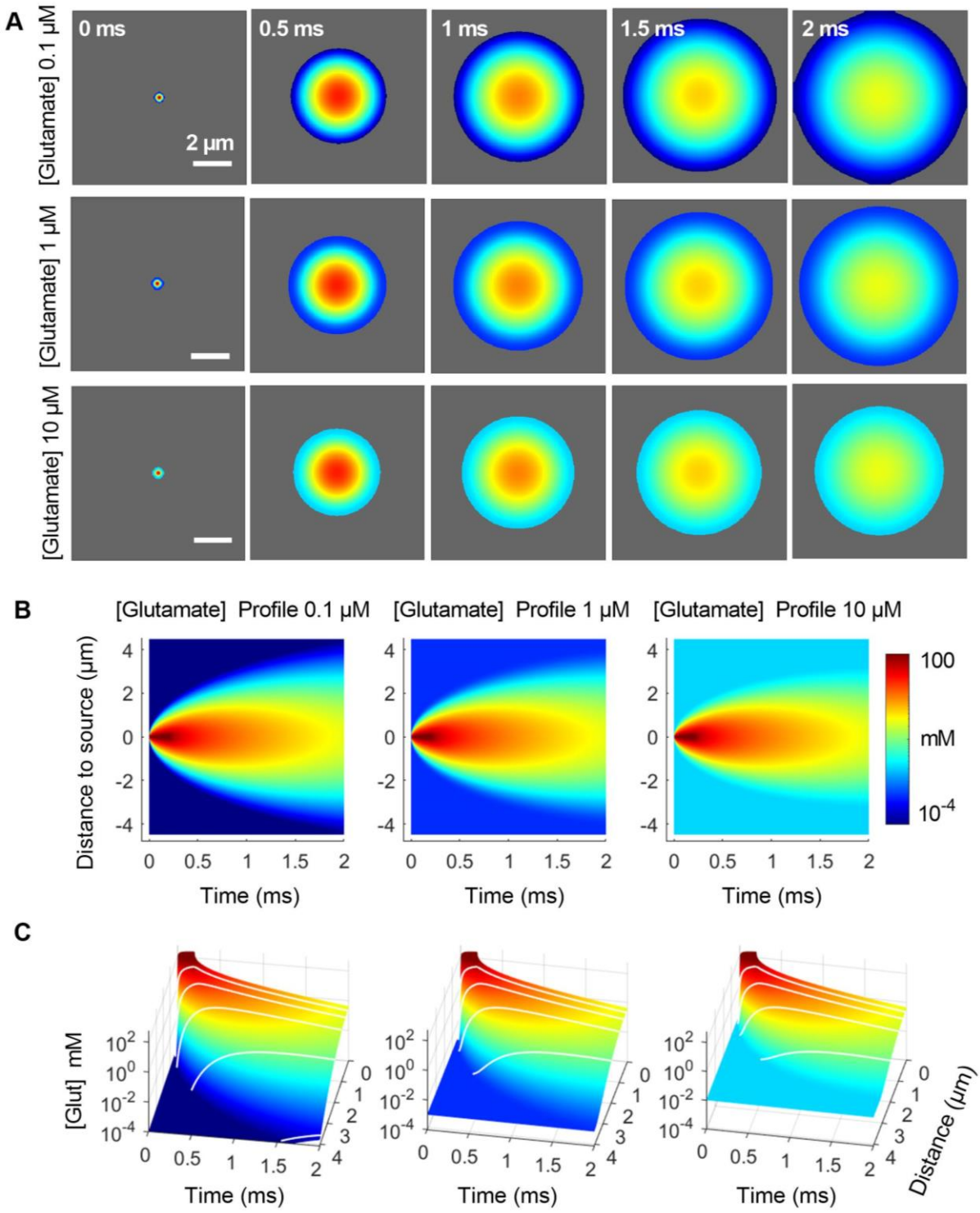

Figure 32. Glutamate spread. A) Simulations of glutamate spread for different ambient concentrations of glutamate: 0.1 µM (upper), 1 µM (middle) and 10 µM (bottom). The simulations ran for 2 ms after single vesicular release of glutamate in and homogenized ECS with a volume fraction of 0.27 and tortuosity of 1.58. Scalebar 2 µm and color bar from 10^{-4} to 100 mM. B) 2D glutamate concentration profile, the glutamate concentration (colormap) is represented against the distance to the source and the time for the different glutamate ambient concentrations: 0.1 µM,1 µM and 10 µM. C) 3D glutamate concentration profiles, the glutamate concentration is represented in 3D

(colormap) against the distance to the source and the time for the different ambient concentrations. White lines represent the concentration above 5% the ambient concentration.

Tensor-maps

Anisotropy both in the morphology of the ECS and in the diffusion of particles within the live ECS has been observed at macro-scales using RTI and IOI methods [7], [14]–[16]. We hypothesize that diffusion in the microscale live ECS will be also anisotropic. Super-resolution shadow imaging shows that the microscale morphology of the live ECS can be very directional in some areas, such as along dendrites or axonal processes. Thus, our goal is to investigate whether diffusion is also anisotropic in the microscale and what is the scale and variability of this directionality.

To investigate the scale and variability of the directionality in the microscale live ECS, we ran multiple subsequent simulations of single vesicular release of glutamate and its spread over 100 µs at hundreds of different source point in two SUSHI images (Figure 33). The SUSHI image displayed in Figure 33 A was 400 x 400 pixels with a field of view size of 75 x 75 µm (λ = 1.87, α = 0.22). SUSHI image B was 400 x 320 pixels with a field of view size of 50 x 40 µm corresponding to the yellow dashed rectangle in Figure 33 A at higher resolution (λ = 1.6, α = 0.16). For each simulation of glutamate spread we identified the most prominent direction of the diffusion pattern after 100 µs, and we assigned a vector to that direction with a corresponding direction (angle) and magnitude. Details about how these tensor-maps were obtained are explained in the Materials & Methods (Matlab code and post-simulation analysis) section.

Figure 33 A shows that most of the tensors present a strong directionality impose by the surrounding ECS nanoscale geometry, suggesting that as soon as a neurotransmitter is released in the ECS its diffusion will be anisotropic towards the regions offering less resistance to diffusion. Also, it can be appreciated that there is no overall preferred directionality, the general tensor direction seems quite random.

Taking a closer look to the ECS structure, we observed that there is strong directionality in some areas, such as along the dendrites or around cell somata (yellow rectangles Figure 33 B). However, in regions were the ECS is much more homogeneous our tensor map looks random, as shown Figure 33 B (green rectangle).

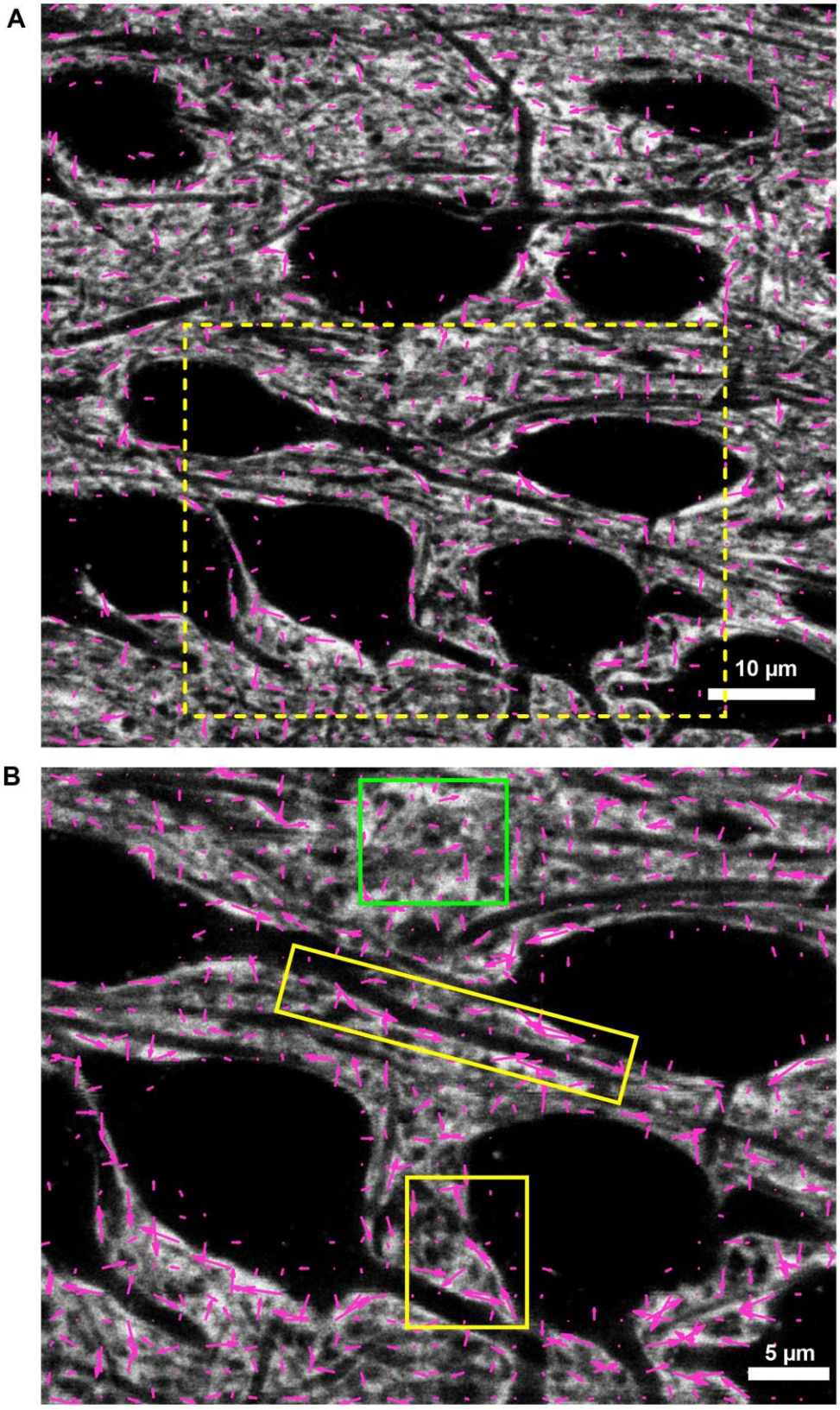
A
10 µm
B
5 µm

Figure 33. ← Previous page. Tensor-map. A) Tensor distribution of 961 source points in a SUSH image (400 x 400 pixels) of the live brain ECS with estimated λ = 1.87 and α = 0.22. Scalebar 10 µm. The yellow rectangle corresponds to the field of view shown in B. B) Tensor distribution of 771 source points in a SUSH image (400 x 320 pixels) of the live brain ECS with calculated λ = 1.6 and α = 0.16. Scalebar 5 µm. In both images A and B arrows correspond to the principal direction at each source point. The origin of each arrow corresponds to the source location. Arrows are scaled 1.5:1.

Discussion

The goal of this second part of the thesis was to develop a new and innovative computational model based on super-resolution shadow images, and to show its potential to investigate the role of the nanoscale geometry of the live brain ECS on volume transmission.

We consider that this computational model of diffusion in the brain ECS provides numerous advantages compared to existing state-of-the-art modelling methods. Firstly, compare to the more common and conventional methods used to study diffusion, such us real time iontophoresis (RTI) and integrative optical imaging (IOI) [13], [14], [71]–[74], SUSHI-based modelling provides nanoscale visualization and simulation of diffusion. Secondly, our model is the only one to utilize actual ECS geometries from live tissue imaging, and therefore expectedly will come closer to reporting the ground truth and the true physiological variability in diffusional properties of the ECS. Most of the existing models used to investigate diffusion at different spatial and temporal scales are based on artificial ECS structures [78], [79]. While these artificial ECS based models might be sufficient to study average diffusional properties over large distance, they fail to predict diffusion locally, and they are blind to the key physiological variability that exists in the brain neuropil. It is true that electron microscopy (EM) reconstructions overcome this limitation as they provide sub-micron resolution of the neuropil. However, they require tissue fixation that is associated with fixation artifacts that alter ECS geometry and the ECS volume. Although the cryo-fixation technique seems to preserve better the ECS structure than the traditional chemical fixation, it has not yet been compared to live tissue slices [82]. In this regard, SUSHI-based modelling uses sub-micron ECS structural information from live brain slices. It is worth mentioning that, so far, all the computational models based on real microscopy images threshold and binarize the images they use. As a result, these images either use low threshold values considering just big obstacles and missing microscale structural information. Or they use high threshold values resulting in highly restrictive geometries to diffusion. On the contrary, SUSHI images use the whole bit depth of the images and as a result macroscale structures are not at odds with preserving nanoscale structural information. Thus, the bigger the bit depth of the SUSHI images we use, the finer the difference we can find in diffusion patterns.

Recent approaches, like single-walled carbon nanotube tracking (SWCNTs), also provide maps of local ECS diffusion with nano-scale resolution in acute brain slices, though they are more limited in the ECS geometric information they provide [24]. Further, the SWCNT approach is limited to study diffusion of particles over few microns as particles get trapped and do not diffuse freely in the ECS. Thus, another advantage of the computational model proposed, is that it allows simulation of diffusion at different spatio-temporal scales. SUSHI-based modelling can be used to predict diffusion of neurotransmitters around individual dendritic spines (few microns) or to model diffusion over large spaces (hundreds of microns). Other strong points of our computational model include the straightforward possibility of performing 3D diffusion simulations using z-stacks of SUSHI images. Given that 3D modelling requires a high computational workload, we have developed a pseudo-3D model to account for diffusion in the

z-direction while preserving the efficiency of 2D simulations. Also, the model can accept any free diffusion coefficient and thus model different sized particles.

Interestingly, our predictions about the index of dispersion of molecules over distance show that close to the source point molecules very quickly hit an obstacle in one direction but not in the others, resulting in high variability of the molecular distribution. But, beyond a few microns everything is smoothen. Moreover, our simulations to assess synaptic crosstalk in different scenarios suggest that the nano-scale structure of the live brain ECS will have huge impact in cell signaling over short distances. Taken altogether, the most important strength of our computational model is its ability to capture the diffusion of a single vesicular release of neurotransmitters, where the dispersion of molecules is highly heterogeneous and the impact on synaptic crosstalk is greater. In line with this, the tensor maps obtained also suggest strong directionality in the diffusion of neurotransmitters towards regions of the ECS offering less resistance to diffusion. Our model predicts that this directionality is mainly imposed by the ECS structure, as appreciated by the strong directionality close to the dendrites and cellular bodies, while in areas with a less defined ECS geometry the direction of diffusion looks random. Another key point of SUSHI-based modelling is that it allows us to investigate how changes in ECS volume affect the diffusion of transmitters in the live brain parenchyma with submicron resolution. For the first time we simulated diffusion of glutamate before and during ECS expansion caused by hyperosmotic stress in real images of the live brain ECS. Our predictions suggest that ECS swelling due to hyperosmotic stress will have a stronger dilution factor in regions where the ECS is more constrained, and therefore it will have higher impact on cellular signaling in these areas. These experiments further confirm that that a hyperosmotic challenge expands the ECS also around neural somata, which supports our finding that a similar challenge in acute brain slices lowers tonic GABAergic inhibition by presumed volume dilution of synaptically released GABA.

SUSHI-based modelling also presents some limitations. On one hand, SUSHI live imaging is constrained by the molecular labeling options, the tissue volumes we can address and the sample type, since currently the technique is only applicable in organotypic tissue slices. Consequently, visualization and quantification of tissue organization from regional to single synapse level is not straight-forward. Recently developed technology, Comprehensive Analysis of Tissues across Scales (CATS), overcomes this limitation providing an integrated labelling, optical imaging and analysis platform to investigate tissue architecture, subcellular morphology and molecular interactions in their structural context [96]. To visualize cellular structures down to the single-synapse level, CATS uses SUSHI imaging in fixed tissue.

On the other hand, although our simulations closely match published RTI data in live brain ECS and free medium we observed a slightly slower recovery at the end of the iontophoretic pulse. It is true that RTI measurements only considers a few measuring points and based on our simulations we would expect to have large variation between the different measuring points, and this could explain our differences. This makes it difficult to compare our simulations with RTI data. Also, while our simulations of diffusion for small molecules are in line with the published

simulated data from *Nicholson 2001* [85], simulation of bigger molecules resulted in faster diffusion than the published data. However, the published simulations imposed different values of λ for the different molecules, while or simulations were performed in the same field of view with the same reported λ for all the molecules. Different computational models use different parameters and geometries that, at the end, make it very difficult to compare the data obtained, what brings us to our next point. We have not yet validated the computational model against real experimental data, which is the only way to corroborate that our predications hold true, and which we plan to do.

Regarding future directions of SUSHI-based modelling, our model has the potential to accept time-lapse SUSHI images and thus perform 4D simulations to study how the dynamics of the ECS nano-scale structure affect diffusion and synaptic communication.

Finally, with all these ideas in mind, we believe that SUSHI-based modelling is a powerful technique that can provide new insights into the role of the sub-micron structure of the live brain ECS in shaping the diffusion of transmitters, and as a result, shaping cellular signaling.

Conclusion

To conclude this part, we have developed a novel computational model of diffusion in the live brain nanoscale ECS.

The model was first tested against published RTI measurements in live brain ECS and in free diffusion medium from *Hrabětová 2007.* Our simulations predicted the RTI diffusion curves for TMA^+ both in free medium and in brain ECS, although the decay in our simulations was slightly slower. Then the model was compared against published simulations for different sized molecules from *Nicholson 2001* [85], [87]. Our simulations of diffusion of big molecules, such as BSA and dextran 70K, lead to faster diffusion patterns than the published ones. With this in mind, we can conclude that though these comparisons helped us to verify that our simulations are in line with published data of diffusion in brain ECS and free medium, they are not enough to validate it. So future steps will be focused on further validating the model against experimental diffusion measurements in live brain slices using SUSHI technique.

The SUSHI-based model proposed, works both in 2 (x, y) and 3 (x, y, z) dimensions. In addition, we proposed a pseudo-3D computational model capable of simulating the diffusion observed in 3D but with the efficiency of a 2D computational model.

The work presented in this section shows that our SHUSHI-based model has great potential to investigate diffusion in the live nano-scale ECS. Our predictions on synaptic crosstalk suggest that the ECS submicron geometry in live tissue shapes the diffusion of neurotransmitters and imposes a directionality. In fact, the ECS structure not only affects diffusion of neurotransmitters in terms of intensity but also in terms of speed. Moreover, our simulations show that the ECS sub-micron geometry has huge impact in the dispersion of molecules. Close to the source (less than 1 µm), molecules very quickly hit an obstacle in one direction but not in the others, resulting in high variability of the concentration distribution. Few microns away from the source everything is smoothen, as particles will start finding obstacles in the other directions as well, and the variability decreases.

In addition our glutamate spread simulations for different extracellular basal concentrations of glutamate are in excellent agreement with *Matthews et al. 2022* [91].

All together we conclude that, we have developed an innovative computational model based on SUSHI images to understand local microscale diffusion of transmitters in the live brain ECS. The key aspect of SUSHI-based modelling is its ability to simulate diffusion on local nano-scale regions were the variability of the molecular dispersion and the impact on synaptic communication are the most significant. Thus, we conclude that computational modelling based on SUSHI images from the live brain ECS provides new opportunities to investigate how microscale diffusion around individual cellular structures shapes synaptic crosstalk.

GENERAL CONCLUSION

We set out to identify putative functional roles of the ECS structure in shaping signaling in the brain neuropil.

We first took an experimental approach to prove that varying ECS structure globally can impact volume transmission in the form of tonic GABAergic inhibition, and that this occurred independently of synaptic GABA release or membrane properties of the postsynaptic neuron. This novel regulation mechanism is independent and complementary to existing regulation mechanisms that take into account primarily release mechanisms, e.g. release frequency and quantal size, as well as receptor numbers and states. Astrocytes also play a role, though in the hippocampal circuit that we worked with, tonic inhibition mainly drives from synaptic spill-over. It is notable that investigating strictly cellular functional properties in the context of hyperosmotic ECS volume expansion, these would not change and the observed change in tonic inhibition would go unexplained. Indeed, the combination of patch-clamp electrophysiology to measure both synaptic and tonic GABAergic signaling was crucial for our experiments, as it allowed us to rule out alteration in synaptic GABA release as a contributing factor in our results.

The observation that ECS dynamics may functionally alter signaling has major putative implications for how we understand signaling and circuits. This becomes clear from considering the common physiological structural dynamics that occur in response to cellular signaling, as well as those occurring over the glymphatic system diurnal rhythm. And our findings are likely to be general and valid also for other volume transmitters, which will be interesting to explore.

Another highly interesting aspect is that ECS regulation of signaling constitutes a way for cells and circuits to communicate beyond synaptic connections, i.e. inter-circuit signaling that may be important for integrative function of the brain. It is also notable that ECS regulated volume transmission occurs on much slower time scales than synaptic signals, which may be important for understanding the temporally more extended manifestations of circuit signaling, such as behavior and consciousness.

To look beyond the global roles of the ECS in regulating signaling, in the second part we took a computational modeling approach to understand how the perisynaptic ECS may regulate glutamatergic synaptic crosstalk. Little is known about glutamatergic crosstalk via the ECS, and whether it plays a role in signaling.

Our modelling efforts found that the ECS can have a dramatic impact on spillover, so that neighboring synapses at equal distance to a common source synapse may see manifold different concentrations of spilled glutamate, and at different time points. It appears that ECS structure is indeed directly a requirement for credibly predicting such synaptic crosstalk. While we have not touched upon the functional consequences of the predicted levels of crosstalk in this thesis, this is an essential aspect in our agenda. Though given the on average 0.5 micron distance between synapses in some areas, and thus conceivably much smaller in some cases, it appears more than

likely that crosstalk can modulate circuit activity by activating neighboring synapses on the same and different neurons. This may also have implications for synaptic plasticity, and here it is interesting to note that induction of plasticity on one spine will impact the ability of neighbors to undergo plasticity, which has conventionally been explained through intra-cellular mechanisms and competition for resources [97]. In the context of plasticity, it will be interesting to look also at other molecules and glutamate, including neuromodulators such as neuropeptide Y, dopamine and others.

Overall, we have shown that the ECS is a likely impactful regulator of signaling at two extreme spatio-temporal cases: globally in brain slices and peri-synaptically. However, volume transmission and synaptic crosstalk are not two discrete phenomena, and one may be considered a version of the other. Between the extreme cases there is an interesting middle ground yet to be investigate, e.g. to explore regional variations and directionality in volume transmission, or how synaptic crosstalk is different between glutamatergic synapses on spines and GABAergic synapses on dendritic trunks, respectively, where the perisynaptic ECS will by nature be different. This thesis has answered a few questions pertaining to the functional roles of the ECS, but perhaps more importantly, it has raised new ones, and provided experimental and modelling tools to start addressing them.

COLLABORATIONS

Functional assessment of NAV1.1 channel

Besides working on the project related to this thesis, we have work in collaboration with Ana Ricobaraza and Ruben Hernandez-Alcoceba to develop genetic tools in the context of Dravet syndrome [98].

Introduction

Dravet syndrome formerly known as severe myoclonic epilepsy of infancy (SMEI), is a genetic encephalopathy characterized by severe epilepsy combined with motor, cognitive, and behavioral abnormalities. It usually appears during the first year of life and is treatment-resistant in most of the cases. Current antiepileptic drugs achieve only partial control of seizures and provide little benefit on the patient's neurological development. In >80% of cases, the disease is caused by pathogenic variation in the *SCN1A* gene, which encodes the alpha subunit of the Nav1.1 voltage-gated sodium channel. Nav1. 1 channel, under physiological conditions, permits the sodium influx from the extracellular space into the cytosol after depolarization of the nerve membrane.

Novel therapies in this field aim to restore *SCN1A* expression in order to address all disease manifestations. This collaboration aimed to provide evidence that a high-capacity adenoviral vector harboring the *SCN1A* cDNA is feasible and able to express functional Nav1.1 in neurons. To do so we contributed with *in-vitro* experiment on different cells lines, were we evaluated the function of Nav1.1 channel. Altogether, the results presented by *L. Mora-Jimenez 2021* provide proof of concept for gene supplementation in Dravet syndrome and indicate new directions for improvement [98].

Materials & Methods

In this section, only the experiments which with we collaborated are described.

Cell Cultures and transfection

HEK-293 cell line and Human Nav1.1 Sodium Channel Cell Line were maintained in DMEM. SH-SY5Y cells were maintained in a 1:1 mixture of Eagle's minimum essential medium and F12 medium supplemented with 1% non-essential amino acids. All culture media were supplemented with 10% fetal bovine serum (FBS), 100 U/mL penicillin, 100 µg/mL streptomycin, and 2 mM l-glutamine. Reagents were obtained from Gibco (Gaithersburg, MD, USA). All cells were maintained at 37°C with 5% CO2 in a humidified incubator. Cells were routinely tested for mycoplasma contamination. Cells were maintained in T75 or T25 flaks and then seeded in coverslips in 24 well plates at 80%–90% confluence, for electrophysiological recordings. HEK-293 and Nav1.1. cells were seeded at a density of 1.2 – 2 x 10^5 and SH-SY5Y cells were seeded at 2.5 × 10^5.

Transfection was performed 24 h by Lipofectamine 2000 (Invitrogen) using 0.5 µg of each firefly luciferase reporter plasmid. The transfection mixture was removed 5 h later and replaced by fresh culture medium.

All cell lines were provided by our collaborators.

Electrophysiological recordings

Electrophysiological recordings were obtained from cultured HEK-293 cells at 24h to 72h after plasmid transfection. The coverslip with attached cells were placed in a recording chamber and perfused at a rate of 2.5 mL/min with ACSF, containing (in mM): 119 NaCl, 2.5 KCl, 1.6 $MgCl_2$, 26 $NaHCO_3$, 1 NaH_2PO_4, 5 HEPES, 10 Glucose, and 2.5 $CaCl_2$ (300-310 mOsm and 7.4 pH). Transfected cells were identified visually through their GFP expression using standard epifluorescence microscopy integrated on the patch-clamp setup (Micro Control Instruments). Control cells, not expressing the NaV1.1 channel, were randomly picked in parallel age-matched non-transfected cultures. Whole-cell patch-clamp recordings were made with glass pipettes filled with standard intracellular solution (in mM): K-gluconate 125, KCl 5, HEPES 10, EGTA 1, Mg-ATP 4, Na2-GTP 0.3, NaP-creatine 10 and L-ascorbic acid 3, 286 mOsm, 7.23 pH, offering a pipette tip electrical resistance between 3-5 MΩ. Recordings were performed at 32°C.

The membrane potential was stepped in increments of 5 mV for 200 ms at 1 sec interval from -80 mV to +40 mV, and the activation voltage for the NaV1.1 channel was determined by plotting the membrane potential against the measured peak membrane current for each voltage step. To verify that any observed current was indeed mediated by a sodium channel, at the end of the experiment we applied 2 µM of the voltage-gated sodium channel blocker tetrodotoxin (TTX) and repeated the voltage step protocol. Data acquisition was performed at 5 kHz using a HEKA EPC-10 amplifier via PatchMaster software, followed by analysis using FitMaster software (HEKA Elektronik).

Results

The activation voltage for the NaV1.1 channel was measured for each of the cell lines by plotting the membrane potential against the measured peak membrane current for each voltage step (Figure 34 B-G). Figure 34 A shows a summary table of the channel activation threshold for each of the cell lines used. These results suggest that activation threshold of the channel appears to be similar in the Nav1.1 cell line, in HEK cells with the plasmid, and in HEK cells with the virus. Though it seems that we have to wait 48h after virus transfection for the HEK cells to optimally express the Nav1.1 channel. At 24 hours, although they expressed GFP when using epifluorescence microscopy, few cells have the sodium current and the threshold is slightly different.

Taking a closer look to the current-voltage curves of the HEK-293 cell, it does look like transfection slightly changes the membrane properties of the HEK cells, evident as a difference in slope of the baseline between Figure 34 B and F below. Regarding SH5Y5 cells, they present a

background sodium current that is presumably mediated by other NaV channels than 1.1, making it difficult to verify functional expression of the NaV1.1.

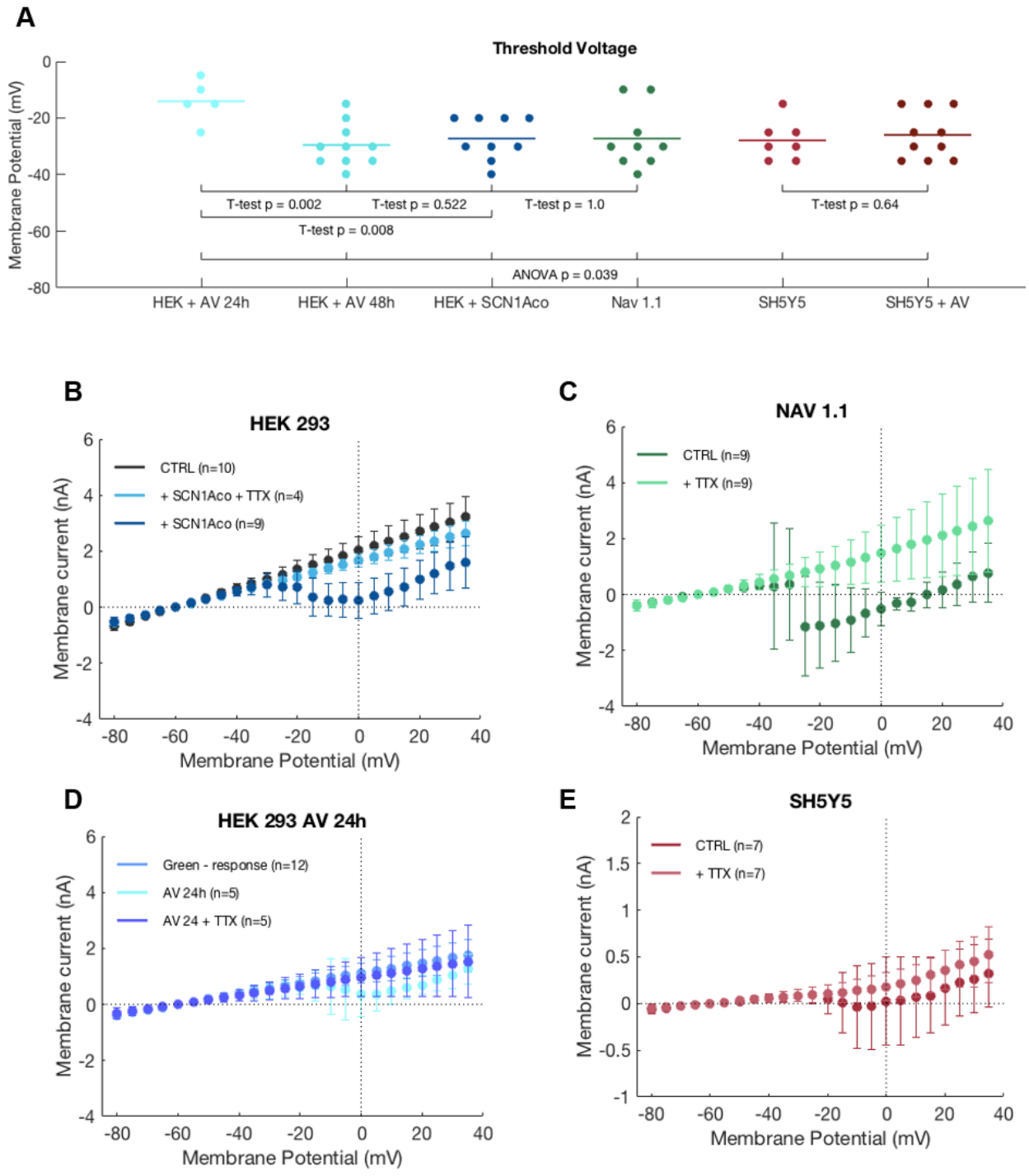

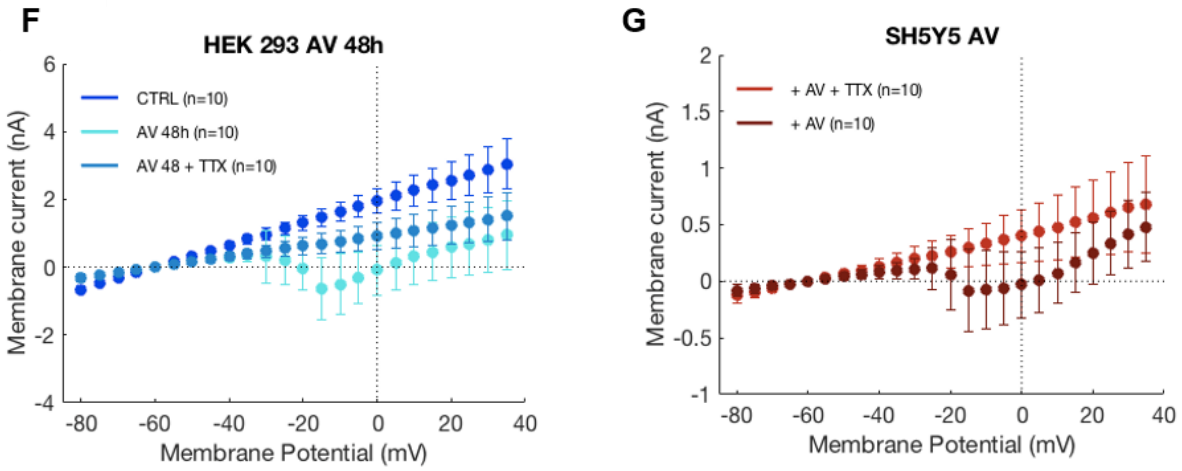

Figure 34 ← Starts in previous page. Activation voltage for Nav1.1 channel and current-voltage curves. A) Activation voltage for the NaV1.1 channel was measured for each of the cell lines HEK-293 24h after viral infection (turquois), HEK-293 48h after viral infection (light blue), HEK-293 after plasmid transfection (dark blue), Human Nav1.1 cell line (green), SH5Y5 cell line (light red), SH5Y5 after viral infection (dark red). B) Membrane current against membrane potential for increasing voltage steps for control HEK-293 cells (black), transfected HEK-293 in the presence of TTX (dark blue) and without TTX (light blue). C) Membrane current against membrane potential for increasing voltage steps for Nav1.1. cells in the presence of TTX (light green) and without TTX (dark green). D) Membrane current against membrane potential for increasing voltage steps for non-GFP expressing HEK-293 cells (dark blue), HEK-293 24h after viral infection in the presence of TTX (purple) and without TTX (light blue). E) Membrane current against membrane potential for increasing voltage steps for SH5Y5 cells in the presence of TTX (light red) and without TTX (dark red). F) Membrane current against membrane potential for increasing voltage steps for non-GFP expressing HEK-293 cells (blue), HEK-293 48h after viral infection in the presence of TTX (dark blue) and without TTX (light blue). G) Membrane current against membrane potential for increasing voltage steps for SH5Y5 cells after viral infection in the presence of TTX (light red) and without TTX (dark red).

Two-Photon *in-vivo* assessment of diffusion

During my PhD stay I worked in Lauritzen Lab at the Panum Institute (Copenhagen, Denmark). For the time there, I was under the supervision of assistant professor Krzysztof Kucharz with the purpose of learning from his expertise in two-photon (2P) *in-vivo* imaging and use it to investigate diffusion of different sized molecules in the *in-vivo* mouse brain.

Introduction

One of the main goals of Lauritzen Lab is to develop experimental and analytical tools to investigate the properties of the brain blood barrier (BBB), a vascular barrier system that limits the passage of substances into the brain parenchyma. Particularly, professor Kucharz is focused on understanding BBB permeability and diffusion properties in the *in-vivo* brain, both in physiological and in pathological conditions (i.e. after stroke) [99], [100]. The main goal of his work is to quantitatively measure the permeability of the BBB in real time as well as the diffusion on nanoparticles in the brain ECS using *in-vivo* 2P microscopy [101]. The purpose of my PhD stay in Lauritzen Lab was to learn to autonomously do 2P *in-vivo* imaging to be able to implement it in my home lab, as well as to use the technique to investigate diffusion of different sized particles in the *in-vivo* mouse brain.

Materials & Methods

In this section are described all the procedures that I performed during my PhD stay.

Animals

The experimental work presented here was performed in C57BL6J male and female wildtype (WT) mice used between the ages of 4 to 6 months and with weights between 20-26 gr. Mice were housed in ventilated cages at room temperature and 50 % relative humidity, under a 12-h light–dark cycle. They were provided with food and water *ad libitum* and with nesting materials.

All procedures were performed according to The Danish National Committee on Health Research Ethics following the guidelines established by the European Council's Convention for the Protection of Vertebrate Animals Used for Experimental and Other Scientific Purposes. All efforts were made to avoid animal suffering and to minimize mice pain and stress.

Animal preparation for acute imaging

First, mice were anesthetized intraperitoneally (i.p.) with xylazine (10 µg /g animal) and ketamine (60 µg/g animal). To keep mice anesthetized during the all the procedure, ketamine was i.p. injected at 30 µg/g animal every 20-30 minutes. Animals were maintained at 37C using a rectal thermistor probe and a heating pad.

Then, a tracheotomy was performed for mechanical respiration (180–220 ml volume; 190–240 strokes/min) with O2-supplemented air (1.5–2 ml/min, MiniVent Type 845 ventilator, Harvard Apparatus). In some experiments, two catheters were inserted by the lab technician or the

supervisor, one into the left femoral artery for injection of compounds and nanoparticles, and for monitoring mean arterial blood pressure (MABP; Pressure Monitor BP-1, World Precision Instruments), and the other into the femoral vein for anaesthesia infusion during imaging. Mice that were not catheterized, were continuously administered ketamine i.p. injections (30 µg/g animal) every 20-30 minutes until the end of the experiment. After tracheotomy and catheterization (if performed) the animal was turned to the prone position and the scalp was removed. The periosteum was also removed with a FeCl3-soaked cotton bud, and the exposed skull was glued (Loctite Adhesives) to a custom-made metal head plate.

We did a craniotomy over the right somatosensory cortex (3 mm lateral, 0.5 mm posterior to bregma) using a 4mm diameter dental drill at 45000 rpm. The bone flap was carefully lifted and we quickly removed the dura mater membrane. Once the brain was exposed we quickly added warm 1 % low melting point agarose on the brain surface. Agarose was diluted 1:100 in artificial cerebro-spinal fluid (ACSF composition in mM: NaCl 120, KCl 2.8, Na2HPO4 1, MgCl2 0.876, NaHCO3 22, CaCl2 1.45, glucose 2.55, pH = 7.4). Then, an imaging coverslip (~4 × 4 mm, 0.08-mm thick; Menzel-Gläser) was placed over the craniotomy, leaving a ~0.5-mm gap for glass micropipette insertion.

Mice were then transferred to the imaging stage. Catheterized mice were changed to continuous administration of α-chloralose anaesthesia (50 mg/kg animal per hour) via an intravenous catheter, and they were allowed to stabilized for 25 minutes before the imaging session started.

All these procedures are graphically explained in Figure 35.

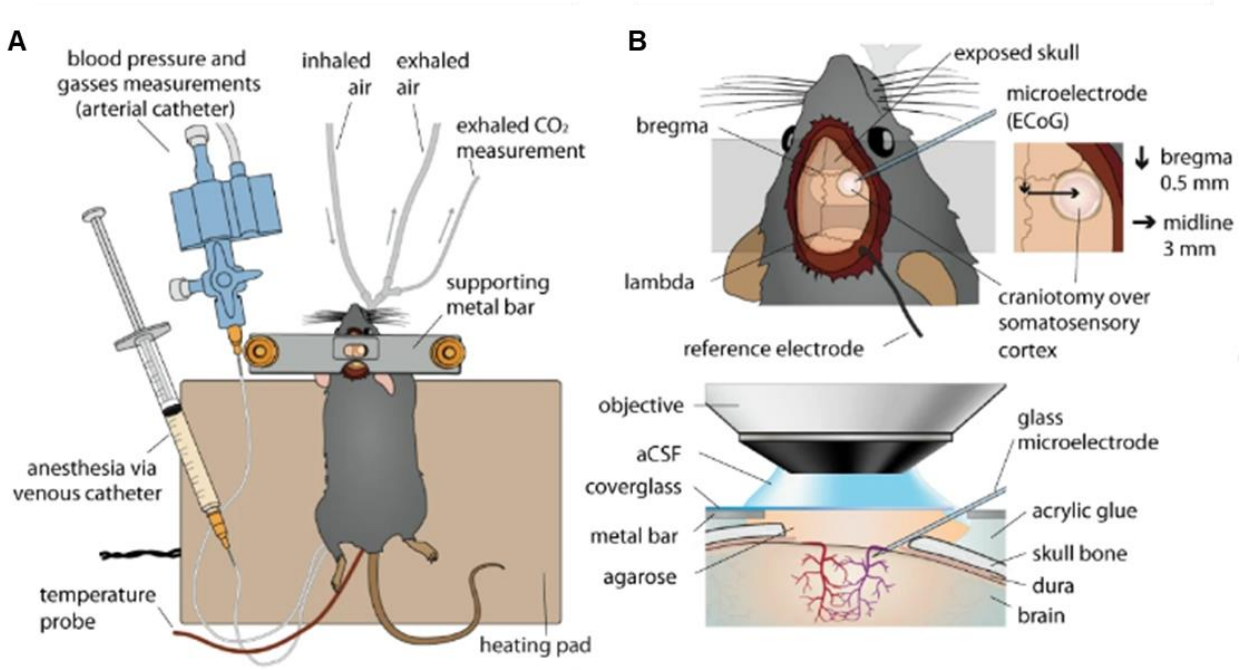

Figure 35. ← Previous page A) Schematic drawing of the mouse preparation for the craniotomy. B) Mouse head with the location of craniotomy and the final disposition of the cranial window with respect to the two-photon imaging set-up. Image borrowed from *Kucharz et al. 2021* [99].

Fluorescent probes:

Intravascular injection. In some experiments in which animals were catheterized, either FITC-dextran (MW 2 MDa, 0.5%, Sigma-Aldrich) or TRITC-dextran (MW 65 kDa, 1%, Sigma-Aldrich) dissolved in sterile saline was administered as a single bolus injection (50 µL) via the femoral arterial catheter.

Retro-orbital injection. Experiments in which animals were not catheterized, either FITC-dextran (MW 2 MDa, 0.5%, Sigma-Aldrich) or TRITC-dextran (MW 65 kDa, 1%, Sigma-Aldrich) dissolved in sterile saline was administered as a single bolus injection (30 µL) via retro-orbital injection (Figure 36).

These fluorescent probes served to delineate vessel lumen and lack of extravascular dyes indicated preserved BBB structural integrity after craniotomy (Figure 36). In addition, delineating the vessels served as a tissue reference for brain ECS injection of other fluorescent molecules.

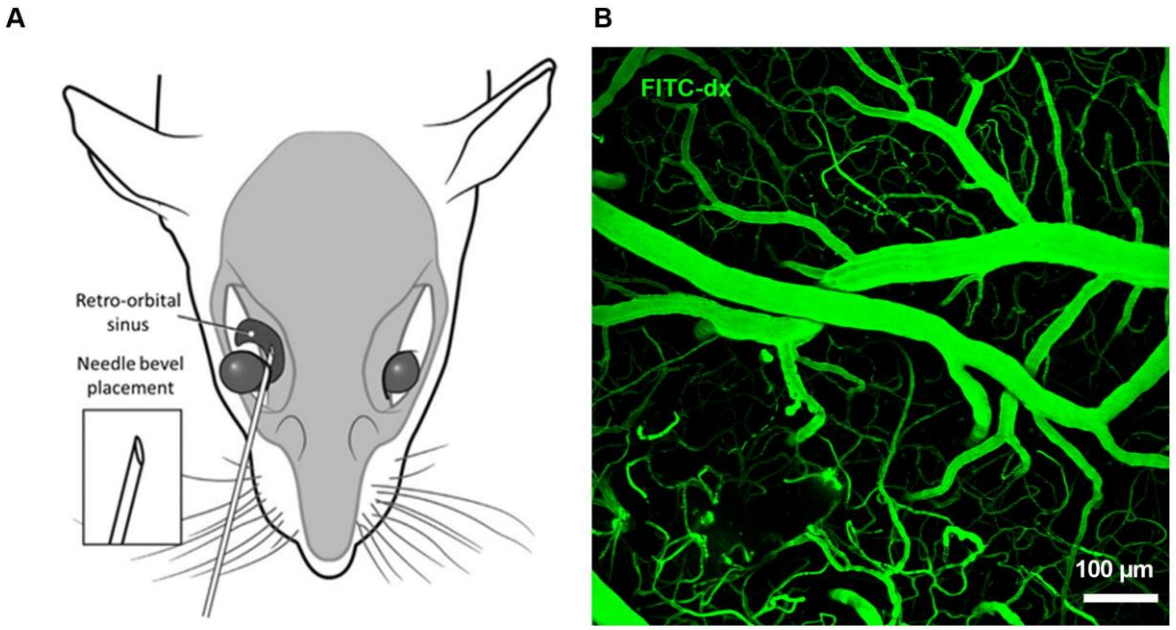

Figure 36. Retro-orbital injection of FITC-dx in mouse. A) Graphical representation of retro-orbital injection in mouse. B) Maximum projection of a z-stack showing the labeled vessels with retro-orbital administration of FITC-dx 2MDa. Scalebar 100 µm.

Retro-orbital injection Different sized molecules: Sodium Fluorescein (NaF, Sigma-Aldrich, 10 % solution in saline, 376 Da) and Alexa Fluor 488 (AF; Sigma-Aldrich; 1% solution in saline, 643 Da) and Alexa Fluor 594 (AF; Sigma-Aldrich; 1% solution in saline, 819 Da) were administered directly into the brain extracellular space through a glass micropipette filled with dye. The micropipette was introduced into the brain tissue as shown in Figure 35 B.

Imaging setup.

In-vivo 2P imaging was performed with an SP5 upright laser scanning microscope (Leica Microsystems) coupled to MaiTai Ti:Sapphire laser (Spectra-Physics). The images were collected using a 20× 1.0 NA water immersion objective. The fluorescence signal was split by FITC/TRITC filter and collected by two separate multi-alkali photomultipliers after 525–560 nm and 560–625 nm bandpass filter (Leica Microsystems). The fluorophores were excited at 870 nm with the 14 mWatt output power at the sample. The images were collected using LAS AF v. 4.4 (Leica Microsystems) in 16-bit color depth and exported to ImageJ for further analysis.

Image acquisition of fluorescent probe diffusion

In one condition, we loaded the glass micropipette with both Alexa 488 and Alexa 594, to compare two molecules with same size. In the other condition the micropipette was loaded with NaF and Alexa 594 to compare different sized molecules. Once the micropipette was introduced in the brain parenchyma the imaging protocol started. Images were 1024x1024 pixels and were acquired at 400 Hz. To image Alexa 488 and 594 at the same time we use a 900nm excitation wavelength with a red channel PMT (photomultiplier) gain of 870 and a green channel PMT gain of 800. To image Alexa 594 and NaF at the same time we used an 840 nm excitation wavelength and the gain of both PMTs was set to 850.

As soon as the pipette was introduced in the brain tissue and located we took time-lapse images of the dyes' free diffusion, a frame every 2 seconds over 40 minutes. After those 40 minutes, the steady state was reached and we analysed the bleaching properties of the dyes. To assess bleaching we took time-lapse images at different rates: fast (a frame every 1 second) and slow (a frame every 5 second) during 2 minutes. At last we imaged the intensity decay after removing the micropipette from the tissue again with time-lapse images every 2 seconds during 40 minutes.

Data processing and analysis

Images were further analysed in Image J. All images were stabilized using the *Image Stabilizer* (Translation) plugin from Image J. Intensity rise, steady state (for photobleaching) and decay of different fluorescent dyes were analysed over time by measuring the average pixel intensity over time at 7 different concentric areas at 150 µm and at 250 µm from the source. "*ROI manager"* and "*Time Series Analyzer"* plugs-in of ImageJ were used for this purpose. Fluorescence intensity for each area was normalized with respect to the maximum and minimum intensity values of the time-lapse, for the rise and decay scenarios. Steady-state fluorescence was normalized with respect to the first frame of the time-lapse.

To analyse photobleaching we just used the intensity measured at 150 µm from the source. After normalization, we fitted a line to each trace and measure the slope for the different dyes at the different imaging rates (fast, 1 frame per second; and slow, 1 frame per 5 seconds). All data were represented and analysed using GraphPad Prism.

In addition, we measured the exponential growth/decay constant (τ) to estimate how fast is the diffusion of the different dyes in the brain parenchyma. τ represents the time point at which the fluorophore concentration is 1/e times the initial/steady state concentration (where 1/e ≈ 0.367879441). To estimate τ, we use the ''*Exponential Recovery with Offset*'' from ImageJ and fitted an exponential equation (Equation 17) to each intensity profile at each of the different areas of interest.

Equation 17

$$y = a \cdot e^{-\frac{t}{\tau}} + c$$

As a result, we obtained an estimate for τ for each of the measuring areas both at 150 and 250 µm for the three fluorophores.

Preliminary Data

First, we compare the free diffusion in brain parenchyma of two Alexa Fluor dyes Alexa 488 (MW: 643 Da) and Alexa 594 (MW: 819 Da). We imaged the rise in intensity as soon as the glass micropipette containing the dyes was introduced in the tissue (not included in Figure 37). However, imaging the rise in intensity is not trivial as it requires to quickly change objectives to a higher magnification and rapidly locating again the micropipette. As a result, in many experiments the diffusion of the dye was already quite advanced once we started the time-lapse. During the steady state phase, we took time-lapse images at different rates to study the bleaching properties of Alexa 488 and 594. After fitting a straight line to the intensity profiles during the fast and the slow imaging rates, we observed that both Alexa 488 and 594 had very low slopes (between -0.02 and 0) in both imaging conditions, suggesting that the fluorophores were not bleaching with the used imaging parameters (Figure 37 B). Figure 37 A shows 2P *in-vivo* images of the decay of Alexa 488 (green) and Alexa 594 (red) as soon as the micropipette was removed from the brain tissue. The circles in the last frame show the areas were the average intensity was measured over time for further analysis. Figure 37 C shows the individual intensity profiles for each of the measured areas both at 150 and 250 µm from the source for both dyes. Alexa 488 and 594 showed the very similar decay patterns both at 150 and 250 µm (Figure 37 D, represented as mean + SD), which makes sense as they both have same chemical and physical properties. However, taking a closer look to the exponential decay constant (Figure 37 E), we observed that both at 150 and 250 µm Alexa 488 has a significantly smaller τ (at 150 µm: 3.23 ± 0.49; at 250 µm: 4.80 ± 0.14; mean ± SD) than Alexa 594 (at 150 µm: 4.95 ± 0.66; at 250 µm: 6.17 ± 0.33; mean ± SD) as reported by a two-ways ANOVA statistical test.

Altogether, these results suggest that the observed decayed is not due to photobleaching effect but to the actual free diffusion of Alexa Fluor. As expected, both dyes showed similar diffusion profiles but Alexa 488, which is a smaller molecule than Alexa 594, shows a faster decay (smaller τ).

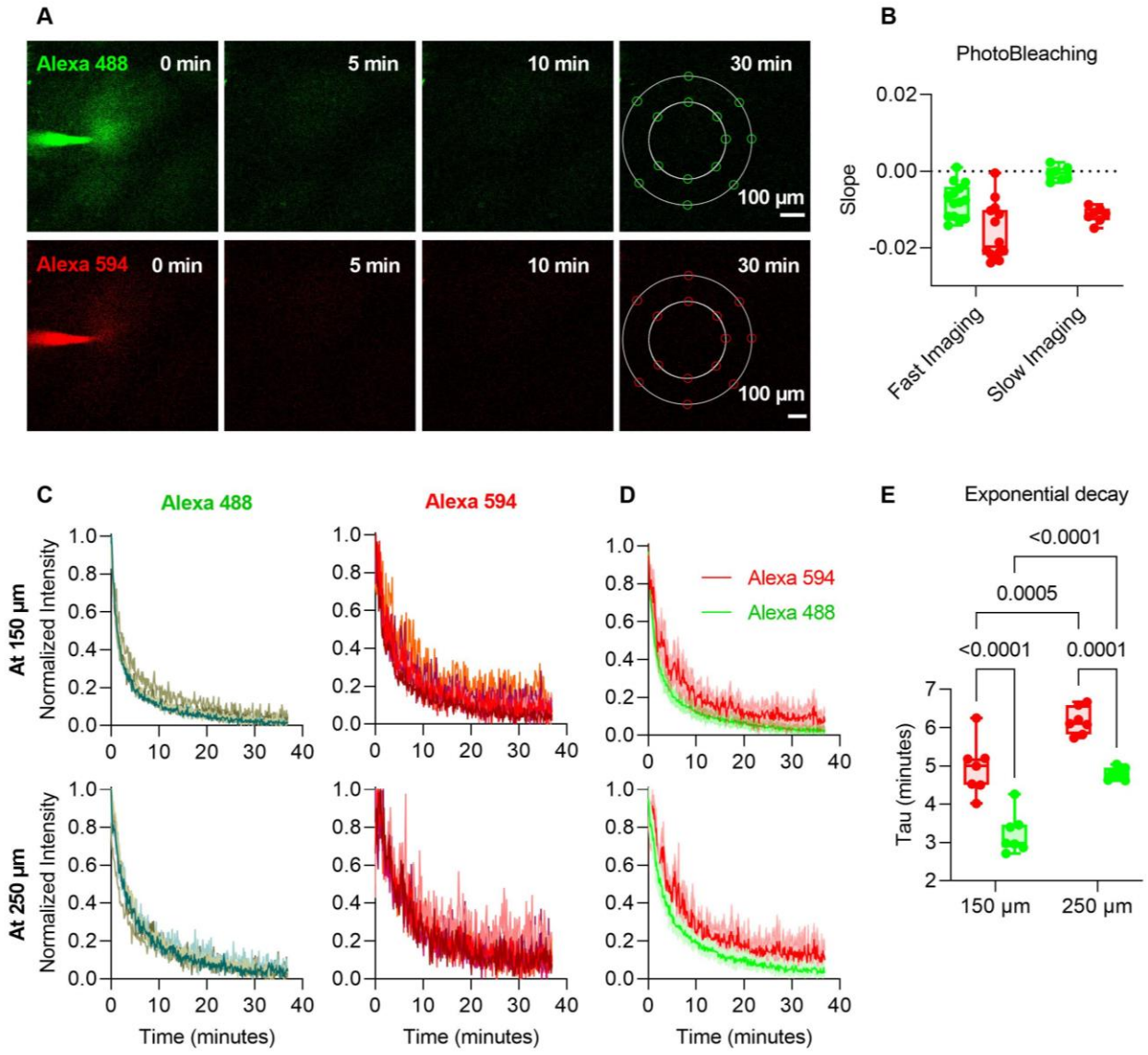

Figure 37. Two-photon *in-vivo* imaging of Alexa 488 and Alexa 594 diffusion in brain parenchyma. A) 2P images of Alexa 488 (green) and Alexa 594 (red) decay over time. Average intensity was measured at 7 areas at 150 and at 250 µm from the source, as represented in the last frame. Scalebar 100 µm. B) Slopes of the fitted lines for the fast and slow imaging rates represented as median and maximum and minimum boxplot. Individual data points represent the slope for each of the seven intensity profiles measured at 150 µm from the source. C) Normalized intensity profiles measured at each of the represented areas in A at 150 (top) and at 250 (bottom) µm for Alexa 488 (green) and Alexa 594 (red). D) Comparison between Alexa 488 and 594 intensity profiles. Data is represented as average profile (line) and SD (shadow) at 150 (top) and at 250 (bottom) µm. E) Exponential decay constant (τ) for Alexa 488 (green) and Alexa 594 (red) represented as mean with maximum and minimum values in a boxplot. Individual data

points correspond to the τ values estimated for each of the intensity profiles in C.P-values are represented for each comparison and result from a two-ways ANOVA statistical test.

Then we compared free diffusion in brain parenchyma of two different molecules: NaF (376 Da) and Alexa 594 (643 Da). We imaged the rise in intensity as soon as the glass micropipette containing the dyes was introduced in the tissue. This time, we were able to capture the free diffusion of NaF and Alexa 594 from the very beginning, as shown in Figure 38 A. The rise in intensity was measured over time for seven different areas at 150 and 250 µm (Figure 38 C and F respectively). Figure 38 D and G show the mean intensity profile + SD (shadowed) for Alexa 594 and NaF at 150 and 250 µm respectively. Quite surprisingly we observed that although Alexa 594 is bigger fluorescence intensity rises faster reaching steady-state before NaF. This is supported by the significantly bigger τ constant for NaF (at 150 µm: 11.05 ± 1.77; at 250 µm: 41.34 ± 19.22; mean ± SD) compared to Alexa 594 (at 150 µm: 4.39 ± 0.45; at 250 µm: 7.22 ± 0.82; mean ± SD) as reported by unpaired t-tests (Figure 38 E and H).

Once steady-state was reached, we assessed the photobleaching effect for each dye. We fitted a line to the intensity profiles of both dies during fast and slow imaging rates and once again the slopes of the lines were very small (between -0.02 and 0.02) suggesting that the fluorophores were not bleaching with the imaging parameters used (Figure 38 B).

Then, the micropipette was removed and we imaged the decay of the NaF and Alexa 594 fluorescence intensity overtime (Figure 39 A). The average intensity was measure over seven different areas at 150 and 250 µm from the source, as show in the last frame of Figure 39 A. Figure 39 C and D show the normalized intensity profiles corresponding to each of those areas at 150 and 250 µm respectively, for NaF and Alexa 594. Then, we compared NaF and Alexa 594 decay profiles (Figure 39 E), represented as mean normalized profile (line) + SD (shadowed). Again, Alexa 594 showed significant lower τ value (at 150 µm: 4.44 ± 0.47; at 250 µm: 6.83 ± 0.75; mean ± SD) than NaF (at 150 µm: 11.91 ± 1.65; at 250 µm: 30.46 ± 8.47; mean ± SD) as reported by a Two-ways ANOVA test (Figure 39 B). Thus, these results suggest that NaF diffusion in the *in-vivo* brain ECS is somehow hindered causing Alexa 594 to diffuse faster in the *in-vivo* brain parenchyma even though is actually bigger.

Unexpectedly, our results show that Alexa 594 diffuses faster than NaF, which is actually a smaller molecule with a reported higher diffusion coefficient in the extravascular compartment of the BBB [101]. We have not found any explanations to the observed hindered diffusion of NaF, but we expect that future work resulting from this collaboration will help us understand these preliminary data.

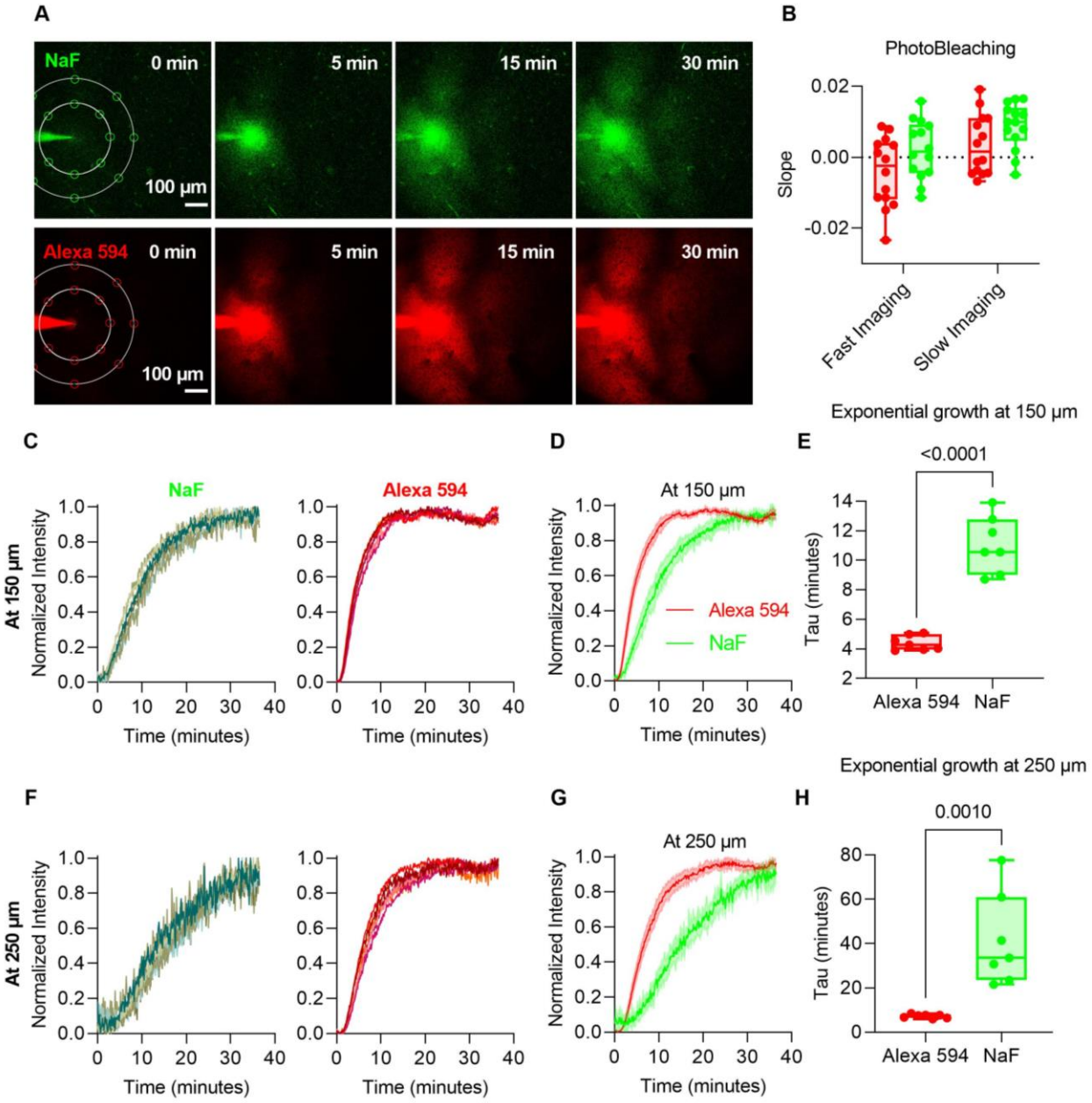

Figure 38. Two-photon *in-vivo* imaging of NaF and Alexa 594 diffusion in brain parenchyma. A) 2P images of NaF (green) and Alexa 594 (red) rise over time. Average intensity was measured at 7 areas at 150 and at 250 µm from the source, as represented in the last frame. Scalebar 100 µm. B) Slopes of the fitted lines for the fast and slow imaging rates represented as median with maximum and minimum values boxplot. Individual data points represent the slope for each of the seven intensity profiles measured at 150 µm from the source. C, F) Normalized intensity profiles measured at each of the represented areas in A for NaF (green) and Alexa 594 (red) at 150 and 250 µm respectively. D, G) Comparison between NaF and 594 rise profiles at 150 and 250 µm respectively. Data is represented as average profile (line) and SD (shadow). E, H) Exponential growth constant (τ) at 150 and 250 µm, respectively, for NaF (green) and Alexa 594 (red) represented as mean with maximum and minimum values in a boxplot. Individual data points correspond to the τ values estimated for each of the intensity profiles in C and F. P-value results from an unpaired t-test.

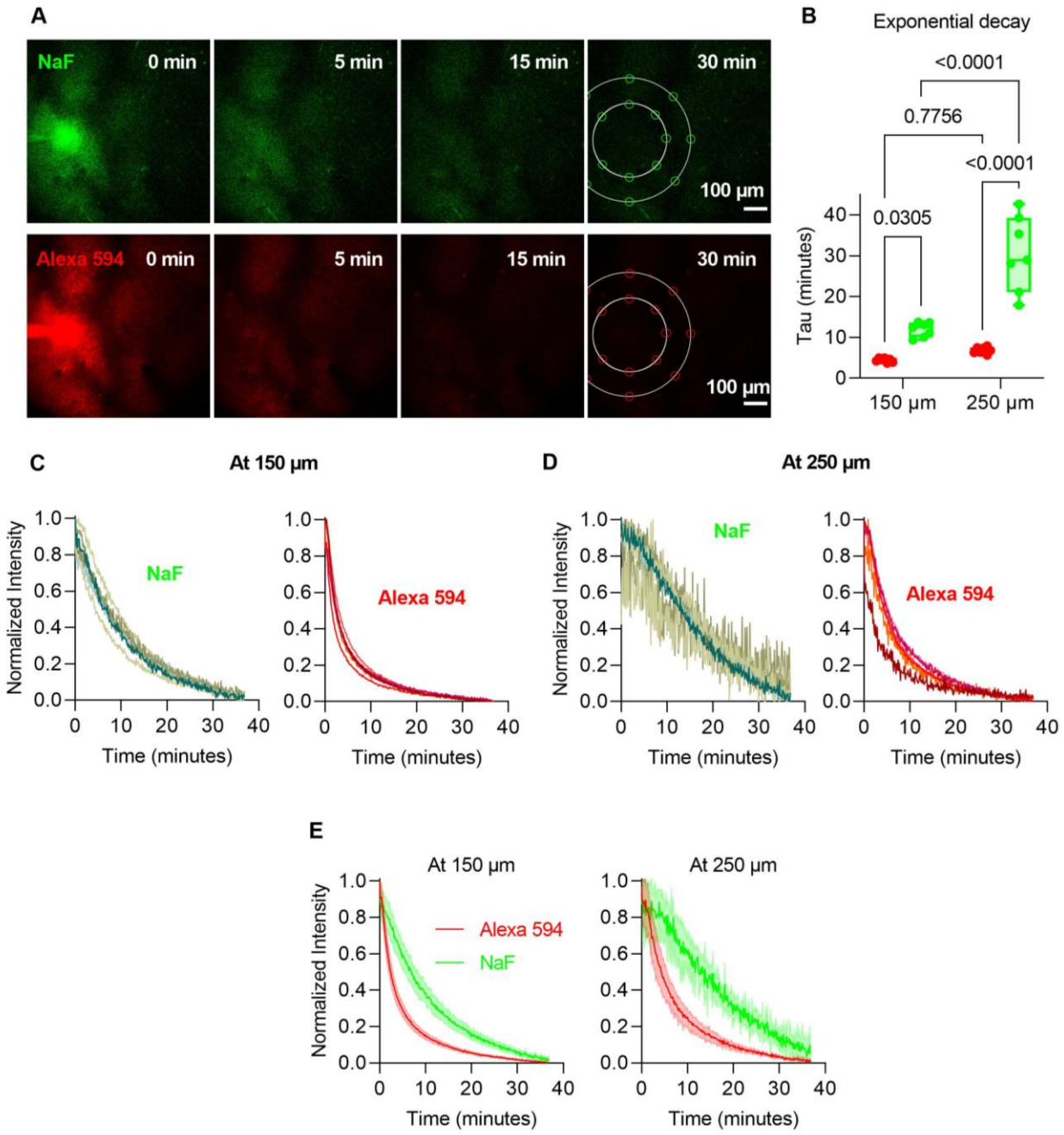

Figure 39. Two-photon *in-vivo* imaging of NaF and Alexa 594 decay in brain parenchyma A) 2P images of NaF (green) and Alexa 594 (red) decay over time. Average intensity was measured at 7 areas at 150 and at 250 µm from the source, as represented in the last frame. Scalebar 100 µm. B) Exponential decay constant (τ) for NaF (green) and Alexa 594 (red) represented as mean with maximum and minimum values in a boxplot. Individual data points correspond to the τ values estimated for each of the intensity profiles in A. P-values result from a two-ways ANOVA statistical test. C, D) Normalized intensity profiles for NaF (green) and Alexa 594 (red) measured at each of the represented areas in A at 150 µm and 250 µm respectively. E) Comparison between NaF and 594 decay profiles. Data is represented as average profile (line) and SD (shadow) at 150 (left) and at 250 (right) µm.

BIBLIOGRAPHY

[1] C. Bonnans, J. Chou, and Z. Werb, "Remodelling the extracellular matrix in development and disease," *Nat Rev Mol Cell Biol*, vol. 15, no. 12, pp. 786–801, Dec. 2014, doi: 10.1038/nrm3904.

[2] F. N. Soria, C. Miguelez, O. Peñagarikano, and J. Tønnesen, "Current Techniques for Investigating the Brain Extracellular Space," *Frontiers in Neuroscience*, vol. 14, 2020, Accessed: Mar. 14, 2023. [Online]. Available: https://www.frontiersin.org/articles/10.3389/fnins.2020.570750

[3] D. A. Rusakov and D. M. Kullmann, "Extrasynaptic Glutamate Diffusion in the Hippocampus: Ultrastructural Constraints, Uptake, and Receptor Activation," *J. Neurosci.*, vol. 18, no. 9, pp. 3158–3170, May 1998, doi: 10.1523/JNEUROSCI.18-09-03158.1998.

[4] K. Fuxe, D. O. Borroto-Escuela, W. Romero-Fernandez, W.-B. Zhang, and L. F. Agnati, "Volume transmission and its different forms in the central nervous system," *Chin J Integr Med*, vol. 19, no. 5, pp. 323–329, May 2013, doi: 10.1007/s11655-013-1455-1.

[5] S. Hrabětová and C. Nicholson, "Contribution of dead-space microdomains to tortuosity of brain extracellular space," *Neurochemistry International*, vol. 45, no. 4, pp. 467–477, Sep. 2004, doi: 10.1016/j.neuint.2003.11.011.

[6] C. Nicholson and S. Hrabětová, "Brain Extracellular Space: The Final Frontier of Neuroscience," *Biophys J*, vol. 113, no. 10, pp. 2133–2142, Nov. 2017, doi: 10.1016/j.bpj.2017.06.052.

[7] S. P. Kuo, P.-P. Chiang, A. R. Nippert, and E. A. Newman, "Spatial Organization and Dynamics of the Extracellular Space in the Mouse Retina," *J. Neurosci.*, vol. 40, no. 41, pp. 7785–7794, Oct. 2020, doi: 10.1523/JNEUROSCI.1717-20.2020.

[8] X. Huang, K. Li, Y. Liu, C. Yang, and H. Han, "Quantitative Measurement of Brain Extracellular Space with Three-Dimensional Electron Microscopy Imaging," *Sens Imaging*, vol. 24, no. 1, p. 2, Jan. 2023, doi: 10.1007/s11220-022-00408-z.

[9] E. Syková and C. Nicholson, "Diffusion in Brain Extracellular Space," *Physiological Reviews*, vol. 88, no. 4, pp. 1277–1340, Oct. 2008, doi: 10.1152/physrev.00027.2007.

[10] M. Vincent, M. Gaudin, C. Lucas-Torres, A. Wong, C. Escartin, and J. Valette, "Characterizing extracellular diffusion properties using diffusion-weighted MRS of sucrose injected in mouse brain," *NMR in Biomedicine*, vol. 34, no. 4, p. e4478, 2021, doi: 10.1002/nbm.4478.

[11] M. A. Perez-Pinzon, L. Tao, and C. Nicholson, "Extracellular potassium, volume fraction, and tortuosity in rat hippocampal CA1, CA3, and cortical slices during ischemia," *Journal of Neurophysiology*, vol. 74, no. 2, pp. 565–573, Aug. 1995, doi: 10.1152/jn.1995.74.2.565.

[12] I. Vorisek and E. Sykova, "Measuring diffusion parameters in the brain: comparing the real-time iontophoretic method and diffusion-weighted magnetic resonance," *Acta Physiologica*, vol. 195, no. 1, pp. 101–110, 2009, doi: 10.1111/j.1748-1716.2008.01924.x.

[13] J. Hrabe and S. Hrabetova, "Time-Resolved Integrative Optical Imaging of Diffusion during Spreading Depression," *Biophysical Journal*, vol. 117, no. 10, pp. 1783–1794, Nov. 2019, doi: 10.1016/j.bpj.2019.08.031.

[14] A. M. Arranz *et al.*, "Hyaluronan Deficiency Due to Has3 Knock-Out Causes Altered Neuronal Activity and Seizures via Reduction in Brain Extracellular Space," *Journal of Neuroscience*, vol. 34, no. 18, pp. 6164–6176, Apr. 2014, doi: 10.1523/JNEUROSCI.3458-13.2014.

[15] D. J. Wolak, M. E. Pizzo, and R. G. Thorne, “Probing the extracellular diffusion of antibodies in brain using in vivo integrative optical imaging and ex vivo fluorescence imaging,” *Journal of Controlled Release*, vol. 197, pp. 78–86, Jan. 2015, doi: 10.1016/j.jconrel.2014.10.034.

[16] F. Xiao, C. Nicholson, J. Hrabe, and S. Hrabětová, “Diffusion of Flexible Random-Coil Dextran Polymers Measured in Anisotropic Brain Extracellular Space by Integrative Optical Imaging,” *Biophysical Journal*, vol. 95, no. 3, pp. 1382–1392, Aug. 2008, doi: 10.1529/biophysj.107.124743.

[17] L. P. Savtchenko and D. A. Rusakov, “Extracellular diffusivity determines contribution of high-versus low-affinity receptors to neural signaling,” *Neuroimage*, vol. 25, no. 1, pp. 101–111, Mar. 2005, doi: 10.1016/j.neuroimage.2004.11.020.

[18] K. Kitamura, B. Judkewitz, M. Kano, W. Denk, and M. Häusser, “Targeted patch-clamp recordings and single-cell electroporation of unlabeled neurons in vivo,” *Nat Methods*, vol. 5, no. 1, Art. no. 1, Jan. 2008, doi: 10.1038/nmeth1150.

[19] N. Ohno, N. Terada, S. Saitoh, and S. Ohno, “Extracellular space in mouse cerebellar cortex revealed by in vivo cryotechnique,” *J Comp Neurol*, vol. 505, no. 3, pp. 292–301, Nov. 2007, doi: 10.1002/cne.21498.

[20] N. Korogod, C. C. Petersen, and G. W. Knott, “Ultrastructural analysis of adult mouse neocortex comparing aldehyde perfusion with cryo fixation,” *eLife*, vol. 4, p. e05793, Aug. 2015, doi: 10.7554/eLife.05793.

[21] J. Tønnesen, V. V. G. K. Inavalli, and U. V. Nägerl, “Super-Resolution Imaging of the Extracellular Space in Living Brain Tissue,” *Cell*, vol. 172, no. 5, pp. 1108-1121.e15, Feb. 2018, doi: 10.1016/j.cell.2018.02.007.

[22] G. Vicidomini, P. Bianchini, and A. Diaspro, “STED super-resolved microscopy,” *Nat Methods*, vol. 15, no. 3, Art. no. 3, Mar. 2018, doi: 10.1038/nmeth.4593.

[23] A. G. Godin *et al.*, “Single-nanotube tracking reveals the nanoscale organization of the extracellular space in the live brain,” *Nature Nanotech*, vol. 12, no. 3, Art. no. 3, Mar. 2017, doi: 10.1038/nnano.2016.248.

[24] F. N. Soria *et al.*, “Synucleinopathy alters nanoscale organization and diffusion in the brain extracellular space through hyaluronan remodeling,” *Nat Commun*, vol. 11, no. 1, Art. no. 1, Jul. 2020, doi: 10.1038/s41467-020-17328-9.

[25] M. Magzoub, H. Zhang, J. A. Dix, and A. S. Verkman, “Extracellular space volume measured by two-color pulsed dye infusion with microfiberoptic fluorescence photodetection,” *Biophysical Journal*, vol. 96, no. 6, pp. 2382–2390, 2009, doi: 10.1016/j.bpj.2008.12.3916.

[26] S. Mériaux, A. Conti, and B. Larrat, “Assessing Diffusion in the Extra-Cellular Space of Brain Tissue by Dynamic MRI Mapping of Contrast Agent Concentrations,” *Frontiers in Physics*, vol. 6, 2018, Accessed: Apr. 19, 2022. [Online]. Available: https://www.frontiersin.org/article/10.3389/fphy.2018.00038

[27] K. Zheng, T. P. Jensen, L. P. Savtchenko, J. A. Levitt, K. Suhling, and D. A. Rusakov, “Nanoscale diffusion in the synaptic cleft and beyond measured with time-resolved fluorescence anisotropy imaging,” *Sci Rep*, vol. 7, no. 1, Art. no. 1, Feb. 2017, doi: 10.1038/srep42022.

[28] S. F. Traynelis and R. Dingledine, “Potassium-induced spontaneous electrographic seizures in the rat hippocampal slice,” *J Neurophysiol*, vol. 59, no. 1, pp. 259–276, Jan. 1988, doi: 10.1152/jn.1988.59.1.259.

[29] F. E. Dudek, A. Obenaus, and J. G. Tasker, “Osmolality-induced changes in extracellular volume alter epileptiform bursts independent of chemical synapses in the rat: Importance of non-synaptic mechanisms in hippocampal epileptogenesis,” *Neuroscience Letters*, vol. 120, no. 2, pp. 267–270, Dec. 1990, doi: 10.1016/0304-3940(90)90056-F.

[30] W. Kilb, P. W. Dierkes, E. Syková, L. Vargová, and H. J. Luhmann, “Hypoosmolar conditions reduce extracellular volume fraction and enhance epileptiform activity in the CA3 region of the immature rat hippocampus,” *J. Neurosci. Res.*, vol. 84, no. 1, pp. 119–129, Jul. 2006, doi: 10.1002/jnr.20871.

[31] E. Shahar, M. Derchansky, and P. L. Carlen, “The role of altered tissue osmolality on the characteristics and propagation of seizure activity in the intact isolated mouse hippocampus,” *Clinical Neurophysiology*, vol. 120, no. 4, pp. 673–678, Apr. 2009, doi: 10.1016/j.clinph.2009.01.014.

[32] M. Arizono, V. V. G. K. Inavalli, and U. V. Nägerl, “Super-resolution shadow imaging reveals local remodeling of astrocytic microstructures and brain extracellular space after osmotic challenge,” *bioRxiv*, p. 2021.01.05.425369, Jan. 2021, doi: 10.1101/2021.01.05.425369.

[33] L. Xie *et al.*, “Sleep Drives Metabolite Clearance from the Adult Brain,” *Science*, vol. 342, no. 6156, p. 10.1126/science.1241224, Oct. 2013, doi: 10.1126/science.1241224.

[34] N. A. Jessen, A. S. F. Munk, I. Lundgaard, and M. Nedergaard, “The Glymphatic System: A Beginner’s Guide,” *Neurochem Res*, vol. 40, no. 12, pp. 2583–2599, Dec. 2015, doi: 10.1007/s11064-015-1581-6.

[35] M. I. Banks and R. A. Pearce, “Kinetic Differences between Synaptic and Extrasynaptic GABAA Receptors in CA1 Pyramidal Cells,” *J. Neurosci.*, vol. 20, no. 3, pp. 937–948, Feb. 2000, doi: 10.1523/JNEUROSCI.20-03-00937.2000.

[36] W. Wei, N. Zhang, Z. Peng, C. R. Houser, and I. Mody, “Perisynaptic Localization of δ Subunit-Containing GABAA Receptors and Their Activation by GABA Spillover in the Mouse Dentate Gyrus,” *J. Neurosci.*, vol. 23, no. 33, pp. 10650–10661, Nov. 2003, doi: 10.1523/JNEUROSCI.23-33-10650.2003.

[37] M. Farrant and Z. Nusser, “Variations on an inhibitory theme: phasic and tonic activation of GABAA receptors,” *Nat Rev Neurosci*, vol. 6, no. 3, Art. no. 3, Mar. 2005, doi: 10.1038/nrn1625.

[38] I. Mody, “Distinguishing Between GABAA Receptors Responsible for Tonic and Phasic Conductances,” *Neurochem Res*, vol. 26, no. 8, pp. 907–913, Sep. 2001, doi: 10.1023/A:1012376215967.

[39] A. Semyanov, M. C. Walker, D. M. Kullmann, and R. A. Silver, “Tonically active GABAA receptors: modulating gain and maintaining the tone,” *Trends in Neurosciences*, vol. 27, no. 5, pp. 262–269, May 2004, doi: 10.1016/j.tins.2004.03.005.

[40] M. C. Spiciarich, J. R. von Gaudecker, L. Jurasek, D. F. Clarke, J. Burneo, and J. Vidaurre, “Global Health and Epilepsy: Update and Future Directions,” *Curr Neurol Neurosci Rep*, vol. 19, no. 6, p. 30, May 2019, doi: 10.1007/s11910-019-0947-6.

[41] C. Steinhäuser, M. Grunnet, and G. Carmignoto, “Crucial role of astrocytes in temporal lobe epilepsy,” *Neuroscience*, vol. 323, pp. 157–169, May 2016, doi: 10.1016/j.neuroscience.2014.12.047.

[42] V. Lee and J. Maguire, “The impact of tonic GABAA receptor-mediated inhibition on neuronal excitability varies across brain region and cell type,” *Front Neural Circuits*, vol. 8, p. 3, 2014, doi: 10.3389/fncir.2014.00003.

[43] I. Pavlov and M. C. Walker, “Tonic GABA(A) receptor-mediated signalling in temporal lobe epilepsy,” *Neuropharmacology*, vol. 69, pp. 55–61, Jun. 2013, doi: 10.1016/j.neuropharm.2012.04.003.

[44] I. Pavlov *et al.*, "Progressive loss of phasic, but not tonic, GABAA receptor-mediated inhibition in dentate granule cells in a model of post-traumatic epilepsy in rats," *Neuroscience*, vol. 194, pp. 208–219, Oct. 2011, doi: 10.1016/j.neuroscience.2011.07.074.

[45] H. P. Goodkin, S. Joshi, Z. Mtchedlishvili, J. Brar, and J. Kapur, "Subunit-specific trafficking of GABA(A) receptors during status epilepticus," *J Neurosci*, vol. 28, no. 10, pp. 2527–2538, Mar. 2008, doi: 10.1523/JNEUROSCI.3426-07.2008.

[46] K. Rajasekaran, S. Joshi, C. Sun, Z. Mtchedlishvilli, and J. Kapur, "Receptors with low affinity for neurosteroids and GABA contribute to tonic inhibition of granule cells in epileptic animals," *Neurobiol Dis*, vol. 40, no. 2, pp. 490–501, Nov. 2010, doi: 10.1016/j.nbd.2010.07.016.

[47] N. Zhang, W. Wei, I. Mody, and C. R. Houser, "Altered Localization of GABAA Receptor Subunits on Dentate Granule Cell Dendrites Influences Tonic and Phasic Inhibition in a Mouse Model of Epilepsy," *J Neurosci*, vol. 27, no. 28, pp. 7520–7531, Jul. 2007, doi: 10.1523/JNEUROSCI.1555-07.2007.

[48] A. Scimemi, A. Semyanov, G. Sperk, D. M. Kullmann, and M. C. Walker, "Multiple and plastic receptors mediate tonic GABAA receptor currents in the hippocampus," *J Neurosci*, vol. 25, no. 43, pp. 10016–10024, Oct. 2005, doi: 10.1523/JNEUROSCI.2520-05.2005.

[49] D. E. Naylor, H. Liu, and C. G. Wasterlain, "Trafficking of GABA(A) receptors, loss of inhibition, and a mechanism for pharmacoresistance in status epilepticus," *J Neurosci*, vol. 25, no. 34, pp. 7724–7733, Aug. 2005, doi: 10.1523/JNEUROSCI.4944-04.2005.

[50] R.-Z. Zhan and J. V. Nadler, "Enhanced tonic GABA current in normotopic and hilar ectopic dentate granule cells after pilocarpine-induced status epilepticus," *J Neurophysiol*, vol. 102, no. 2, pp. 670–681, Aug. 2009, doi: 10.1152/jn.00147.2009.

[51] Z. Peng, C. S. Huang, B. M. Stell, I. Mody, and C. R. Houser, "Altered expression of the delta subunit of the GABAA receptor in a mouse model of temporal lobe epilepsy," *J Neurosci*, vol. 24, no. 39, pp. 8629–8639, Sep. 2004, doi: 10.1523/JNEUROSCI.2877-04.2004.

[52] K. Tsunashima, C. Schwarzer, E. Kirchmair, W. Sieghart, and G. Sperk, "GABA(A) receptor subunits in the rat hippocampus III: altered messenger RNA expression in kainic acid-induced epilepsy," *Neuroscience*, vol. 80, no. 4, pp. 1019–1032, Oct. 1997, doi: 10.1016/s0306-4522(97)00144-9.

[53] C. R. Houser and M. Esclapez, "Downregulation of the alpha5 subunit of the GABA(A) receptor in the pilocarpine model of temporal lobe epilepsy," *Hippocampus*, vol. 13, no. 5, pp. 633–645, 2003, doi: 10.1002/hipo.10108.

[54] J. Glykys, E. O. Mann, and I. Mody, "Which GABA(A) receptor subunits are necessary for tonic inhibition in the hippocampus?," *J Neurosci*, vol. 28, no. 6, pp. 1421–1426, Feb. 2008, doi: 10.1523/JNEUROSCI.4751-07.2008.

[55] D. Piniella *et al.*, "Experimental and Bioinformatic Insights into the Effects of Epileptogenic Variants on the Function and Trafficking of the GABA Transporter GAT-1," *International Journal of Molecular Sciences*, vol. 24, no. 2, Art. no. 2, Jan. 2023, doi: 10.3390/ijms24020955.

[56] G. Fattorini, M. Melone, and F. Conti, "A Reappraisal of GAT-1 Localization in Neocortex," *Frontiers in Cellular Neuroscience*, vol. 14, 2020, Accessed: Mar. 13, 2023. [Online]. Available: https://www.frontiersin.org/articles/10.3389/fncel.2020.00009

[57] O. EMG. Schijns *et al.*, "GAT-1 (rs2697153) and GAT-3 (rs2272400) polymorphisms are associated with febrile seizures and temporal lobe epilepsy," *Epileptic Disorders*, vol. 22, no. 2, pp. 176–182, 2020, doi: 10.1684/epd.2020.1154.

[58] E. Benarroch, "What Is the Role of GABA Transporters in Seizures?," *Neurology*, vol. 97, no. 12, pp. 580–584, Sep. 2021, doi: 10.1212/WNL.0000000000012574.

[59] K. Lauderdale, T. Murphy, T. Tung, D. Davila, D. K. Binder, and T. A. Fiacco, "Osmotic Edema Rapidly Increases Neuronal Excitability Through Activation of NMDA Receptor-Dependent Slow Inward Currents in Juvenile and Adult Hippocampus," *ASN Neuro*, vol. 7, no. 5, p. 175909141560511, Oct. 2015, doi: 10.1177/1759091415605115.

[60] J. Glykys, E. Duquette, N. Rahmati, K. Duquette, and K. J. Staley, "Mannitol decreases neocortical epileptiform activity during early brain development via cotransport of chloride and water," *Neurobiology of Disease*, vol. 125, pp. 163–175, May 2019, doi: 10.1016/j.nbd.2019.01.024.

[61] J. Bischofberger, D. Engel, L. Li, J. R. Geiger, and P. Jonas, "Patch-clamp recording from mossy fiber terminals in hippocampal slices," *Nat Protoc*, vol. 1, no. 4, Art. no. 4, Nov. 2006, doi: 10.1038/nprot.2006.312.

[62] X.-M. Zhu and W.-Y. Ong, "Changes in GABA transporters in the rat hippocampus after kainate-induced neuronal injury: Decrease in GAT-1 and GAT-3 but upregulation of betaine/GABA transporter BGT-1," *Journal of Neuroscience Research*, vol. 77, no. 3, pp. 402–409, 2004, doi: 10.1002/jnr.20171.

[63] J. I. Arellano, A. Muñoz, I. Ballesteros-Yáñez, R. G. Sola, and J. DeFelipe, "Histopathology and reorganization of chandelier cells in the human epileptic sclerotic hippocampus," *Brain*, vol. 127, no. Pt 1, pp. 45–64, Jan. 2004, doi: 10.1093/brain/awh004.

[64] T.-S. Lee *et al.*, "GAT1 and GAT3 expression are differently localized in the human epileptogenic hippocampus," *Acta Neuropathol*, vol. 111, no. 4, pp. 351–363, Apr. 2006, doi: 10.1007/s00401-005-0017-9.

[65] G. W. Mathern *et al.*, "Hippocampal GABA and glutamate transporter immunoreactivity in patients with temporal lobe epilepsy," *Neurology*, vol. 52, no. 3, pp. 453–472, Feb. 1999, doi: 10.1212/wnl.52.3.453.

[66] L. Héja *et al.*, "Glutamate uptake triggers transporter-mediated GABA release from astrocytes," *PLoS One*, vol. 4, no. 9, p. e7153, Sep. 2009, doi: 10.1371/journal.pone.0007153.

[67] L. Savtchenko, M. Megalogeni, D. A. Rusakov, M. C. Walker, and I. Pavlov, "Synaptic GABA release prevents GABA transporter type-1 reversal during excessive network activity," *Nat Commun*, vol. 6, no. 1, p. 6597, May 2015, doi: 10.1038/ncomms7597.

[68] A. Raghunandan *et al.*, "Bulk flow of cerebrospinal fluid observed in periarterial spaces is not an artifact of injection," *eLife*, vol. 10, p. e65958, Mar. 2021, doi: 10.7554/eLife.65958.

[69] T. R. Murphy, D. K. Binder, and T. A. Fiacco, "Turning down the volume: Astrocyte volume change in the generation and termination of epileptic seizures," *Neurobiol Dis*, vol. 104, pp. 24–32, Aug. 2017, doi: 10.1016/j.nbd.2017.04.016.

[70] R. Colbourn, A. Naik, and S. Hrabetova, "ECS Dynamism and Its Influence on Neuronal Excitability and Seizures," *Neurochem Res*, vol. 44, no. 5, pp. 1020–1036, May 2019, doi: 10.1007/s11064-019-02773-w.

[71] R. G. Thorne and C. Nicholson, "In vivo diffusion analysis with quantum dots and dextrans predicts the width of brain extracellular space," *Proceedings of the National Academy of Sciences*, vol. 103, no. 14, pp. 5567–5572, Apr. 2006, doi: 10.1073/pnas.0509425103.

[72] A. Saghyan, D. P. Lewis, J. Hrabe, and S. Hrabetova, “Extracellular diffusion in laminar brain structures exemplified by hippocampus,” *Journal of Neuroscience Methods*, vol. 205, no. 1, pp. 110–118, Mar. 2012, doi: 10.1016/j.jneumeth.2011.12.008.

[73] P. Sucha, M. Chmelova, M. Kamenicka, M. Bochin, T. Oohashi, and L. Vargova, “The Effect of Hapln4 Link Protein Deficiency on Extracellular Space Diffusion Parameters and Perineuronal Nets in the Auditory System During Aging,” *Neurochem Res*, vol. 45, no. 1, pp. 68–82, Jan. 2020, doi: 10.1007/s11064-019-02894-2.

[74] D. Thevalingam, A. A. Naik, J. Hrabe, D. P. McCloskey, and S. Hrabětová, “Brain extracellular space of the naked mole-rat expands and maintains normal diffusion under ischemic conditions,” *Brain Res*, vol. 1771, p. 147646, Nov. 2021, doi: 10.1016/j.brainres.2021.147646.

[75] C. Paviolo *et al.*, “Near-Infrared Carbon Nanotube Tracking Reveals the Nanoscale Extracellular Space around Synapses,” *Nano Lett.*, vol. 22, no. 17, pp. 6849–6856, Sep. 2022, doi: 10.1021/acs.nanolett.1c04259.

[76] W. R. Holmes, “Modeling the effect of glutamate diffusion and uptake on NMDA and non-NMDA receptor saturation.,” *Biophys J*, vol. 69, no. 5, pp. 1734–1747, Nov. 1995.

[77] H. G. Lipinski, “Monte Carlo simulation of extracellular diffusion in brain tissues,” *Phys Med Biol*, vol. 35, no. 3, pp. 441–447, Mar. 1990, doi: 10.1088/0031-9155/35/3/012.

[78] K. C. Chen and C. Nicholson, “Changes in brain cell shape create residual extracellular space volume and explain tortuosity behavior during osmotic challenge,” *Proceedings of the National Academy of Sciences*, vol. 97, no. 15, pp. 8306–8311, Jul. 2000, doi: 10.1073/pnas.150338197.

[79] J. Hrabe, S. Hrabětová, and K. Segeth, “A Model of Effective Diffusion and Tortuosity in the Extracellular Space of the Brain,” *Biophys J*, vol. 87, no. 3, pp. 1606–1617, Sep. 2004, doi: 10.1529/biophysj.103.039495.

[80] L. Ray, J. J. Iliff, and J. J. Heys, “Analysis of convective and diffusive transport in the brain interstitium,” *Fluids Barriers CNS*, vol. 16, no. 1, p. 6, Dec. 2019, doi: 10.1186/s12987-019-0126-9.

[81] K. E. Holter *et al.*, “Interstitial solute transport in 3D reconstructed neuropil occurs by diffusion rather than bulk flow,” *Proc Natl Acad Sci USA*, vol. 114, no. 37, pp. 9894–9899, Sep. 2017, doi: 10.1073/pnas.1706942114.

[82] J. P. Kinney, J. Spacek, T. M. Bartol, C. L. Bajaj, K. M. Harris, and T. J. Sejnowski, “Extracellular sheets and tunnels modulate glutamate diffusion in hippocampal neuropil,” *J Comp Neurol*, vol. 521, no. 2, pp. 448–464, Feb. 2013, doi: 10.1002/cne.23181.

[83] L. Savtchenko and D. Rusakov, “Increased Extrasynaptic Glutamate Escape in Stochastically Shaped Probabilistic Synaptic Environment,” *Biomedicines*, vol. 10, p. 2406, Sep. 2022, doi: 10.3390/biomedicines10102406.

[84] L. P. Savtchenko, K. Zheng, and D. A. Rusakov, “Buffering by Transporters Can Spare Geometric Hindrance in Controlling Glutamate Escape,” *Frontiers in Cellular Neuroscience*, vol. 15, 2021, Accessed: Apr. 03, 2023. [Online]. Available: https://www.frontiersin.org/articles/10.3389/fncel.2021.707813

[85] C. Nicholson, “Diffusion and related transport mechanisms in brain tissue,” *Rep. Prog. Phys.*, vol. 64, no. 7, pp. 815–884, Jul. 2001, doi: 10.1088/0034-4885/64/7/202.

[86] C. Nicholson and J. M. Phillips, “Ion diffusion modified by tortuosity and volume fraction in the extracellular microenvironment of the rat cerebellum.,” *The Journal of Physiology*, vol. 321, no. 1, pp. 225–257, Dec. 1981, doi: 10.1113/jphysiol.1981.sp013981.

[87] S. Hrabětová and C. Nicholson, “Biophysical Properties of Brain Extracellular Space Explored with Ion-Selective Microelectrodes, Integrative Optical Imaging and Related Techniques,” in *Electrochemical Methods for Neuroscience*, A. C. Michael and L. M. Borland, Eds., in Frontiers in Neuroengineering. Boca Raton (FL): CRC Press/Taylor & Francis, 2007. Accessed: Apr. 06, 2021. [Online]. Available: http://www.ncbi.nlm.nih.gov/books/NBK2581/

[88] J. R. Winkler, “Numerical recipes in C: The art of scientific computing, second edition,” *Endeavour*, vol. 17, no. 4, p. 201, Jan. 1993, doi: 10.1016/0160-9327(93)90069-F.

[89] T. Budisantoso, H. Harada, N. Kamasawa, Y. Fukazawa, R. Shigemoto, and K. Matsui, “Evaluation of glutamate concentration transient in the synaptic cleft of the rat calyx of Held,” *J Physiol*, vol. 591, no. 1, pp. 219–239, Jan. 2013, doi: 10.1113/jphysiol.2012.241398.

[90] Y. Wang *et al.*, “Counting the Number of Glutamate Molecules in Single Synaptic Vesicles,” *J Am Chem Soc*, vol. 141, no. 44, pp. 17507–17511, Nov. 2019, doi: 10.1021/jacs.9b09414.

[91] E. A. Matthews *et al.*, “Optical analysis of glutamate spread in the neuropil,” *Cerebral Cortex*, vol. 32, no. 17, pp. 3669–3689, Sep. 2022, doi: 10.1093/cercor/bhab440.

[92] G. Segovia, A. G. Yagüe, J. M. García-Verdugo, and F. Mora, “Environmental enrichment promotes neurogenesis and changes the extracellular concentrations of glutamate and GABA in the hippocampus of aged rats,” *Brain Research Bulletin*, vol. 70, no. 1, pp. 8–14, Jun. 2006, doi: 10.1016/j.brainresbull.2005.11.005.

[93] E. R. Hascup *et al.*, “Diet-induced insulin resistance elevates hippocampal glutamate as well as VGLUT1 and GFAP expression in AβPP/PS1 mice,” *Journal of Neurochemistry*, vol. 148, no. 2, pp. 219–237, 2019, doi: 10.1111/jnc.14634.

[94] B. R. Miller *et al.*, “Up-regulation of GLT1 expression increases glutamate uptake and attenuates the Huntington’s disease phenotype in the R6/2 mouse,” *Neuroscience*, vol. 153, no. 1, pp. 329–337, Apr. 2008, doi: 10.1016/j.neuroscience.2008.02.004.

[95] K. K. Szumlinski *et al.*, “Homer Proteins Regulate Sensitivity to Cocaine,” *Neuron*, vol. 43, no. 3, pp. 401–413, Aug. 2004, doi: 10.1016/j.neuron.2004.07.019.

[96] J. M. Michalska *et al.*, “Uncovering brain tissue architecture across scales with super-resolution light microscopy.” bioRxiv, p. 2022.08.17.504272, Aug. 18, 2022. doi: 10.1101/2022.08.17.504272.

[97] R. Fonseca, U. V. Nägerl, R. G. M. Morris, and T. Bonhoeffer, “Competing for memory: hippocampal LTP under regimes of reduced protein synthesis,” *Neuron*, vol. 44, no. 6, pp. 1011–1020, Dec. 2004, doi: 10.1016/j.neuron.2004.10.033.

[98] L. Mora-Jimenez *et al.*, “Transfer of SCN1A to the brain of adolescent mouse model of Dravet syndrome improves epileptic, motor, and behavioral manifestations,” *Molecular Therapy - Nucleic Acids*, vol. 25, pp. 585–602, Sep. 2021, doi: 10.1016/j.omtn.2021.08.003.

[99] K. Kucharz *et al.*, “Post-capillary venules are the key locus for transcytosis-mediated brain delivery of therapeutic nanoparticles,” *Nat Commun*, vol. 12, no. 1, Art. no. 1, Jul. 2021, doi: 10.1038/s41467-021-24323-1.

[100] K. Kucharz, N. Kutuzov, O. Zhukov, M. Mathiesen Janiurek, and M. Lauritzen, “Shedding Light on the Blood-Brain Barrier Transport with Two-Photon Microscopy In Vivo,” *Pharm Res*, vol. 39, no. 7, pp. 1457–1468, Jul. 2022, doi: 10.1007/s11095-022-03266-2.

[101] N. Kutuzov, H. Flyvbjerg, and M. Lauritzen, “Contributions of the glycocalyx, endothelium, and extravascular compartment to the blood-brain barrier,” *Proc Natl Acad Sci U S A*, vol. 115, no. 40, pp. E9429–E9438, Oct. 2018, doi: 10.1073/pnas.1802155115.